UNIVERSITY OF CALIFORNIA

Santa Barbara

Uncovering the Role of Progranulin in Human iPSC-Derived Microglia and Cerebral Organoids

A dissertation submitted in partial satisfaction of the

requirements for the degree Doctor of Philosophy

in Molecular, Cellular and Developmental Biology

by

Carolina Maciel Camargo

Committee in charge:

Professor Kenneth S. Kosik, Chair

Professor Brooke Gardner

Professor Dzwokai Zach Ma

Professor Meghan Morrissey

March 2024

The dissertation of Carolina Maciel Camargo is approved.

_____

Professor Brooke Gardner

_____

Professor Meghan Morrissey

_____

Professor Dzwokai Zach Ma

_____

Professor Kenneth S. Kosik, Committee Chair

December 2023

Uncovering the Role of Progranulin in Human iPSC-Derived Microglia and Cerebral Organoids

Carolina Maciel Camargo

To my mother, Ivete, the embodiment of love and strength, now my guardian angel and forever my inspiring soul.

To my father, Edson, my rock and my example of dedication and integrity, for sacrificing so much so I could have the best possible future.

To my brother, Otávio, my role model and my confidant, for supporting and comforting me through the most challenging times.

I'm only here today because of you.

ACKNOWLEDGEMENTS

I had the privilege of working with exceptional individuals during my PhD journey. First and foremost, I must express my gratitude to my advisor, Dr. Kenneth Kosik, for giving me the opportunity of a lifetime to engage in cutting-edge research along with exceptional scientists. He not only believed in my potential but also pushed me to become the scientist I am today. However, for me what truly sets Dr. Kosik apart is that he is not only an exceptional scientist, but also a great human being. He consistently treated everyone with respect and kindness, and provided me support during the toughest personal challenges I faced throughout my graduate studies. I will forever be grateful for the invaluable support he provided during those difficult times.

I want to extend my gratitude to my committee members, Dr. Meghan Morrissey, Dr. Brooke Gardner, and Dr. Zach Ma. We did not meet often, but you gave me invaluable personal and scientific advice, and really pushed me so I could present the best version of my work.

Thank you to my fellow members of the Kosik Lab and the Center for Stem Cell Biology and Engineering, who taught me so much and made this journey much more enjoyable.

I would like to also thank my therapist, Dr. Conner, whose guidance was instrumental in helping me navigate through the toughest and final years of my graduate studies.

I am deeply grateful to my friends, who always supported me in happy and difficult times. A special mention goes to Ben Woody, who has stood by my side through so many years.

Lastly, I express my profound gratitude to my family – my mother, father, and brother. You mean the world to me, and I wouldn't have done any of this without your unconditional love and support.

CURRICULUM VITAE

Carolina Maciel Camargo

EDUCATION

University of California, Santa Barbara, CA 2023
Ph.D., Molecular, Cellular and Developmental Biology

Federal University of Paraná, Brazil 2015
M.S., Genetics

University Positivo/Federal University of Paraná, Brazil 2012
B.S., Biological Sciences

PROFESSIONAL EMPLOYMENT

University of California, Santa Barbara, CA 2015-2023
Graduate student researcher, Neuroscience Research Institute

University of California, Santa Barbara, CA 2015-2018
Teaching assistant, Department of Molecular, Cellular and Developmental Biology

Federal University of Paraná, Brazil 2013-2015
Graduate student researcher, Department of Genetics

Federal University of Paraná, Brazil 2011-2012
Undergraduate student researcher, Department of Genetics

PUBLICATIONS

Camargo, C. M., Almeida, M. C., Cupajita, J. M., Hwang, I., Kosik, K. S. (2024). Progranulin loss induces mitochondrial dysfunction and ferroptosis in human brain organoids. *Manuscript in preparation*.

Bai, Y., **Camargo, C. M.**, Glasauer, S. M. K., Gifford, R., Tian, X., Longhini, A. P., & Kosik, K. S. (2024). Single-cell mapping of lipid metabolites using an infrared probe in human-derived model systems. *Nature Communications*, *15*(1), 350.

Calonga-Solís, V., Olbrich, M., Ott, F., Adelman Cipolla, G., Malheiros, D., Künstner, A., Farias, T. D. J., **Camargo, C. M.**, Petzl-Erler, M. L., Busch, H., Fähnrich, A., & Augusto, D. G. (2023). The landscape of the immunoglobulin repertoire in endemic pemphigus foliaceus. *Frontiers in Immunology*, *14*(July), 1–12.

Salviano-Silva, A., Becker, M., Augusto, D. G., Busch, H., Adelman Cipolla, G., Farias, T. D. J., Bumiller-Bini, V., Calonga-Solís, V., Munz, M., Franke, A., Wittig, M., **Camargo, C. M.**, Goebeler, M., Hundt, J. E., Günther, C., Gläser, R., Hadaschik, E., Pföhler, C.,

Sárdy, M., … Malheiros, D. (2021). Genetic association and differential expression of HLA Complex Group lncRNAs in pemphigus. *Journal of Autoimmunity*, *123*, 102705.

Sohn, P. D., Huang, C. T. L., Yan, R., Fan, L., Tracy, T. E., **Camargo, C. M.**, Montgomery, K. M., Arhar, T., Mok, S. A., Freilich, R., Baik, J., He, M., Gong, S., Roberson, E. D., Karch, C. M., Gestwicki, J. E., Xu, K., Kosik, K. S., & Gan, L. (2019). Pathogenic Tau Impairs Axon Initial Segment Plasticity and Excitability Homeostasis. *Neuron*, *104*(3), 458-470.e5.

Oliveira, L. C., Kretzschmar, G. C., dos Santos, A. C. M., **Camargo, C. M.**, Nisihara, R. M., Farias, T. D. J., Franke, A., Wittig, M., Schmidt, E., Busch, H., Petzl-Erler, M. L., & Boldt, A. B. W. (2019). Complement Receptor 1 (CR1, CD35) Polymorphisms and Soluble CR1: A Proposed Anti-inflammatory Role to Quench the Fire of "Fogo Selvagem" Pemphigus Foliaceus. *Frontiers in Immunology*, *10*. https://doi.org/10.3389/fimmu.2019.02585

Camargo, C. M., Augusto, D. G., & Petzl-Erler, M. L. (2016). Differential gene expression levels might explain association of LAIR2 polymorphisms with pemphigus. *Human Genetics*, *135*(2), 233–244.

AWARDS

4-years full doctorate scholarship – Science Without Borders – CNPq 2015

First place in the graduate admission exam - Genetics Department, Federal University of Paraná 2013

ABSTRACT

Uncovering the Role of Progranulin in Human iPSC-Derived

Microglia and Cerebral Organoids

by

Carolina Maciel Camargo

Loss-of-function mutations in the granulin (*GRN*) gene cause frontotemporal dementia (FTD) in heterozygosity and neuronal ceroid lipofuscinosis (NCL), a lysosomal storage disease, in homozygosity. While it is well established that disease-causing *GRN* mutations decrease progranulin (PGRN) levels, leading to neurodegeneration, the cellular and molecular mechanisms underlying these conditions remain poorly understood. To investigate the impact of complete PGRN deficiency in human brain cells, we conducted two separate studies using two disease models: human induced pluripotent stem cell (iPSC)-derived forebrain organoids and microglia.

Forebrain organoids allowed us to probe the effects of PGRN deficiency on neuronal and glial cell populations. By employing single-cell RNA sequencing, we uncovered robust downregulation of the mitochondrial oxidative phosphorylation pathway in PGRN KO organoids. In alignment with these results, PGRN loss led to reduced mitochondrial respiration. Additionally, we demonstrated that PGRN KO organoids showed increased levels of reactive oxygen species and exhibited key hallmarks of ferroptosis, including increased lipid peroxidation and iron accumulation. Finally, we showed that PGRN loss leads to increased susceptibility to ferroptotic cell death.

In the second study, we explored the role of PGRN in human iPSC-derived microglia, a cell type absent in forebrain organoids. By integrating transcriptomic and lipidomic analyses, we revealed that PGRN plays a pivotal role in microglial lipid metabolism. PGRN KO microglia showed accumulation of triacylglycerides (TAGs) at baseline and after activation by lipopolysaccharide (LPS) exposure. Interestingly, the lipidomic profiles of resting and activated PGRN KO was distinct, with resting microglia showing a trend for enrichment of TAGs with saturated and monounsaturated long-chain fatty acids, and LPS-treated microglia showing accumulation of TAGs with very long chain polyunsaturated fatty acids. Moreover, we showed that PGRN loss leads to accumulation of lipid droplets. Transcriptomic analysis revealed that PGRN deficient microglia showed dysregulated expression of genes related to lipid metabolism, and our results suggest that PGRN loss drives lipid accumulation by inducing metabolic changes toward increased lipid synthesis and decreased lipid β-oxidation.

Our findings suggest a critical role of mitochondrial dysfunction and impaired responses to oxidative stress in driving neurodegeneration associated with PGRN deficiency, and indicate an important role of PGRN in regulating microglial function and lipid metabolism.

TABLE OF CONTENTS

Chapter 1

Introduction to progranulin in health and disease

1.1 Progranulin in frontotemporal dementia and neuronal ceroid lipofuscinosis

Frontotemporal dementia (FTD) is a group of neurodegenerative disorders that make up to 10% of all dementia cases, and after Alzheimer's it's the most common cause of early-onset neurodegenerative dementia in cases before 65 years of age. FTD is characterized by severe atrophy of the frontal and temporal lobes of the brain, and patients present behavioral and personality changes and/or language dysfunction (1,2). FTD is usually associated with tau or TAR DNA-binding protein 43 (TDP-43) (3).

Progranulin (PGRN) gained prominence within the neuroscience community in 2006, following the discovery that heterozygous mutations in the *GRN* gene (which encodes for PGRN) were the cause of FTD with TDP-43 inclusions (4–6). TDP-43 pathology is one of the hallmarks of the disease, and is characterized by ubiquitin-positive cytoplasmatic inclusions in affected cerebral regions that contain hyperphosphorylated TDP-43 protein (2,7). PGRN-related frontotemporal dementia (FTD-GRN) accounts for up to 11.7% of total FTD cases, and up to 25% of familial FTD cases (8). FTD-GRN is a fatal and rapidly progressing disease, with age of onset varying from 35 to 89 years, and almost fully penetrant by age 80 years (3,9). In addition to atrophy of the frontal and temporal lobes, there is also atrophy extending into the parietal lobe (10). Symptoms include behavioral changes with apathy and social withdrawal, hallucinations, impaired speech production, mutism, impaired comprehension, memory deficits, executive dysfunction and parkinsonism (3,10).

In 2012, a case report described two siblings with neuronal ceroid lipofuscinosis (NCL) resulting from homozygous mutations in *GRN* (11). NCL is a group of lysosomal storage disorders characterized by abnormal lysosomal accumulation of lipofuscin, an autofluorescent lipoprotein aggregate, in several tissues including the skin, retina and brain (12). The disease results in neuronal loss mainly in the cortex, cerebellum and thalamus (13). NCL caused by mutations in *GRN* (NCL type 11 or CLN11) is a rare disease that has been described in only 8 patients from 6 unrelated families to date (11,14–17). The patients display problems with balance and coordination (ataxia), vision loss, epilepsy and dementia, with the age of onset from 7 to 25 years. Neuronal loss occurs mainly in the cerebellum, but lipofuscin aggregates can also be found in the cortex (14).

Although the clinical manifestations of FTD-GRN and CLN11 are very distinct, they share several common pathological features such as lipofuscin accumulation, impaired lysosomal function, neuroinflammation and gliosis (18,19). Despite CLN11 patients not displaying TDP-43-positive inclusions, they can exhibit loss of normal TDP-43 localization in the nucleus, which may represent an initial stage in the TDP-43 pathological process that precedes the formation of cytoplasmic inclusions (14). It is important to note that some of the neuropathological features described above (neuroinflammation and gliosis) have not been yet confirmed in CLN11 patients, but deduced based on the similarities between CLN11 and other NCL diseases, and on homozygous *GRN* knockout mice.

As of today, over 70 mutations have been found in exons and introns of *GRN* in FTD patients (8). The majority of these pathogenic variants are nonsense, frameshift and splice site mutations causing a premature stop codon, that result in loss of function of the GRN gene via degradation of RNA through nonsense-mediated mRNA decay, although some missense mutations lead to changes in secretion and processing of PGRN (8). Homozygous mutations in *GRN* leads to complete absence of PGRN, while heterozygous mutations can result in reduction of ~50% or more in PGRN levels (4,8). Notably, some FTD-GRN patients show undetectable plasma levels of PGRN, while homozygous mutation carriers can display low levels of PGRN. Moreover, homozygous carriers can develop FTD instead of NCL (14). These findings suggest that not all variants have the same impact on PGRN expression, and that the pathophysiological mechanism in PGRN disorders might not depend only on PGRN levels. Variants that decrease progranulin levels are also associated with enhanced susceptibility to neurodegenerative diseases, including Parkinson's disease (PD) (20), amyotrophic lateral sclerosis (ALS) caused by repeat expansions in the *C9ORF72* (21), limbic-predominant age-

related transactivation response DNA-binding protein 43 encephalopathy (LATE) (22) and Alzheimer's disease (AD) (9,23), findings that underscore the role of PGRN in neurodegenerative diseases.

For the study of FTD-GRN and CLN11, a number of PGRN deficient mouse models have been generated (24–27). However, mice with partial loss of PGRN due to heterozygous mutations exhibit limited changes in behavior and neuropathology (28). Therefore, most studies have focused on studying homozygous *GRN* knockout mice. These mice exhibit lipofuscin accumulation, astrogliosis and microgliosis, which worsen with aging (28–30). Total PGRN loss in mice also leads to exacerbated microglial activation, neuronal loss and TDP-43 pathology (24,31,32). Moreover, these mice exhibit upregulation of lysosomal genes in microglia (31,33), linking PGRN, microglial activation and lysosomal dysfunction. Overall, homozygous PGRN knockout mice recapitulate major pathological hallmarks of FTD-GRN and CLN11.

1.2 Progranulin overview

Human progranulin, also known as granulin precursor, is encoded by the *GRN* (also known as *GEP, GP88, PEPI, CLN11* or *PCDGF*) gene, residing on chromosome 17q21.32 and composed of 13 exons. PGRN is a highly glycosylated 593 amino acid-long, 88 kDa glycoprotein (34,35) that can be secreted or located intracellularly. PGRN is highly conserved across species, which underscores its evolutionary significance. Progranulin-like proteins are present in unicellular eukaryotes, plants and metazoan animals, suggesting PGRN is one of earliest extracellular regulatory proteins that continue to play important roles in multicellular animals (36).

Structurally, PGRN consists of seven and a half tandemly repeated cysteine-rich granulin domains, namely paragranulin (p, a granulin half domain, with ~3 kDa), and granulins A-G (~6 kDa) (34,35,37). The granulins within PGRN are connected by short linear sequences known as linkers, that can be cleaved through proteolysis, resulting in the release of mature granulin proteins (35), or fragments composed of multiple granulins (38,39).

PGRN is expressed in myeloid, epithelial, endothelial cells and fibroblasts in periphery, and in neurons, microglia, endothelial cells and astrocytes in the central nervous system (CNS) (9,40). Intracellularly, PGRN is located in the endoplasmic reticulum (ER), Golgi apparatus, and secretory vesicles, consistent with its secretion, and lysosomes and endo-lysosomes (39,41–43). Full length PGRN is secreted into the extracellular matrix by exocytosis as a soluble protein (44) or associated with exosomes (45). Extracellularly, it may undergo proteolytic processing by elastases (46–48), matrix metalloproteinases MMP-9 (49) and MMP-14 (50), a disintegrin and metalloproteinase with thrombospondin type 1 motif 7 ADAMTS-7 (51) and proteinase 3 (PR3) (48). Once in the extracellular space, PGRN binds sortilin and it reaches the lysosome through endocytosis (43). Alternatively, intracellularly it can reach the lysosome by binding to sortilin (SORT), or prosaposin (PSAP) and via the trafficking receptors M6PR and LRP1, where it is redirected from the secretory pathway to the endolysosomal pathway (52). Intracellular processing of PGRN also occurs in the endolysosomal compartments by cysteine proteases cathepsin D and L (35,53,54). Additionally, a more recent study showed that cathepsins E, G, K, S and V can also cleave PGRN in *in vitro* cleavage assays (39).

PGRN is a growth factor involved in wound healing, immune response, inflammation and cell proliferation (55,56). In the periphery, PGRN is involved in promoting tissue repair

and wound healing. For example, studies have shown that PGRN accelerates the healing of skin wounds in mice by promoting the migration and proliferation of neutrophils, macrophages, fibroblasts and accumulation of blood vessels in the wound site (57). It also acts as a growth factor to stimulate cell proliferation of various cell types, including epithelial and endothelial cells, contributing to tissue growth and repair (58,59). Moreover, it is often overexpressed in cancers and as a tumor progression factor it's been linked to breast, ovary, endometrium, liver and kidney cancers, and non-epithelial cancers such as myelomas, gliomas and meningiomas (60). PGRN is also overexpressed during infections, such as pneumonia and sepsis (61,62), and PGRN deficient mice exhibit increased susceptibility to bacterial infections (24). Interestingly, full-length PGRN and granulins seem to have opposing functions in inflammation and cell growth. Full length PGRN plays anti-inflammatory roles by upregulating anti-inflammatory cytokines IL-10 and IL-13, and inhibiting TNFα signaling (47,48,56,63), while granulins have pro-inflammatory properties, by stimulating the secretion of IL-8, TNF-α and IL-1β (47,56,64). In terms of cell proliferation, full-length PGRN is mitogenic, while different granulins can induce or inhibit cell growth (47,65,66).

Besides its role in extracellular signaling as a secreted protein, PGRN regulates lysosomal function. The discovery that patients with homozygous *GRN* mutations developed NCL was the pivotal event that brought progranulin's role in the lysosome to the forefront. Since then, a large number of studies have revealed the key role of PGRN in the lysosome. As stated earlier, PGRN is trafficked and processed inside the cell in endolysosomal compartments. PGRN facilitates acidification of lysosomes (67) and modulates the activities of lysosomal enzymes such as glucocerebrosidase (GCase), an enzyme that metabolizes glycosphingolipids (68–70), and cathepsin D (67,71,72). PGRN deficiency leads to enlarged

lysosomes with altered morphology in mice and humans (19,33,73). Moreover, brains of patients with FTD-GRN have elevated lysosomal proteins, including saposin D, cathepsin D, and LAMP1 (18). *GRN*$^{-/-}$ mice also show increased levels of lysosomal lipofuscin particles and lysosomal proteins, such as cathepsin D and LAMP1 (30,32,74,75). The increased expression of lysosomal proteins due to PGRN loss could be in part via transcription factor EB (TFEB) activation (40,74). TFEB is master regulator of lysosome biogenesis, and the promoter region of *GRN* has TFEB binding sites. The mechanisms underlying how PGRN levels influence TFEB activity remain unclear (40). FTD-GRN patients and *GRN*$^{-/-}$ mice also show aberrant brain lipid composition, which has been suggested to be caused, at least partly, by lysosomal dysfunction (73).

1.3 Progranulin function in the brain

In the CNS, PGRN is highly expressed in the cerebral cortex, hippocampus and cerebellum (76,77), and mainly expressed in neurons, microglia, endothelial cells and astrocytes (9,40,78). Among these cell types, it is preferentially expressed in neurons and microglia, while microglia express the greatest amount of PGRN (25,33). PGRN expression increases as neurons mature (79), and through development it becomes more limited to some neuronal populations, such as cortical neurons, hippocampal pyramidal neurons, and Purkinje cells in the cerebellum (77). In microglia, PGRN expression varies depending on the state of activation, being upregulated in activated microglia (79). PGRN expression has been detected in astrocytes and oligodendrocytes in mouse and human brains, but in significantly lower amounts than that of microglia and neurons (46,78,80).

PGRN's role as a neurotrophic factor is well-established. It promotes neuronal survival and outgrowth of primary cortical and motor neurons when administered extracellularly (81,82), by regulation of activity of GSK-3β, that plays a key role in the Wnt pathway (81). In line with these findings, PGRN deficient neurons show decreased neurite outgrowth, branching and altered morphology (27,71,83). Moreover, PGRN protects neurons from cellular stress and stress-induced apoptosis. PGRN deficient neurons are more susceptible to stress caused by proteasome inhibitor MG132 (84), protein kinase inhibitor staurosporine (81), Aβ42 (85), PI3K and MEK inhibitors (86), NMDA and hydrogen peroxide (87,88). A recent study showed that lysosome-targeted PGRN had more protective effects against NMDA excitotoxicity than just PGRN, underscoring the role of PGRN in regulating lysosomal functional, and providing a link between PGRN lysosomal and neurotrophic functions (89). However, despite these observations, a key challenge has been identifying the receptor that binds to PGRN and allows for PGRN's neurotrophic functions (40). Sortilin is widely accepted as a PGRN receptor, but it is involved in the transport of PGRN and not in signaling pathways (43), and some neurotrophic functions of PGRN are independent of sortilin (83,90). Other receptors have been identified, such as TNFR and EphA2 (63,91), but more studies are necessary to provide the link between them and neurotrophic functions of PGRN.

PGRN is also involved in neuronal connectivity, by regulating synapse formation and function. PGRN has been shown to be co-transported with BDNF in primary hippocampal neurons, and the secretion of PGRN is dependent on neuronal activity (44). Additionally, PGRN knockout mice show altered synaptic connectivity and impaired synaptic plasticity (27). Moreover, it's been shown that reducing PGRN levels in primary hippocampal neurons leads to reduced neural connectivity due to decreased synaptic density and neuronal branching, while

increasing the number of synaptic vesicles per synapse (92). The same study showed that brains of patients with FTD-GRN also exhibit increased synaptic vesicle number (92).

In microglia, PGRN plays an important role in microglial activation and inflammatory response. Activated microglia are strongly immunoreactive for PGRN. Microglial PGRN is highly upregulated following traumatic brain injury (93), spinal cord injury (94) and axotomy (95). High PGRN levels are also found in lysosomal storage diseases (96), AD (97), Creutzfeldt–Jakob disease, and mouse models of ALS (98), where they are correlated to activated microglia (99). These results underscore the important role of PGRN in regulating the inflammatory response in the brain. Consistent with these findings, loss of PGRN leads to increased microglial activation and microgliosis. Depletion of PGRN leads to exaggerated microglial inflammation and microgliosis following traumatic brain injury (93), injury caused by MPTP (25), and with aging (24). Microglia and macrophages lacking PGRN, when exposed to bacterial lipopolysaccharide (LPS), display an exacerbated inflammatory reaction characterized by increased secretion of pro-inflammatory cytokines and decreased expression of the anti-inflammatory cytokine IL-10. Moreover, the conditioned media from these cells promotes neuronal cell death (24,25). PGRN also acts as a chemoattractant in the brain, as it's been shown that lentiviral expression of PGRN in mouse results in an increase of microglia around the injection site, and recombinant PGRN promotes microglial migration (100). In addition to upregulation of the inflammatory response, loss of PGRN leads to aberrant activation of the complement pathway. PGRN deficient microglia display increased expression of innate immune complement genes, such as *C1qa* and *C3* (31,33), and enhanced complement-activated synaptic pruning (33). It's been suggested that PGRN inhibits inflammation in microglia by binding to TNF receptor 2 (TNFR2), and thus blocking TNF-α

signaling (63,101), but other studies failed to replicate these findings (102,103). PGRN also serves as a soluble cofactor in Toll-like receptor 9 (TLR9) signaling, thus promoting secretion of pro-inflammatory cytokines and regulating the innate immune response (104,105).

PGRN also regulates the phagocytic capabilities of microglia, and in general loss of PGRN compromises phagocytosis. PGRN deficient microglia and macrophages show impaired phagocytosis and increased deposition of Aβ (106), impaired uptake of zymosan particles (107), and it's been shown that recombinant PGRN promotes increased microglial phagocytosis of Aβ (100). Interestingly, PGRN deficient macrophages exhibit increased phagocytosis of apoptotic cells (108).

The exacerbated activation of microglia due to PGRN loss is also accompanied by lysosomal dysfunction. It's been shown that PGRN deficiency promotes gene expression changes that characterize a shift of microglia from a homeostatic to a disease-specific state that causes endolysosomal dysfunction (31). Indeed, PGRN deficient microglia show increased lysosomal biogenesis, evident by increased size and number of lysosomes, and upregulation of lysosomal genes, particularly in activated microglia following neuroinflammation (18,33,74). underscoring the role of PGRN in microglial lysosomal function. Neurons of PGRN deficient mice and individuals with FTD-GRN also show increase in lysosomal storage materials and accumulation of abnormally large lysosomes of (19,31), indicating PGRN has roles in regulating lysosomes in other cell types other than microglia.

Similarly to the role of PGRN in microglia, PGRN regulates the inflammatory response of astrocytes. Astrocytes from PGRN-overexpressing mouse brains, when exposed to LPS, show lower expression of pro-inflammatory cytokines, and higher expression of IL-10 (109). In line with these findings, recombinant PGRN attenuates the pro-inflammatory profile of

activated astrocytes (110). PGRN deficient astrocytes also lead to decreased number of synapses and abnormal synapse morphology in human and mouse brains (111). Moreover, PGRN deficient mouse brains display microgliosis accompanied by astrogliosis with aging and following traumatic brain injury (24,110). It's been proposed that PGRN-deficient activated microglia can recruit and activate astrocytes (9,40). Indeed, it’s been shown that activated microglia can induce a subtype of reactive astrocytes (112). Alternatively, PGRN loss could directly activate astrocytes independently of microglia, but more studies are required to draw definitive conclusions (40).

Chapter 2

Progranulin loss induces mitochondrial dysfunction and ferroptosis in human cerebral organoids

2.1 Abstract

Loss-of-function mutations in the granulin (*GRN*) gene cause frontotemporal dementia in heterozygosity and neuronal ceroid lipofuscinosis, a lysosomal storage disease, in homozygosity. While it is well established that disease-causing *GRN* mutations decrease progranulin (PGRN) levels, leading to neurodegeneration, the cellular and molecular mechanisms underlying these conditions remain poorly understood. In this study, we utilized

human induced pluripotent stem cell (iPSC) derived forebrain organoids to investigate the impact of PGRN deficiency on neuronal and glial cell populations. Through single-cell RNA sequencing, we identified robust downregulation of the mitochondrial oxidative phosphorylation pathway in PGRN KO organoids. In line with these results, PGRN KO organoids showed decreased mitochondrial respiration. Furthermore, our study demonstrated that PGRN loss induced increased levels of reactive oxygen species (ROS), lipid peroxidation and iron accumulation. Finally, we observed increased vulnerability to ferroptotic cell death in PGRN KO organoids. Our findings suggest that mitochondrial dysfunction and impaired responses to oxidative stress are early manifestations of PGRN loss, and offer insights into the molecular mechanisms driving neurodegeneration caused by PGRN deficiency.

2.2 Introduction

Neuronal ceroid lipofuscinosis (NCL) and frontotemporal dementia (FTD) are two debilitating neurodegenerative disorders that are caused by mutations in *GRN* in a gene-dose effect. The majority are loss-of function mutations that result in nonsense-mediated mRNA decay (8). Heterozygous *GRN* mutations result in PGRN haploinsufficiency and cause FTD-GRN, which accounts for up to 11.7% of FTD cases (4,5,8). NCL is a group of lysosomal storage disorders, and the complete absence of PGRN due to *GRN* homozygous mutations leads to neuronal ceroid lipofuscinosis type 11 (CLN11), a rare type of NCL (11,14). Although the clinical manifestations of these diseases are distinct, they share some common pathological features such as lipofuscin accumulation, impaired lysosomal function, neuroinflammation and gliosis (18,19). Additionally, mutations that decrease progranulin levels are associated with

enhanced susceptibility to neurodegenerative diseases, including Parkinson's disease (PD) (20), amyotrophic lateral sclerosis (ALS) caused by repeat expansions in the *C9ORF72* (21) and Alzheimer's disease (AD) (9,23), suggesting an important role of PGRN in neurodegenerative diseases.

Progranulin is a multifunctional intracellular and secreted protein expressed in neurons, microglia, endothelial cells and astrocytes in the central nervous system (CNS). In the CNS, progranulin acts as a neurotrophic factor, regulates lysosomal function and controls inflammation (9,40,78). Nevertheless, there is currently limited understanding of the cellular and molecular pathways that lead from PGRN deficiency to neurodegeneration.

Human brain organoids derived from induced pluripotent stem cells (iPSC) are a powerful tool for modeling neurodegenerative diseases, as they allow examination of the initial pathological events that occur before the onset of neurodegeneration. Moreover, compared to traditional 2D cultures, 3D cerebral organoids provide a more physiologically relevant environment that mimics the cellular heterogeneity and complex architecture of the human brain (113,114). PGRN deficient iPSC-derived neurons and 3D co-cultures of neurons and astrocytes recapitulate some pathological hallmarks of FTD-GRN and NCL, such as TDP-43 mislocalization and hyperphosphorylation, enlarged lysosomes and lysosomal lipofuscin accumulation (72,115,116). However, most 2D models not display many aspects of TDP-43 pathology seen in FTD-GRN patients, which suggests that PGRN induces pathology in a non-cell autonomous way (115). Indeed, *GRN* deletion in only microglia or neurons is not sufficient to cause CLN11-like pathology (117,118), and PGRN astrocytes can induce toxicity in control neurons (111,119), supporting that hypothesis.

In this study, we utilized iPSC-derived forebrain organoids to model progranulin deficiency. Our use of this model in studying the effects of PGRN loss provides insights that might be pronounced or absent in simpler models. We performed single-cell RNA sequencing (scRNA-seq) in forebrain organoids derived from *GRN* homozygous knockout (PGRN KO) and control (Ctrl) iPSC lines. Our results uncovered significant downregulation of genes related to mitochondrial oxidative phosphorylation in PGRN KO organoids. Consistent with these findings, PGRN KO organoids exhibited reduced mitochondrial respiration. Moreover, PGRN-deficient organoids showed increased susceptibility to ferroptotic cell death, accompanied by ferroptosis hallmarks including reduced GPX4 expression, iron accumulation, and increased lipid peroxidation. Our results demonstrate a critical link between PGRN, mitochondrial function and ferroptosis, and suggest that mitochondrial dysfunction might contribute to neuronal cell loss in neurodegeneration caused by *GRN* loss-of-function mutations.

2.3 Methods

Human iPSC lines and culture

PGRN KO ($GRN^{-/-}$) and Ctrl ($GRN^{+/+}$, isogenic control) human iPSC were both generated in the WTC11 background. Ctrl contains a TdTom under *TMEM119,* and it was generated from WTC11. PGRN KO iPSC line was generated by Dr. Bruce R. Conklin (Gladstone Institutes, UCSF) (115) by mutagenizing WTC11 iPSC by dual Cas9 D10A nickase in the exon 12, which resulted in a 10 base pair deletion in one allele, and a 7 bp insertion plus a 1 bp mutation in the second allele (Figure 2.1 A). Human iPSCs were cultured in mTeSR

Plus medium (STEMCELL Technologies) in 6-well plates (Corning) coated with Matrigel (Corning). Medium was changed daily, and cells were passed with ReleSR (STEMCELL Technologies) when 70-80% confluent.

Human forebrain organoids generation

For the generation of human forebrain organoids, we followed previously described protocols (114,120) with a few modifications. On day 0, hiPSC were dissociated into single cells with Accutase (STEMCELL Technologies), then seeded into AggreWell 800 Microwell plates (STEMCELL Technologies). 3 x 10^6 cells were seeded per well in mTeSR Plus medium plus 10 nM ROCK inhibitor. After 24h, embryoid bodies were collected from the wells and transferred to a 10 cm dish treated with Anti-Adherence Rinsing solution (STEMCELL Technologies) in Neural Induction Medium (NIM), containing DMEM/F12 (Gibco) as the base, plus 1X GlutaMAX Supplement (Gibco), 1X MEM Non-Essential Amino Acids (Gibco), 20% KnockOut Serum Replacement (Gibco), 1x Antibiotic-Antimycotic (Gibco), 0.1 mM 2-mercaptoethanol, 5 uM dorsomorphin (Sigma), 10 uM SB-431542 (Tocris), and 2.5 uM XAV-939 (Tocris). Human cortical organoids (hCO) and human ventral organoids (hVO) were fed daily with NIM from days 1-5, and 5 μM IWP-2 was added to medium on days 4-6 only for hVO. On day 6, organoids were transferred to Neural Differentiation Medium (NM), containing Neurobasal-A (Gibco), B-27 supplement without vitamin A (Gibco), 1x GlutaMax, and 1x Antibiotic-Antimycotic, supplemented with 20 ng/ml EGF (R&D Systems) and 20 ng/ml FGF2 (R&D Systems). hCO organoids were fed daily with NM plus FGF2 and EGF from days 6-15, and every other day from days 16-24. For hVO organoids, NM was also supplemented with 5 uM IWP-2 (Selleckchem) from days 6-11; 5 uM IWP-2, 100 nM SAG

(Selleckchem) and 100 nM RA (Sigma) from days 12-14; 5 uM IWP-2, 100 nM SAG, 100 nM RA and 100 nM AlloP (Selleckchem) on day 15; and 5 uM IWP-2, 100 nM SAG, and 100 nM AlloP from days 16-24. Medium was changed daily for hVO from days 6-24. For both hCO and hVO, NM was supplemented with 20 ng/ml BDNF (Peprotech) and 20 ng/ml NT3 (Peprotech) from days 25-43, with medium changes every other day. From day 43 on, hCO and hVO organoids were maintained in NM without additional supplements and fed every 4 days. For functional experiments, only hCO were used. For scRNA-seq, hCO and hVO were fused at D60.

Dissociation of organoids

Organoids were dissociated utilizing the Worthington Papain Dissociation System (Worthington Biochemical). Briefly, each organoid was incubated at 37ºC for 30 min in a solution of papain plus DNase, after which they were triturated every 10 min with a 1000 ul pipette tip until the whole tissue was dissociated (about 4-5 cycles of trituration). The single cell solution was then mixed with an albumin-ovomucoid inhibitor solution plus DNase and pelleted with centrifugation at 300 RCF for 5 min. Cell were then used for scRNA-seq library construction or functional experiments. Organoids used for scRNA-seq were 6 months old, and for functional experiments, 5-7 months old. For functional experiments, at least 5 organoids were pooled for each dissociation. Cells were resuspended in DMEM/F12 plus 10% FBS, and plated in glass-bottom 8-well chambers (IBIDI) coated with 50 ug/ml PDL, at a density of approximately 200k cells/cm^2. On the next day, medium was replaced with BrainPhys Neuronal Medium (STEMCELL Technologies) supplemented with 1% N2 Supplement-A, 2% NeuroCult SM1 Neuronal Supplement, 20 ng/ml GDNF, 20 ng/ml

BDNF, 1 mM dibutyryl-cAMP and 200 nM ascorbic-acid (supplements were purchased from STEMCELL Technologies), plus 1x Antibiotic-Antimycotic. Cells were maintained in BrainPhys and half medium was changed every 5 days. Experiments were performed within 14 and 21 days after plating.

Single-cell RNA Sequencing (scRNA-seq)

Sample processing and library preparation

For scRNA-seq, we utilized 3 fused (hCO + hVO) organoids of each genotype - PGRN KO and Ctrl, at age 6 months. Organoids were dissociated into single cells as described above. After dissociation, cells were resuspended in a PBS + 0.04% BSA solution, filtered through a 70 um Flowmi cell strainer (Sigma), and cell concentration and viability were determined with trypan blue. The average number of cells per organoid was 3.39×10^5 +/- 7.99×10^4 cells, and cell viability was >95% for all organoid samples. Cells were then labelled with Cell Multiplexing Oligos from the 10x Genomics 3' CellPlex Kit (10x Genomics), which allowed cells from different samples to be pooled together prior to loading into a 10x Genomics chip. The 6 samples were pooled together, and about 43,000 cells were loaded into ChipG in order to reach a targeted cell recovery of 30,000 cells. Gel In-Bead Emulsion (GEMs), and 3' Gene Expression and Cell Multiplexing Libraries were generated using the Chromium Next GEM Single Cell 3' GEM, Library & Gel Bead Kit v3.1 (Dual Index) with 3' Feature Barcode kit for Cell Multiplexing (10x Genomics). Libraries were sequenced on the Illumina NovaSeq 6000 at the UC Davis DNA Technology Core, with a depth of ~42k reads per cell.

Counts matrix generation and quality control

Demultiplexed FASTQ files were aligned to the GRCh38 genome (reference refdata-gex-GRCh38-2020-A) with CellRanger v6.1.1 using the CellRanger Multi pipeline, using default parameters. Downstream analysis was performed with Seurat 4.4 in RStudio 4.3.1. The preprocessed counts matrix was transformed into a Seurat object for each sample. Only cells that expressed more than 1,300 and less than 9,000 genes, and less than 50,000 UMIs were considered for the downstream analysis. We also removed damaged cells with miQC package (121), which combines information about mitochondrial percentage and library complexity (number of genes), by filtering out cells with 75% or higher probability of being compromised. We did not check for doublets, as doublet detection tools tend to remove cells with intermediate or continuous phenotypes. After quality control analysis, we obtained a total of 9,316 cells (1,553 +/- 284 cells per sample).

Data processing, clustering, and cell type identification

The UMI counts were normalized and scaled using the SCTransform function in Seurat. To correct for batch effects, we performed sample integration using the 3000 most variable genes (nfeatures) identified by SCTransform. Cells were clustered based on the first 100 principal components (PCs), chosen based on the elbow plot, and using a resolution of 0.6. Data were visualized in 2 dimensions with Uniform Manifold Approximation and Projection (UMAP) using the same PCs. Clustering using these parameters resulted in the identification of 18 clusters. Two small clusters that contained less than 10 cells in two or more organoids were removed from analyses. Cluster markers were identified using the FindAllMarkers function using the Wilcoxon Rank Sum test, log(fold change) threshold of 0.25, min.pct of 0.25, and min.diff.pct of 0.2. FDR-corrected p-values of ≤ 0.05 were considered significant. Cell-type annotation was performed manually based on established marker genes, on the

PanglaoDB scRNA-seq database (122), on the gene list enrichment analysis tool Enrichr (123), and based on developing brain and organoid-specific scRNA-seq datasets (113,124–126).

Differential gene expression analysis and gene ontology (GO)/pathway enrichment analysis

Following cell type identification, each set cell cluster was subset, and differential gene expression was performed. Differentially expressed genes (DEG) for each cell cluster between PGRN KO and Ctrl organoids were identified with the FindMarkers function, using Wilcoxon Rank Sum test, 0.25 as the log2(fold change) threshold, and FDR-corrected p-value of ≤ 0.05. Ribosomal genes (RPS- and RPL-) were removed from analysis. Enrichment analysis for gene ontology (GO) terms and pathways among DEGs was performed using EnrichR (123) and Metascape (127). Gene set expression scores were calculated using the AddModuleScore function in Seurat, with default parameters.

RT-qPCR

To quantify *GRN* mRNA, total RNA was extracted from organoids using PureLink RNA Mini Kit (ThermoFisher), and cDNA synthesized with the ProtoScript II First Strand cDNA Synthesis Kit (NEB). qPCR was performed on an Applied Biosystems QuantStudio 6 Pro Real-Time PCR System, using TaqMan probes (ThermoFisher) specific for *GRN* (Hs00963707_g1) and for *PPIA* (endogenous reference, Hs99999904_m1). Expression fold change was calculated using the $\Delta\Delta$Ct method.

Cellular ROS

For reactive oxygen species (ROS) detection, we used CellROX Green (Invitrogen), a fluorescent probe used to measure mitochondrial and nuclear ROS. Dissociated organoid cells

were incubated in fresh medium plus 5 uM CellROX Green reagent for 30 min at 37 ºC. Cells were washed twice with PBS, fresh culture media plus 0.5 ug/ml Hoechst 33342 was added, and live cells were imaged immediately.

Lipid peroxidation

The lipid peroxidation sensor BODIPY 581/591 C11 (Invitrogen) was used to detect in-situ lipid peroxidation in live cells. Dissociated organoid cells were incubated in fresh medium containing 5 μM of BODIPY C11 and 0.5 ug/ml Hoechst 33342 at 37 °C for 30 min. Cells were washed twice with PBS, fresh culture media was added, and cells were imaged immediately. Media was then replaced with fresh media plus 100 uM cumene hydroperoxide (Sigma). Cells were incubated for 3 hours, then imaged again in the fileds of view. In the analysis, the oxidized/reduced fluorescence ratio of BODIPY-C11 was used to normalize for cell incorporation of the probe into membrane.

Intracellular labeling of ferrous iron

FerroOrange was used to detect intracellular Fe^2 in live cells. Dissociated organoids were incubated in fresh medium containing 1 μM of FerroOrange (Dojindo) and 0.5 ug/ml Hoechst 33342 at 37 °C for 30 min, and cells were imaged immediately. For assessment of FerroOrange in neurons, dissociated organoid cells were incubated with 5 uM AraC from D1 post-dissociation until the day of the assay (21 days), to eliminate mitotic cells and keep only post-mitotic neurons. Neurons were imaged with FerroOrange, 0.1 μM NeuO (STEMCELL Technologies) and Hoechst 33342.

Cell death analysis

Analysis of dell death by ferroptosis was performed by incubating dissociated organoid cell cultures with 100 uM cumene hydroperoxide for 2-3 hours at 37ºC. Cells were washed twice with PBS, then incubated with fresh media plus 10 ug/ml 7-AAD (Sigma) for 15 min at 37ºC. Cells were fixed in 4% PFS for 10 min at room temperature (RT), washed 3x with PBS, then mounted with Prolong Diamond Antifade Mountant (Invitrogen).

Immunofluorescence and immunohistochemistry of organoid cryosections and 2D cultures

Whole organoids were fixed in PFA 4% for 1h at RT, washed 3x with PBS, and then cryopreserved by overnight incubation at 4ºC in a solution of 30% sucrose in PBS. Cryopreserved organoids where then embedded in Neg-50 Frozen Section Medium (Epredia), flash frozen in dry ice, and stored at -80º C. Frozen organoids were sectioned in 20µm slices in a Leica Cryostat CM1850. 2D dissociated organoid cultures were fixed with 4% PFA for 10 min at RT, then washed 3x with PBS.

For immunofluorescence, fixed organoid cryoslices and 2D dissociated organoid cultures were incubated in blocking buffer containing PBTA (0.5% BSA and 0.1% Triton X-100 in PBS) plus 5% normal goat or donkey serum for 1h at RT. Samples were then incubated with primary antibodies in blocking buffer overnight at 4ºC, washed three times with PBTA, then incubated with secondary antibodies in blocking buffer for 1h at RT. Samples were washed three times with PBTA, then mounted with Prolong Diamond Antifade Mountant (Invitrogen) with or without DAPI for nuclei staining.

For immunohistochemistry, after inactivation of endogenous peroxidases (3% hydrogen in PBS), antibody specific antigen retrieval was performed, and cryosections were blocked and afterwards incubated with the primary antibody for 1 hour. Sections were then incubated with rabbit anti-Goat IgG (H+L) secondary antibody, HRP (Invitrogen 31402, 1:500). Next, for detection of specific binding, the mouse and rabbit specific HRP/DAB IHC detection Kit micro-polymer (Abcam ab236466) was used which contains secondary antibodies and DAB to produce a dark brown color. Sections were then counter-stained with hematoxylin, dehydrated and cover slipped with permanent mounting agent.

The following primary antibodies were used: goat anti-PGRN (R&D Systems AF2420, 1:700), rabbit anti-SATB2 (Abcam ab34735, 1:100), rat anti-CTIP2 (Abcam ab18465, 1:200), guinea-pig anti-MAP2 (Synaptic Systems 188004, 1:500), mouse anti-TUJ1 (Sigma T8578, 1:500), chicken anti-GFAP (Abcam ab4674, 1:500), rabbit anti-TBR1 (Abcam 31940, 1:500), mouse anti-CUX1 (Abcam 54583, 1:500), rabbit anti-SOX2 (Sigma ab5603, 1:500), mouse anti-TOM20 (Santa Cruz sc17764, 1:500), rabbit anti-GPX4 (Abcam ab125066, 1:500), mouse anti-NeuN (1:1,000). The following secondary antibodies were used: goat anti-rabbit Alexa Fluor 488 (ThermoFisher A-11008), goat anti-guinea pig Alexa Fluor 594 (ThermoFisher A-11076), goat anti-rat Alexa Fluor 647 (ThermoFisher A-21247), goat anti-mouse AlexaFluor 555 (ThermoFisher A-21422), goat anti-chicken Alexa Fluor 647 (ThermoFisher A-21449), goat anti-mouse Alexa Fluor 647 (ThermoFisher A-21235). Secondary antibodies were used at a dilution of 1:1,000.

Image acquisition and analysis

Samples were imaged using a Leica SP8 confocal microscope, and image analysis was done in ImageJ2 (Fiji) software v2.14.0. Background was subtracted from each image. TOM20, CellROX and FerroOrange fluorescence intensities were quantified by thresholding the targeted channel, and measuring the integrated density (IntDen) for the region of interest (ROI) in the field of view (FOV). IntDen was then normalized by the number of cells, equivalent to the number of DAPI-positive nuclei, in each FOV. For FerroOrange intensity analysis in neurons, the NeuO channel was thresholded and applied as a mask in the FerroOrange channel, and the mean fluorescence intensity of FerroOrange was measured in the ROI. For GPX4 intensity analysis, the MAP2 channel was thresholded and applied as a mask in the GPX4 channel. The IntDen was measured in the GPX4 channel for the ROI, and the value was normalized by the number of cells in each FOV. For quantification of BODIPY-C11, the images of oxidized and reduced BODIPY-C11 were first thresholded, and IntDen was measured for the ROIs. The ratio of oxidized/reduced BODIPY-C11 was calculated by calculating the ratio of oxidized/reduced BODIPY-C11 IntDen, in order to normalize for cell incorporation of the probe into membrane. For cell death analysis, the number of DAPI+ and 7-AAD positive were calculated for each FOV, and cell viability calculated as 1-(number of 7-AAD+ nuclei/number of DAPI+ nuclei) x 100.

Oxygen consumption rate

The oxygen consumption rate (OCR) and the extracellular acidification rate (ECAR) were measured in a Seahorse XF96 Extracellular Flux Analyzer (Agilent Technologies). Organoids were dissociated, and a total of $3x10^5$ cells/well were seeded on a Seahorse XF96 plate and cultured for 2 weeks. On the day of the assay, cells were washed with assay medium

(DMEM assay medium supplemented with 5 mM HEPES, 5 mM glucose, 2 mM glutamine, and 1 mM sodium pyruvate; pH 7.4). Compounds were injected sequentially during the assay resulting in final concentrations of 2 μM oligomycin (Port A), 0.75 μM FCCP (Port B), 1.35 μM FCCP (Port C), and 1 μM rotenone and 2 μM antimycin (Port D). OCR and ECAR were measured in parallel. Seahorse data were normalized to cell number by counting the number of nuclei stained with 1μg/mL Hoechst. Nuclei counts and analysis were completed on an Operetta High-Content Imaging System (PerkinElmer). ATP production rates were calculated as described by Divakaruni et al. (JBC, 2017).

2.4 Results

Generation and single-cell RNA-seq of PGRN KO and isogenic control cerebral organoids

Given the heterogeneity of expression and effects of PGRN in the CNS, we chose a human forebrain organoid model to study the effect of loss of PGRN in human brain cells. Organoids were generated for two human iPSC lines – PGRN KO (*GRN*$^{-/-}$), and an isogenic control – Ctrl (*GRN*$^{+/+}$). Both iPSC lines were generated in the WTC11 iPSC background, which was mutagenized to generate the PGRN KO iPSC (115) (Figure 2.1 A). Human cortical organoids (hCO) and ventral organoids (hVO) were differentiated following a directed-differentiation protocol (114,120), then fused for the subsequent scRNA-seq analyses. Knockout of *GRN* was confirmed on mRNA and protein expression levels (Figure 2.1 B, C). Cerebral organoids displayed the expected morphology and cell-type markers at 6 months (Figure 2.1 D). We chose this time point since it has been shown that 6-month organoids

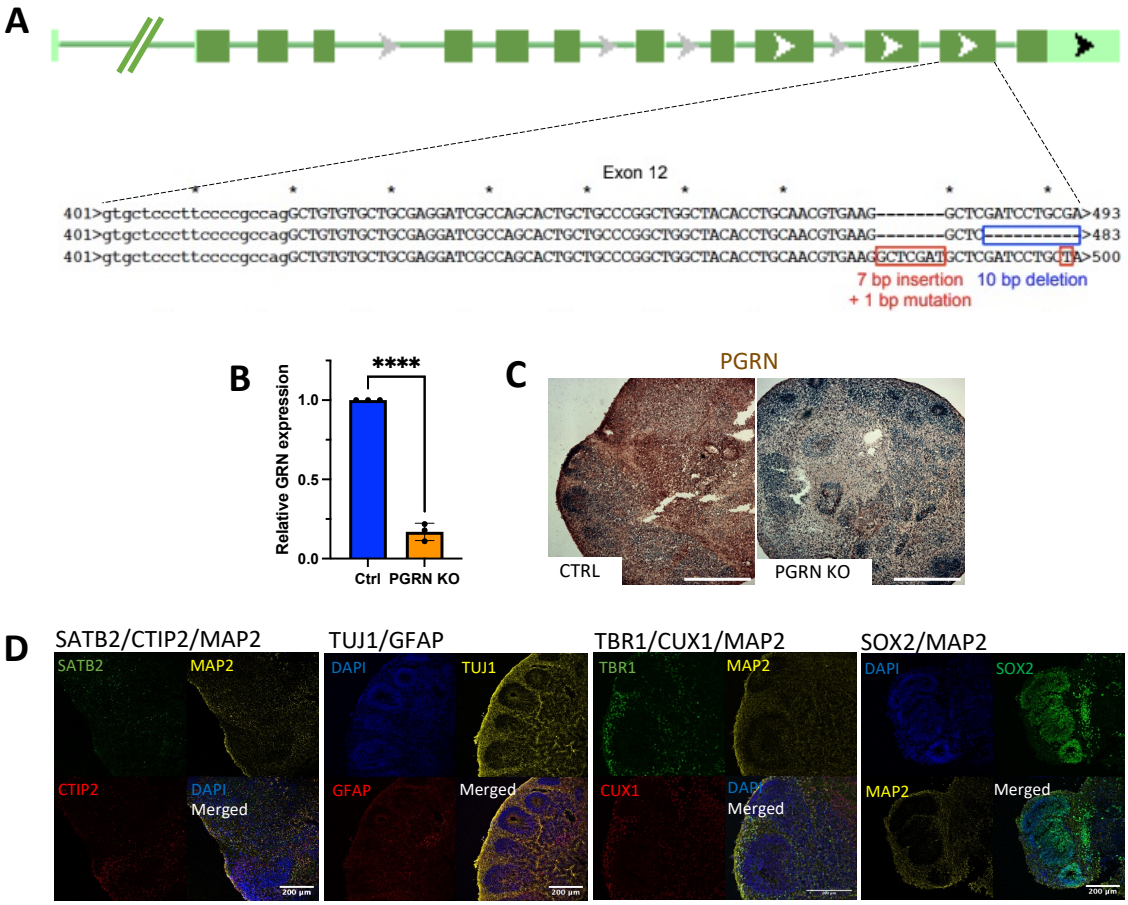

Figure 2.1 - Characterization of PGRN KO and Ctrl human brain organoids

A – Diagram of the *GRN* gene, which contains 13 exons. The *GRN* region that was modified is depicted. The modification was generated by dual Cas9 D10A nickase in the exon 12, and resulted in a 10 base pair deletion in one allele, and a 7 bp insertion plus a 1 bp mutation in the second allele.

B – *GRN* mRNA expression in PGRN KO and Ctrl organoids. qPCR was performed using mRNA from 3 organoids from 3 different batches, for each genotype, and *GRN* expression was normalized with *PPIA*. Statistical significance was calculated by two-tailed unpaired *t*-test. Bars and error bars represent means ± SEM. $^{*}p \leq 0.1$, $^{**}p \leq 0.01$, $^{***}p \leq 0.001$, $^{****}p \leq 0.0001$.

C – Immunohistochemistry representative images showing expression levels of PGRN in CTRL and PGRN KO brain organoids (scale bars = 500 µm).

D – Images of 6-month-old organoid sections immunostained for surface-layer (SATB2) and deep-layer (CTIP2) neuronal markers, astrocytic marker GFAP and neuronal marker TUJ1, deep-layer (TBR1) and surface-layer (CUX1) neuronal markers, neural stem/progenitor cell marker SOX2 and neuronal marker MAP2.

present a higher variety of cell types and a larger proportion of neurons than younger organoids (114,120). Single-cell RNA-seq libraries were generated using the 10X Genomics platform (Figure 2.2 A). Three 6-month old fused organoids from each genotype were sequenced, and following quality control analyses, we obtained a total of 9,316 cells (1,553 +/- 284 cells per sample).

Unsupervised clustering of cells based on their transcriptomic profiles resulted in the detection of 18 distinct clusters that were labeled as 16 major cell types based on expression of unique markers (Figure 2.2 B, D), which aligns with findings from other scRNA-seq studies on human brain organoids (113,124,125). We identified three clusters of glutamatergic cortical neurons (CN), all expressing markers such as *NEUROD6*, *NEUROD2*, *STMN2*, *BCL11B*, *TBR1*, *MAPT* and *DCX*. CN-1 expressed high levels of genes such as *FEZF2* and *SYT4*; CN-2 showed high expression of genes such as *SOX11* (early neuronal marker) and *SATB2*; and CN-3 was characterized by high expression of *SATB2*, among other genes. GABAergic interneurons (IN) expressed high levels of markers such as *DLX1*, *DLX2*, *GAD1* and *GAD2*. We also found a population of unidentified neurons (N) expressing neuronal markers genes such as *GRIN2B*, *PCLO*, *ANK3* and *MAPT*. Intermediate progenitor neurons (IPC) showed high expression of markers such as *EOMES*, *ELAVL4*, *NHLH1* and *PPP1R17*. Neuroepithelial cells (NEC) formed 3 clusters (NEC-1, NEC-2 and NEC-3) and expressed high levels of cell-cycle related genes, such as *HMGB2*, *TOP2A*, *HELLS* and *CENPF*. Astrocytes (AST) expressed high levels of canonical markers such as *NDRG2*, *S100B*, *GJA1* and *AQP4*. Radial glial cells (RGC) formed a cluster characterized by high expression of genes such as *PAX6*, *HOPX*, *TNC*, *VIM*, *GLI3*, *PTPRZ1* and *SLC1A3*. Oligodendrocyte progenitor cells (OPC) expressed genes such as *OLIG1*, *OLIG2*, *DCX1*, *DCX2*, and *PDGFRA*. Glial progenitor cells

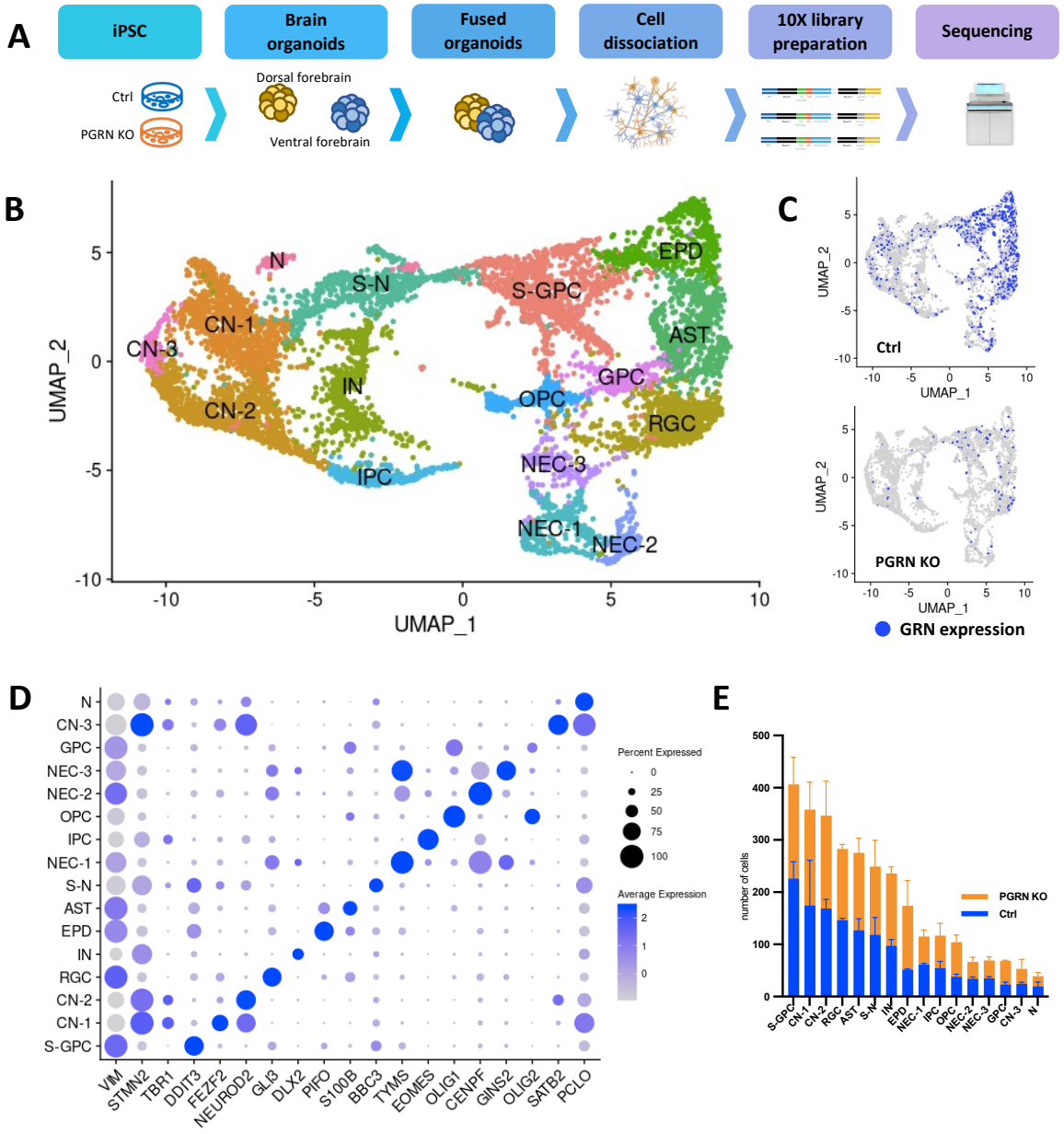

Figure 2.2 – Cellular composition of PGRN KO and Ctrl organoids upon scRNA-seq analysis

A – Schematic illustration of the sample material and scRNA-seq workflow.

B – UMAP of 8975 cells from six PGRN KO and Ctrl brain organoids. Clusters that had less than 10 cells in more than 2 organoids were removed – one cluster of interneurons and a cluster of mesenchymal cells, totaling 98 cells.

C – UMAP of PGRN KO and control organoids, with *GRN* expression highlighted in blue.

D – Dot plot showing expression of selected markers genes in each cell cluster.

E – Bar plot of proportions of major cell types in PGRN KO and control organoids. There was not significant difference of number of cells of each cell type between PGRN KO and Ctrl

organoids. Statistical significance was calculated by 2-way ANOVA with Sidak multiple comparisons test. Bars and error bars represent means ± SEM.
CN – cortical glutamatergic neurons, IN – gabaergic interneurons, IPC – intermediate progenitor cells, N – unidentified neurons, S-N – stressed neurons, GPC – glial progenitor cells, S-GPC – stressed glial progenitor cells, EPD – ependymal cells, AST – astrocytes, OPC – oligodendrocyte precursor cells, RGC – radial glial cells, NEC – neuroepithelial cells.

(GPC) were characterized by intermediate expression of OPC and RGC/astrocyte genes. Stressed glial progenitor cells (S-GPC) expressed intermediate levels of RGC/astrocyte markers such as *VIM*, *SLC1A3*, *TNC* and *PAX6*, no expression of OPC genes, and showed high expression of unfolded protein response (UPR) genes (e.g. *DDIT3*, *DDIT4*, *CRYAB*, *P4HB*, *SLC3A2*). We found a population of cells expressing intermediate levels of neuronal markers such as *BCL11B*, *STMN2*, *SNAP25* and *SYT4*, that also showed high expression of the same S-GPC UPR genes and high expression of other UPR genes such as *HERPUD1* and *BBC3*. We called this population "stressed neurons" (S-N). The unfolded protein response is a stress response pathway that regulates the endoplasmatic reticulum homeostasis. Similar populations of stressed cells that show upregulation of the UPR have been found in previous single-cell RNAseq organoid studies (113,124), and they most likely represent cells that have been affected by the lack of oxygen supply due to the absence of vascularization of brain organoids (113,124). Finally, we identified a population of ependymal cells, characterized by high expression of markers such as *FOXJ1*, *PIFO* and *DYNLRB2*. Two small clusters of GABAergic neurons and mesenchymal cells, that contained less than 10 cells in two or more organoids, were removed from analyses. *GRN* was expressed in all cell types in our dataset, but mainly glial cells (Figure 2.2 C). All known major cell types were detected in both PGRN KO and Ctrl organoids, with consistent numbers across samples (Figure 2.2 E).

Dysregulation of oxidative phosphorylation system in PGRN KO organoids

In order to identify dysregulated genes related to PGRN loss, we performed differential gene expression analysis between PGRN KO and Ctrl organoids for each identified cell type (absolute log2FC > 0.25, adjusted p-value < 0.05), and then conducted gene set enrichment analysis to identify biological processes and pathways that were overrepresented among the differentially expressed genes (DEG).

We found that the most significant dysregulated pathway of downregulated genes in all cell types was cellular respiration, also called mitochondrial oxidative phosphorylation (OXPHOS) (Figure 2.3 A, C). The OXPHOS system is the final biochemical process in the production of ATP, and is composed of the electron transport chain (ETC), a set of five multiprotein enzyme complexes localized in the inner mitochondrial membrane that are encoded by genes in the mitochondrial or nuclear DNA (128). The ETC creates a proton gradient utilized to generate ATP production, and produces electron carriers (e.g. NAD+ and FAD) that are essential for glycolysis and the tricarboxylic acid (TCA) cycle. In our study, all dysregulated genes in this pathway were nuclear-encoded genes that encode for components of the complexes I (NADH dehydrogenase), III (cytochrome bc1 complex), IV (cytochrome c oxidase) and V (ATP synthase) of the mitochondrial ETC, and most of them overlapped in all the cell types (Figure 2.3 B, OXPHOS genes in astrocytes and neurons). After finding this major dysregulation of mitochondrial respiration genes in PGRN KO organoids, we then focused the differential gene expression analysis in neurons and astrocytes (Figure 2.3 C, D), considering these are cell types that have been shown to be heavily affected by progranulin deficiency (9,111,115,119).

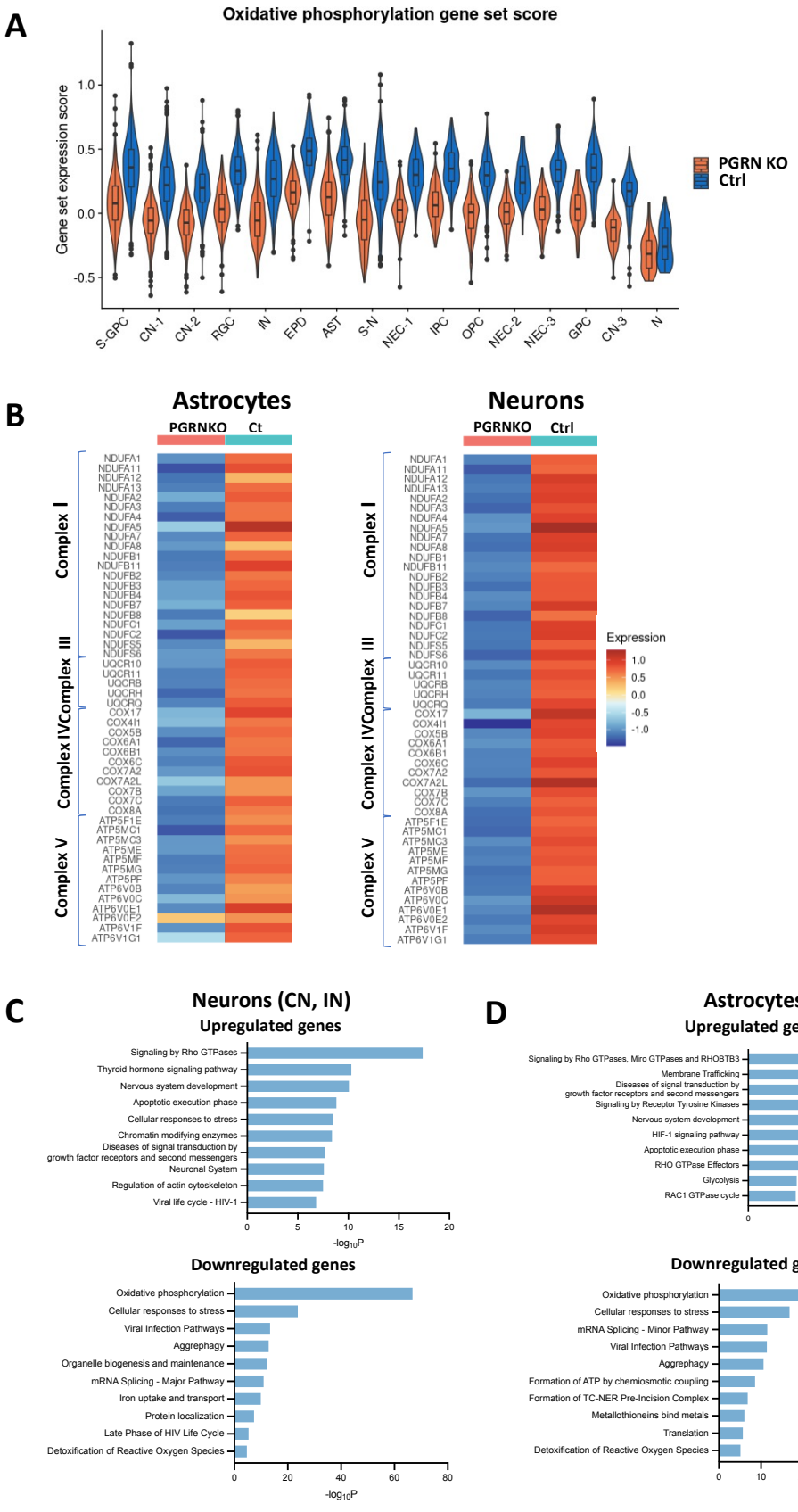
A
Oxidative phosphorylation gene set score
Gene set expression score
1.0
0.5
0.0
-0.5
S-GPC
CN-1
CN-2
RGC
IN
EPD
AST
S-N
NEC-1
IPC
OPC
NEC-2
NEC-3
GPC
CN-3
N
PGRN KO
Ctrl
B
Astrocytes
PGRNKO
Ct
Neurons
PGRNKO
Ctrl
Complex I
Complex III
Complex IV
Complex V
NDUFA1
NDUFA11
NDUFA12
NDUFA13
NDUFA2
NDUFA3
NDUFA4
NDUFA5
NDUFA7
NDUFA8
NDUFB1
NDUFB11
NDUFB2
NDUFB3
NDUFB4
NDUFB7
NDUFB8
NDUFC1
NDUFC2
NDUFS5
NDUFS6
UQCR10
UQCR11
UQCRB
UQCRH
UQCRQ
COX17
COX4I1
COX5B
COX6A1
COX6B1
COX6C
COX7A2
COX7A2L
COX7B
COX7C
COX8A
ATP5F1E
ATP5MC1
ATP5MC3
ATP5ME
ATP5MF
ATP5MG
ATP5PF
ATP6V0B
ATP6V0C
ATP6V0E1
ATP6V0E2
ATP6V1F
ATP6V1G1
Expression
1.0
0.5
0.0
-0.5
-1.0
C
Neurons (CN, IN)
Upregulated genes
Signaling by Rho GTPases
Thyroid hormone signaling pathway
Nervous system development
Apoptotic execution phase
Cellular responses to stress
Chromatin modifying enzymes
Diseases of signal transduction by growth factor receptors and second messengers
Neuronal System
Regulation of actin cytoskeleton
Viral life cycle - HIV-1
0
5
10
15
20
-log10P
Downregulated genes
Oxidative phosphorylation
Cellular responses to stress
Viral Infection Pathways
Aggrephagy
Organelle biogenesis and maintenance
mRNA Splicing - Major Pathway
Iron uptake and transport
Protein localization
Late Phase of HIV Life Cycle
Detoxification of Reactive Oxygen Species
0
20
40
60
80
-log10P
D
Astrocytes
Upregulated genes
Signaling by Rho GTPases, Miro GTPases and RHOBTB3
Membrane Trafficking
Diseases of signal transduction by growth factor receptors and second messengers
Signaling by Receptor Tyrosine Kinases
Nervous system development
HIF-1 signaling pathway
Apoptotic execution phase
RHO GTPase Effectors
Glycolysis
RAC1 GTPase cycle
0
10
20
30
-log10P
Downregulated genes
Oxidative phosphorylation
Cellular responses to stress
mRNA Splicing - Minor Pathway
Viral Infection Pathways
Aggrephagy
Formation of ATP by chemiosmotic coupling
Formation of TC-NER Pre-Incision Complex
Metallothioneins bind metals
Translation
Detoxification of Reactive Oxygen Species
0
10
20
30
40
50
-log10P

Figure 2.3 – Pathway enrichment analysis and downregulation of OXPHOS in PGRN deficient organoids
A – Gene expression scores for the OXPHOS gene set for all cell types.
B – Heatmap of expression levels of DEG involved in OXPHOS in astrocytes and neurons.
C – Bar graph of the top 10 enriched pathways (KEGG and Reactome pathways) across DEGs between PGRN KO and Ctrl neurons (CN + IN). DEGs comprised 539 upregulated and 280 downregulated genes.
D – Bar graph of the top 10 enriched pathways (KEGG and Reactome pathways) across DEGs between PGRN KO and Ctrl astrocytes. DEGs comprised 584 upregulated and 225 downregulated genes.

Among the enriched pathways of downregulated genes in both astrocytes (AST) and neurons (CN, IN), aggrephagy (Figure 2.3 C, D) and mitophagy (KEGG pathways, not shown), stand out. Aggrephagy is the removal of protein aggregates by macroautophagy, and this term included the term autophagy. In line with these findings, several studies have shown that PGRN deficiency leads to impairment of autophagic flux, which leads to accumulation of TDP-43 in neurons (129,130). Mitophagy is a mechanism of removal of damaged mitochondria through autophagy. This set of genes included *GABARAPL2, GABARAP, FIS1, JUN, UBB, TOMM7* and *UBA52*. These findings also align with previous research demonstrating that PGRN deficiency impairs mitophagy (130–133).

Lysosomal lumen acidification (GO biological processes, not shown) was another enriched pathway of downregulated genes (*ATP6V0B, ATP6V0C, ATP6V1F, RNASEK*) in neurons, but not astrocytes. This result is consistent with research indicating that PGRN plays an essential role in acidification of lysosomes (67).

Pathway enrichment analysis of downregulated genes also showed that the terms “cellular response to stress” and “detoxification of reactive oxygen species” were enriched in PGRN KO neurons and astrocytes (Figure 2.3 C, D). Among those genes there were several

involved in the ubiquitin-proteasome system (*UBB, UBA52, PSMA2, ELOB, RBX1, SEM1*), suggesting proteasome dysfunction. These pathways also included antioxidant genes that were downregulated in astrocytes (*PRDX5, PRDX1, JUN, PARK7, MT3, TXN, ATOX1, HSBP1, GSTP1*) and neurons (*SOD1, ATOX1, PRDX5, PRDX2, PARK7, MT3, MIF, TXN, HSBP1, MT1F, MT2A*).

The HIF-1 signaling pathway was one of the top pathways of upregulated genes enriched in astrocytes (Figure 2.3 D) and neurons (not shown). These genes included *HIF1A, EGLN1, HK1, VEGFA, PDK1, CDKN1B* and *AKT3*. HIF-1α mediates responses to oxidative stress and hypoxia by translocation to the nucleus and mitochondria, and downregulates OXPHOS to decrease oxygen consumption (134–136). This suggests that these cells might be responding to elevated reactive oxygen species (ROS) levels. The upregulation of "cellular response to stress" and "apoptotic execution phase" genes also indicates that PGRN deficient astrocytes and neurons could be under stress, that could be leading to cell death.

We found that PGRN KO astrocytes (Figure 2.3 D), but not neurons, show upregulation of several genes involved in the glycolysis pathway (*ALDH3A2, TPI1, PKM, PGK1, ENO1, ENO2, GAPDH, PGM1, PFKP, HK1*), and the combined average expression of all genes involved in this pathway is also higher in astrocytes (Supplementary Figure 2.1). This suggests that astrocytes attempt to compensate the decreased energy production from the impaired oxidative phosphorylation by enhancing glycolysis (Warburg effect). This is also a way to support energy metabolism of neurons – lactate, produced by glycolysis in astrocytes, is taken up by neurons as an energy source (137).

Interestingly, in PGRN KO astrocytes, "stress granule assembly" was the top enriched GO biological processes term of upregulated genes (not shown), including *DDX6, DYNC1H1,*

DDX3X, YTHDF3, G3BP1, G3BP2, MAPT, BICD1. Stress granules protects cells from oxidative stress damage, and the suppression of stress granules formation by oxidative stress promotes cell death (138). These findings suggest that PGRN KO astrocytes could be able to regulate redox levels by inducing stress granule formation.

These findings establish a link between PGRN loss and mitochondrial function, energy metabolism, and stress response pathways, emphasizing OXPHOS as a prominent pathway affected by *GRN* deficiency.

PGRN loss impairs mitochondrial respiration

Given the robust effect of PGRN deficiency in the expression of OXPHOS genes, we next sought to investigate mitochondrial function in organoids. We used the Seahorse XF96 Analyzer to measure mitochondrial respiration, a reliable method to assess mitochondrial function, in organoids. Oligomycin (ATP-synthase inhibitor), FCCP (uncoupling agent) and rotenone/antimycin (complexes I and III inhibitors, respectively) were sequentially added to assess oxygen consumption rate (OCR) in different conditions. We observed that mitochondrial respiration, as measured by the OCR, was decreased in PGRN KO cells (Figure 2.4 A). More specifically, basal OCR, ATP-linked OCR, maximal respiration and reserve capacity were all significantly decreased in PGRN KO cells (Figure 2.4 B). Reserve capacity is the difference between maximal and basal respiration, and assesses the cell's capacity to respond to elevated energy demands or stress conditions. The decreased reserve capacity in PGRN KO cells indicates that these cells are more susceptible to oxidative metabolic stress. The impaired mitochondrial respiration, with a larger proportional decrease in maximal respiration, as observed in PGRN KO organoids, can be due to several factors, such as changes

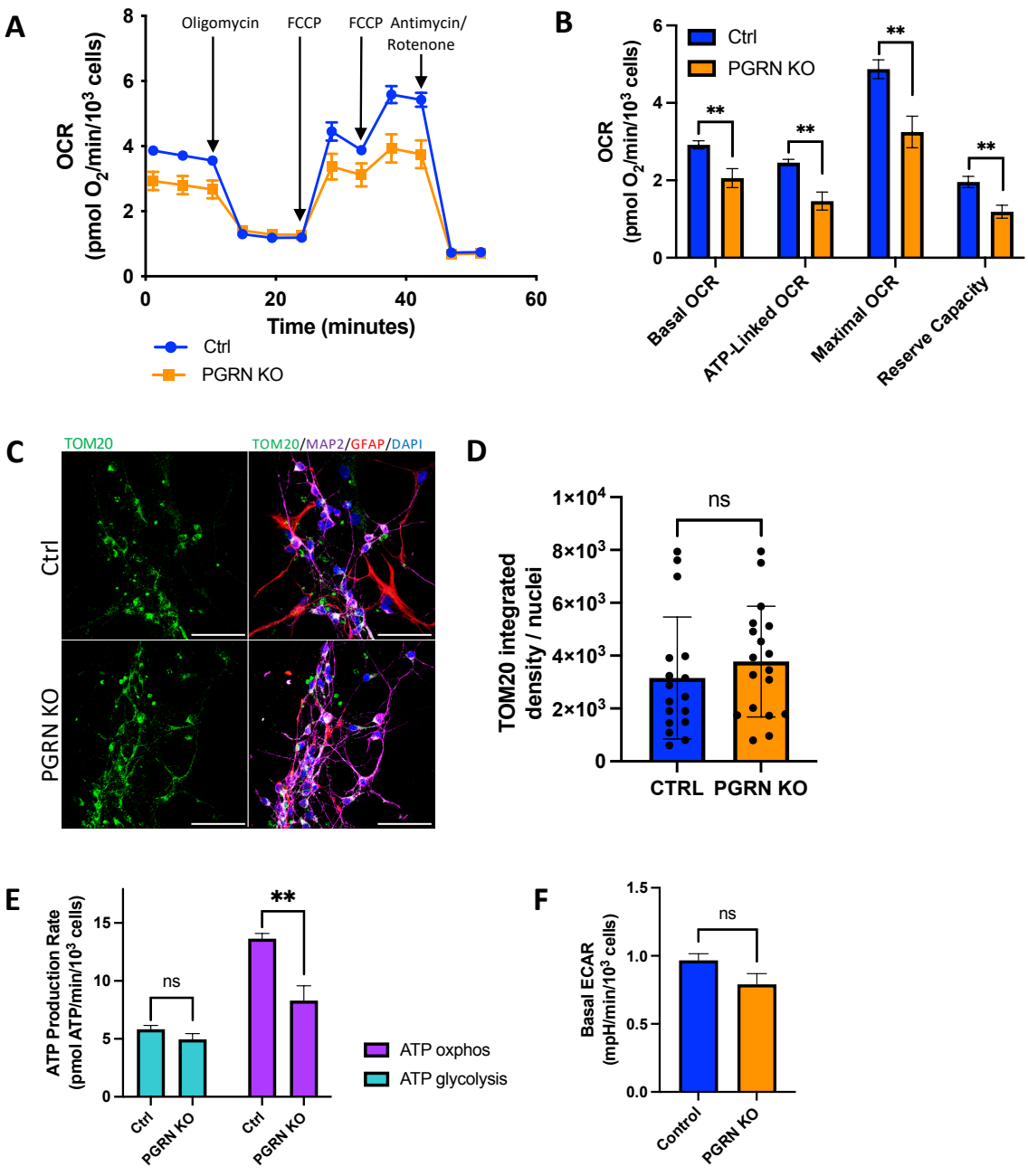

Figure 2.4 - PGRN loss impairs mitochondrial respiration in human brain organoids
A – Oxygen consumption rate (OCR) was measured in PGRN KO and Ctrl dissociated organoids by the sequential addition of specific respiratory modulators. Data represent the mean ± SEM of n=6 technical replicates obtained from the dissociation of 8 organoids per genotype. Values were normalized by the number of cells counted by DAPI fluorescence.
B – Respiratory parameters extracted from OCR.
C – Representative images of TOM20 immunostained organoid cells from PGRN KO and Ctrl organoids, co-stained with GFAP, MAP2 and DAPI. Scale bars = 50 µm.

D – Quantification of TOM20 levels in organoids, calculated as the integrated density of TOM20 fluorescence in the field of view normalized by the number of nuclei (minimum of 12 cells per field of view).
E – Rates of ATP produced from oxidative phosphorylation (obtained from OCR) and glycolysis (obtained from ECAR).
F – Extracellular acidification rate (ECAR) under basal conditions.
Statistical significance was calculated by two-tailed unpaired *t*-test. Bars and error bars represent means ± SEM. $^{*}p \leq 0.1$, $^{**}p \leq 0.01$, $^{***}p \leq 0.001$, $^{****}p \leq 0.0001$.

in mitochondrial content or respiratory chain activity (139). Since mitochondrial mass, assayed by TOM20 expression, was not different between the two genotypes (Figure 2.4 C, D), the decreased mitochondrial respiration observed is most likely due to decreased activity of respiratory chain complexes I-IV. Moreover, the ATP production rate from oxidative phosphorylation was significantly decreased in PGRN KO (Figure 2.4 E), while the ATP production rate from glycolysis (Figure 2.4 E) and the extracellular acidification rate (ECAR) (Figure 2.4 F), an indicator of glycolysis, were not different between genotypes. These results indicate that PGRN loss impacts cells energy metabolism through impairment of the OXPHOS system.

PGRN loss leads to increased oxidative stress

The mitochondrial respiratory chain is the main source of intracellular reactive oxygen species (ROS), which are produced as a byproduct of electron transfer, and perturbations in the oxidative phosphorylation system can increase the production of ROS (140). Given that we observed impairment of the OXPHOS system in mitochondria, and that transcriptomics analyses suggested a dysfunctional response to oxidative stress response in PGRN KO organoids, we sought out to investigate intracellular ROS. For that we used CellROX green, a

probe that that exhibits bright fluorescence upon oxidation by ROS and localizes in the nucleus and mitochondria. CellROX labelling demonstrated a significant higher accumulation of ROS in the PGRN KO organoid cells as opposed to controls (Figure 2.5 A, B).

Excessive ROS can cause oxidative damage on membrane lipids, DNA and proteins. Lipid peroxidation is the oxidative degradation of lipids, and its products (reactive aldehydes and lipid radicals) can further damage lipids and proteins in a chain reaction, resulting in the formation of lipofuscin – a lipid-protein aggregate and one of the hallmarks of NCL (141–143). Therefore, we investigated if PGRN loss alters cell lipid peroxidation levels (Figure 2.5 C, D). We used BODIPY 581/591 C11 as a live-cell reporter for lipid peroxidation. BODIPY C11 localizes in lipophilic membrane structures, and its oxidation shifts the fluorescent emission peak from ~590 nm (red, reduced) to ~510 nm (green, oxidized). Under baseline conditions, PGRN KO cells showed a significant increase in lipid peroxidation (ratio of oxidized/reduced BODIPY C11 fluorescence) compared to controls (Figure 2.5 C, D, left). After three hours of treatment with cumene hydroperoxide (CHP), a well characterized oxidant and lipid peroxidation inducer (144), lipid peroxidation levels increased considerably in both genotypes, and the increase was significantly higher in PGRN KO cells (Figure 2.5 C, D, right). These results suggest that PGRN loss leads to increased basal oxidative stress, indicated by increased nuclear, mitochondrial and lipid-derived ROS levels, and increased cellular vulnerability to induced oxidative stress.

Interestingly, we did not find lipofuscin buildup in PGRN KO organoids (data not shown), which contradicts findings from other studies that have reported lipofuscin accumulation in *GRN*$^{-/-}$ iPSC-derived neurons (72,116). This suggests that, in our model,

lipofuscin accumulation could be a later event because of increased oxidative stress, as it's been shown in aged *GRN*$^{-/-}$ mouse models (30).

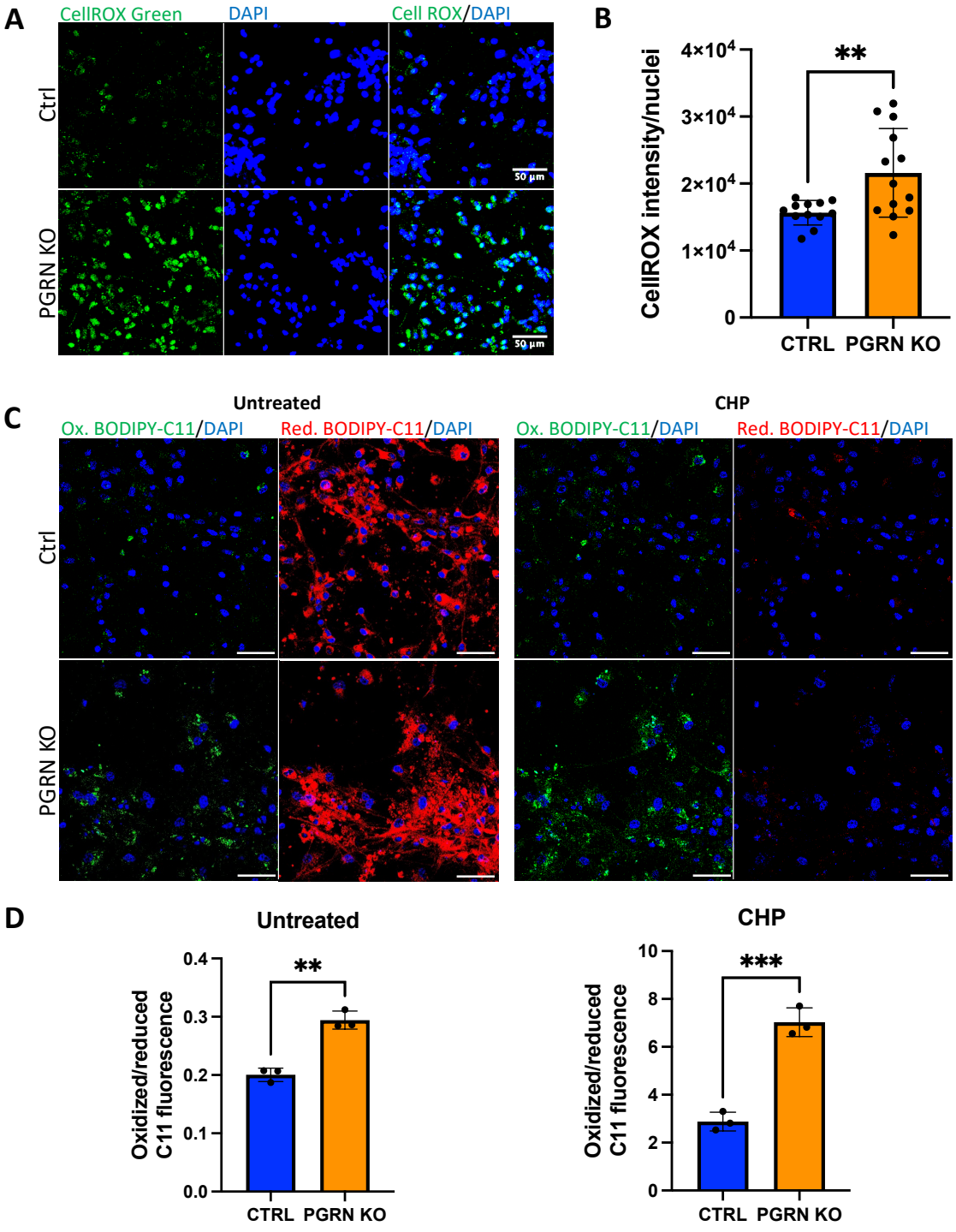

Figure 2.5 - PGRN KO brain organoids show increased cellular ROS and lipid peroxidation

A – Representative images of cellular ROS in PGRN KO and Ctrl dissociated organoids by CellROX Green staining.

B – Quantification of CellROX Green in organoids, calculated as the integrated density of CellROX fluorescence in the field of view normalized by the number of nuclei.

C – Representative images of lipid peroxidation in untreated PGRN KO and Ctrl dissociated organoids by BODIPY 581/591 C11 staining. Ox. BODIPY-C11 (oxidized) represents the levels of lipid ROS, while Red. BODIPY-C11 represents the level of staining with the probe (reduced or unoxidized). Scale bars = 50 μm.

D – Quantification of lipid peroxidation levels in untreated (left) and CHP-treated (right) dissociated organoids, calculated as the ratio of oxidized/reduced BODIPY-C11 mean fluorescence intensity in the ROI of field of view. Each point represents an average of ~65 fields of view.

Statistical significance was calculated by two-tailed unpaired *t*-test. Bars and error bars represent means ± SD. $^{*}p \leq 0.1$, $^{**}p \leq 0.01$, $^{***}p \leq 0.001$, $^{****}p \leq 0.0001$.

PGRN loss sensitizes cells to ferroptosis

The accumulation of lipid peroxides can lead to membrane disruption and ferroptosis, a non-apoptotic type of programmed cell death characterized by iron accumulation and increased lipid peroxidation (145,146). Another hallmark of ferroptosis is impaired activity of glutathione peroxidase 4 (GPX4), an antioxidant enzyme and major inhibitor of ferroptosis that converts toxic lipid hydroperoxides to non-toxic lipid alcohols (146,147) (Figure 2.6 A). Since our results indicate that PGRN loss leads to increased ROS and lipid peroxidation, we next investigated if PGRN deficiency is also linked to sensitivity to ferroptosis. A list of ferroptosis suppressors and driver genes was retrieved from FerrDb (148), a database of ferroptosis regulators, and used to screen for ferroptosis-related DEGs. Differential gene expression analysis showed that in PGRN KO glutamatergic neurons (CN1, CN3, CN2) several ferroptosis-suppressor genes were downregulated (*TXN, FTL, FTH1, TMSB4X, CISD1, CISD2, CHMP5, PARK7, SOX2, BEX1, GPX4*) (Figure 2.6 B). Among these genes, only *FTH1*

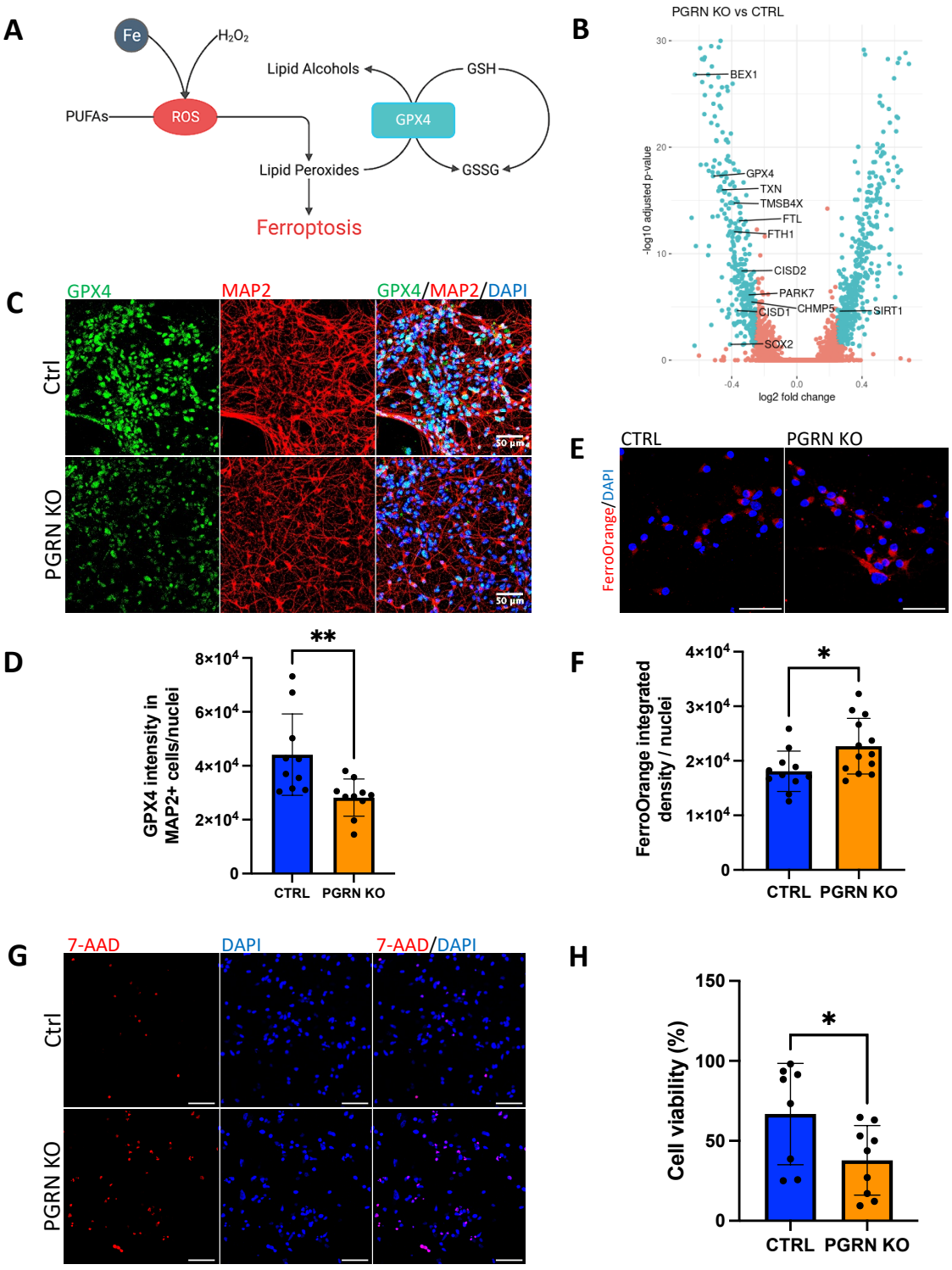

Figure 2.6 - Loss of progranulin sensitizes cells to ferroptosis

A – The production of ROS can cause lipid peroxidation, which in turn induces ferroptosis. Ferrous iron (Fe^{2+}) reacts with hydrogen peroxide (Fenton reaction), which generates ROS that oxidizes polyunsaturated fatty acids (PUFAs) and results in membrane damage and cell death

(ferroptosis). Glutathione peroxidase 4 (GPX4) is the central enzyme regulating ferroptosis. GPX4 converts gluthatione (GSH) into oxidized glutathione (GSSG) and reduces lipid peroxides to non-toxic lipid alcohols. Diagram reprinted from *Rockland Immunochemicals,* 2023, retrieved from rockland.com/resources/the-ferroptosis-pathway.
B - Volcano plot of differential gene expression results of PGRN KO versus Ctrl glutamatergic (CN1, CN2, CN3) neurons, with differentially expressed negative regulators of ferroptosis highlighted. Within the depicted genes, only *FTH1* and *CISD2* are not significantly downregulated in CN2. 925 DEGs (green) were identified using the Wilcoxon test with a log2FC cutoff of (abs)0.25 and p-adjusted value <0.05. Ferroptosis suppressor genes were collected from the ferroptosis database FerrDb v2.
C – Representative images of PGRN KO and Ctrl dissociated organoids labeled with GPX4 and MAP2.
D – Quantification of GPX4 in MAP2-positive cells, calculated as the integrated density of GPX4 fluorescence in MAP2+ cells in the field of view and normalized by the number of nuclei.
E – Representative images of live PGRN KO and Ctrl organoids labeled with FerroOrange and DAPI.
F – Quantification of FerroOrange in organoids, calculated as the integrated density of FerroOrange fluorescence in the field of view normalized by the number of nuclei.
G – Representative images of PGRN KO and Ctrl organoids treated with 100 uM cumene hydroperoxide for 2 hours, and labeled with 7-AAD and DAPI.
H – Cell viability based on of 7-AAD-positive ferroptotic cells after 2 and 3 hours of CHP treatment. The extent of cell death was determined based on counting 7-AAD positive dying cells in randomly chosen regions. Each field of view contains 90 +/- 31.5 cells.
Statistical significance was calculated by two-tailed unpaired *t*-test. Bars and error bars represent means ± SD. $^{*}p \leq 0.1$, $^{**}p \leq 0.01$, $^{***}p \leq 0.001$, $^{****}p \leq 0.0001$. Scale bars = 50 μm.

and *CISD2* were not downregulated in CN2. *BEX1*, that encodes brain-expressed X-linked protein 1, is the most upregulated gene in this gene list, and it has been shown to protect cancer cells from ferroptosis (149). Thioredoxin (*TXN*) inhibits ferroptosis by regulating GPX4 and GSH (150–152), and it promotes ferroptosis in cancer cells when suppressed (150–152). *FTL* and *FTH1* encode the light and heavy chain, respectively, of ferritin, a cytosolic iron storage protein that functions as an iron buffer, and promotes increased Fe^{2+} intracellular levels and ferroptosis when downregulated (153–156). *CISD1* and *CISD2* encode for iron-sulphur cluster containing proteins that regulate mitochondrial iron and ROS metabolism, and knockdown of

CISD1 or *CISD2* induces ferroptosis and mitochondrial iron overload (157–159). In PGRN KO neurons (CN - glutamatergic neurons and IN - GABAergic interneurons), *GPX4,* a master regulator of ferroptosis, was the second most significantly downregulated gene within ferroptosis suppressor genes, and we confirmed its downregulation at the protein level in mature (MAP2+) neurons (Figure 2.6C, 2.6D).

Ferrous iron (Fe^{2+}) accumulation is another hallmark of ferroptosis (145). Iron can induce ferroptosis by activating lipid peroxidation enzymes or by directly generating ROS through the Fenton reaction (160,161). In order to investigate the overall levels of ferrous iron, we used FerroOrange, a fluorescent probe that enables live-cell fluorescent imaging of intracellular Fe^{2+}. We found that PGRN KO organoids have significantly higher ferrous iron content compared to controls (Figure 2.6 E, F). Transcriptomic analysis showed that neurons expressed lower levels of iron transport and uptake genes (Figure 2.3 C). Looking at these results closely, we found that this difference was driven mainly by glutamatergic neurons. Given that glutamatergic neurons showed dysregulation of iron-related and ferroptosis-supressor genes, we also investigated ferrous iron content in neurons by co-labeling live organoid cells with FerroOrange and NeuO, a fluorescent probe that selectively labels neurons. We found that NeuO-positive cells also express higher levels of ferrous iron (Supplementary Figure 2.2 A, B).

To determine if progranulin loss impacts ferroptotic cell death, we induced ferroptosis in organoids by exposing them to CHP. After two and three hours of treatment, cell death in dissociated organoids was assessed with 7-AAD staining. Cumene hydroperoxide induced dramatic overall cell death in both genotypes, but PGRN KO dissociated organoids showed a significant increase in relative cell death when compared to controls (Figure 2.6 G, H).

2.5 Discussion

While it's widely recognized that disease-causing *GRN* mutations decrease PGRN levels, leading to neurodegeneration, the role of PGRN and the sequence of events triggered by its deficiency, culminating in neurodegeneration, remains unknown. In this study, we utilized human forebrain organoids to model complete PGRN deficiency and explore its effects, as 3D organoids offers a more physiologically relevant environment than traditional 2D cultures and allows for a better understanding of complex brain interactions and cell types involved in progranulin loss pathology.

Our study reveals that PGRN loss in human organoids results in pronounced mitochondrial dysfunction. This is evident from the downregulation of ETC genes and the subsequent reduction in oxygen consumption – an accurate measure of mitochondrial function. This data suggest that this decline is likely due to impaired respiratory chain activity resulting from the lower expression of ETC genes. Mitochondrial dysfunction is a common feature in several neurodegenerative diseases, including AD, PD, ALS and the classical mitochondrial disorder Leigh syndrome (162–165). These disorders often exhibit mitochondrial defects such as decreased mitochondrial membrane potential and altered respiratory chain enzyme activities. Reduced activity of respiratory chain complexes and decreased oxygen consumption has also been identified in multiple forms of NCL (166–169). Additionally, previous studies have shown the effect of PGRN loss in mitochondrial function. PGRN deficiency has been linked to decreased mitochondrial respiration and mitochondrial dysfunction in progranulin deficient human neuroblastoma cells and FTD-GRN patients' derived lymphoblasts (131). Moreover, studies have shown downregulation of mitochondrial-related genes and proteins in FTD-GRN neurons (170) and mouse and human models of progranulin deficiency (171,172).

The mitochondria are the primary source of cellular ROS, and defects in OXPHOS can affect several cellular characteristics, including increased ROS generation. The generation of mitochondrial superoxide can arise from inefficient electron transfer within the ETC, mainly complexes I and III, which results in electron buildup and excessive leakage to oxygen, giving rise to the production of ROS (173). Here we demonstrated that PGRN loss results in excessive cellular ROS production, which is likely due to impaired OXPHOS and a deficient antioxidant response. Excessive ROS have been reported in other progranulin-deficient disease models such as human neuroblastoma cells (131), and mouse microglial cells (107), and PGRN has been shown to protect against oxidative stress (87,88). Additionally, oxidative stress is a key contributor to a number of neurodegenerative disorders, including AD, PD, ALS and NCL (174,175). If ROS levels are excessive, they can further impair OXPHOS complexes and cause damage to mitochondrial molecules, further amplifying ROS production (176).

One of the early cellular responses to excessive ROS is to induce mitophagy, and PGRN deficiency has been linked to impaired autophagy and mitophagy (130–133). Accumulation of damaged mitochondria could lead to increased ROS production and subsequent further mitochondrial damage. We found downregulation of several mitophagy-related genes in PGRN KO cells. Given that we found no global changes in mitochondrial mass measured with TOM20, it is possible that these cells engage in compensatory mechanisms by increasing mitochondrial biogenesis, or that impairment of mitophagy due to PGRN deficiency is cell-specific, as previously suggested (132). Additionally, assessment with other mitochondrial markers should be performed to confirm our results on mitochondrial mass.

When ROS surpass the capabilities of antioxidant defense mechanisms, excessive ROS can trigger lipid peroxidation, especially polyunsaturated fatty acids in cell membranes. The

observed elevation in lipid peroxidation in PGRN KO organoids mirrors findings in other neurodegenerative diseases. Oxidative damage to lipids can lead to the formation of lipofuscin, a hallmark of NCL and a phenomenon also observed in PGRN haploinsufficiency (Ward et al., 2017) and other neurodegenerative disorders such as Huntington's disease, AD and PD (143). The observed elevation in lipid peroxidation, together with increased ROS production and dysregulation of a number of antioxidant genes, reinforces the notion that PGRN deficiency exacerbates cellular vulnerability to oxidative stress.

Ferroptosis is a form of non-apoptotic regulated cell death characterized by iron-dependent lipid peroxidation (145). Our findings on increased susceptibility of PGRN KO cells to ferroptotic cell death add another layer of complexity to the role of PGRN in neurodegeneration. Ferroptosis is associated with a diverse array of neurodegenerative disorders, such as AD, PD and ALS (177–179). Additionally, PGRN has been shown to protect mouse brains from ferroptosis induced by cerebral ischemia (180,181) and the neurotoxin MPP^+ (88). We also showed that PGRN KO organoids accumulate ferrous iron. It's been shown that knockdown of ETC genes increases labile iron (182). Mitochondria plays a central role in iron metabolism, as they are the sole site of heme synthesis and the primary generator of iron-sulfur (Fe-S) clusters, and contain up to 20-50% of iron in cells. Heme and Fe-S are essential components of the ETC complexes, and disruptions in these complexes can result in release of ferrous iron (182,183). The observed downregulation of GPX4, a main regulator of ferroptosis, and other ferroptosis-suppressor genes in PGRN KO neurons, particularly in glutamatergic neurons, accentuates the potential significance of PGRN in modulating GPX4-mediated ferroptosis. Additionally, PGRN might play a direct role in ferroptosis. Progranulin is composed of 7 and a half repeats of a highly conserved 12-cysteine granulin motif (34).

Cysteine depletion can induce ferroptosis by causing a direct inhibition of GSH and GPX4 protein expression (184), and disruption of lysosomal cystine efflux attenuates ATF4 induction and triggers ferroptosis (185). It's conceivable that the increased susceptibility to ferroptosis could be attributed to glutamatergic neurons. This speculation arises from our transcriptomic analysis, which revealed that PGRN KO neurons, particularly glutamatergic neurons, could potentially exhibit greater susceptibility to ferroptosis. Moreover, we showed that mature neurons display heightened iron accumulation. Furthermore, ferroptotic damage in neurons is a common feature in several neurodegenerative diseases (186). Further studies are required to establish this relationship definitively.

As summarized in Figure 2.7, the interplay between mitochondrial dysfunction, oxidative stress, and ferroptosis is complex, and these mechanisms most likely collectively contribute to progression of neurodegeneration in the context of PGRN deficiency. Additionally, PGRN plays a major role in the regulation of autophagy and lysosomal function (19,67,130). PGRN loss results in downregulation of ETC genes, either directly or as part of an adaptive response to oxidative stress. This, in turn, can result in mitochondrial dysfunction, leading to an overproduction of reactive oxygen species (ROS) due to an incomplete reduction of oxygen in the ETC. Dysfunctional mitochondria can also disrupt lysosomal function, causing the buildup of damaged cellular components. This dysfunction in lysosomes and autophagy could amplify mitochondrial dysfunction due to accumulation of damaged mitochondria. Defective lysosomal function leads to the accumulation of waste, inducing oxidative stress. Moreover, lipofuscin, found in dysfunctional lysosomes, sequesters iron, contributing to ferroptosis (182). Oxidative stress could further impair both mitochondrial and lysosomal functions. The accumulation of damaged cellular components can overwhelm

lysosomes, and oxidatively damaged mitochondria could intensify ROS production. Oxidative stress is closely associated with ferroptosis, as it can trigger lipid peroxidation, initiating this form of cell death. Additionally, the buildup of iron catalyzes ROS formation, which can result in lipid peroxidation and ferroptosis.

Our findings provide valuable insights into the molecular mechanisms underlying PGRN deficiency. The convergence of mitochondrial dysfunction, oxidative stress and increased vulnerability to ferroptosis highlights the complex interplay of these processes in the pathogenesis of neurodegeneration due to PGRN loss. Although we did not find differences in cell numbers between PGRN KO and control organoids, our results suggest that these features could be early pathomechanisms in neurodegeneration associated with PGRN deficiency. Further investigation into the precise molecular pathways linking PGRN deficiency to these cellular abnormalities could be crucial for developing targeted therapeutic strategies for NCL and FTD caused by GRN loss-of-function mutations.

Limitations of the study

To substantiate our transcriptomics analysis, our data requires supplementary validation with a higher sample size encompassing multiple organoid batches and different iPSC clones. The applicability of these discoveries to human brain pathology requires further investigation, since human brain organoids do not fully recapitulate the complexity of the human brain, such as organization and cell diversity. On that note, incorporating microglia in the organoid model would be valuable, considering their essential role in neurodegeneration due to PGRN loss of mutations. One of the limitations of this study was using dissociated organoids instead of whole organoids in our functional assays, potentially missing key

physiological responses inherent in the intact 3D structure. Additionally, it would be intriguing to explore whether recombinant PGRN can ameliorate the observed effects in PGRN KO organoids.

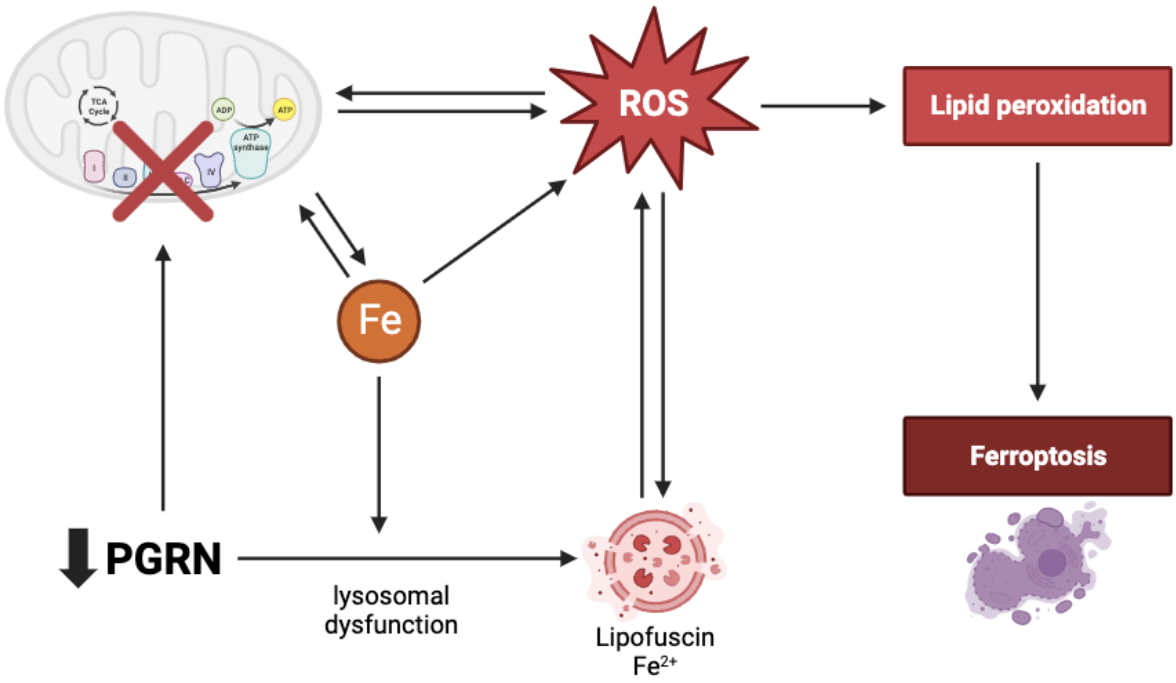

Figure 2.7 – Summary figure describing our findings and possible mechanisms that lead to ferroptosis of PGRN KO cells. Created with BioRender.com.

2.6 Supplementary figures

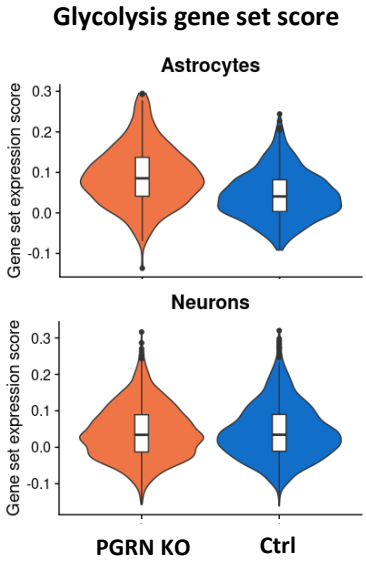

Supplementary Figure 2.1 – Gene expression scores for the glycolysis gene set for astrocytes and neurons.

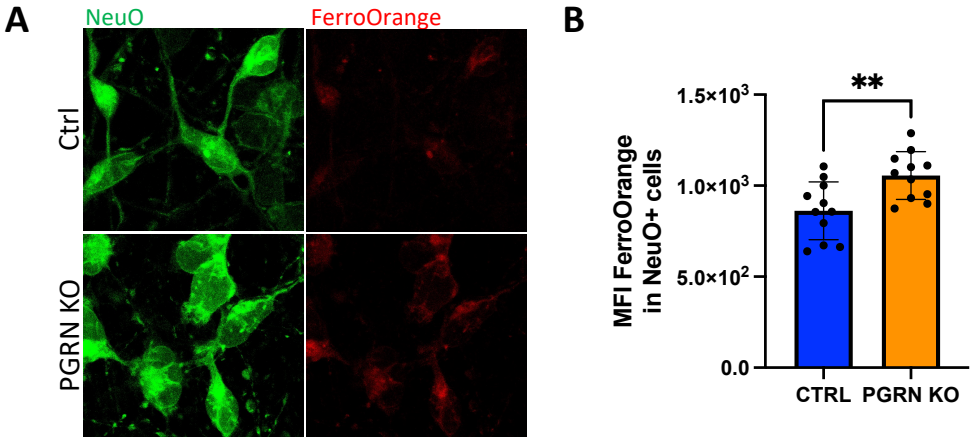

Supplementary Figure 2.2 – PGRN KO neurons accumulate iron
A – Representative images of live PGRN KO and Ctrl organoids labeled with FerroOrange and NeuO.
B - Mean fluorescence intensity (MFI) of FerroOrange in NeuO-positive cells in PGRN KO and Ctrl organoids.
Statistical significance was calculated by two-tailed unpaired *t*-test. Bars and error bars represent means ± SD. $^{*}p \leq 0.1$, $^{**}p \leq 0.01$, $^{***}p \leq 0.001$, $^{****}p \leq 0.0001$.

Chapter 3

Progranulin loss induces lipid metabolism dysfunction in human iPSC-derived microglia

3.1 Abstract

Loss-of-function mutations in the granulin (*GRN*) gene cause frontotemporal dementia in heterozygosity and neuronal ceroid lipofucinosis, a lysosomal storage disease, in homozygosity. While it is well established that disease-causing *GRN* mutations decrease PGRN levels, leading to neurodegeneration, the cellular and molecular mechanisms underlying these conditions remain poorly understood. Progranulin (PGRN) plays a key role in microglial

function, and PGRN loss drives microglia to a disease-activated, hyperinflammatory state. Here, we used human induced pluripotent stem cell (iPSC) derived microglia to model PGRN deficiency. By integrating transcriptomics and lipidomics, we showed that PGRN is involved in lipid metabolism. PGRN deficient (PGRN KO) microglia seemed to accumulate triacyglycerides (TAG) with saturated and monounsaturated long chain fatty acids. Interestingly, when activated with lipopolysaccharide (LPS), PGRN KO microglia showed robust accumulation of TAGs with highly unsaturated and very long chain fatty acids. Transcriptomic analysis revealed that the expression of genes involved in lipid metabolism, including fatty acid synthesis, elongation, desaturation and β-oxidation, was dysregulated in PGRN KO microglia. Moreover, these cells exhibited distinct expression patterns of genes involved in cell proliferation, migration, immune response, inflammation, and energy metabolism. Our findings suggest that lipid accumulation due to progranulin loss might be triggered by transcriptional dysregulation of fatty acid synthesis and β-oxidation pathways, and provide insights into the molecular mechanisms driving neurodegeneration caused by PGRN deficiency.

3.2 Introduction

Neuronal ceroid lipofuscinosis (NCL) and frontotemporal dementia (FTD) are two debilitating neurodegenerative disorders that are caused by mutations in *GRN* in a gene-dose effect. The majority are loss-of function mutations that result in nonsense-mediated mRNA decay (8). Heterozygous *GRN* mutations result in progranulin (PGRN) haploinsufficiency and cause FTD-GRN, which accounts for up to 11.7% of FTD cases (4,5,8). NCL is a group of

lysosomal storage disorders, and the complete absence of PGRN due to *GRN* homozygous mutations leads to neuronal ceroid lipofuscinosis type 11 (CLN11), a rare type of NCL (11,14). Although the clinical manifestations of these diseases are distinct, they share some common pathological features such as lipofuscin accumulation, impaired lysosomal function, neuroinflammation and gliosis (18,19).

Progranulin is a multifunctional intracellular and secreted protein expressed in neurons, microglia, endothelial cells and astrocytes in the central nervous system (CNS) (9,40,78). Microglia are brain resident macrophages that maintain the brain homeostasis and respond to brain injury. In normal and healthy conditions, microglia are in the resting state, when they are constantly surveilling the environment. Microglia become activated in response to endogenous or exogenous pathological insults, when they internalize pathogenic species and try to degrade them, while also activating the expression of inflammatory genes (187,188). Among cells in the CNS, microglia express the greatest amount of PGRN (25,33). PGRN plays a key role in microglial function, by regulating cell recruitment, proliferation and activation (9,99). PGRN deficient mouse microglia are aberrantly activated, produce more proinflammatory cytokines compared to wild-type microglia, induce neuronal loss and promote TDP-43 proteinopathy (24,25,31,189). While these findings underscore the essential role of microglia in neurodegeneration caused by loss of PGRN, the specific contribution of microglia in this context remains unkown.

Microglial lipid metabolism is involved in regulating microglial activation and essential functions, including migration, phagocytosis, and inflammatory signaling, and disruptions in microglial lipid processing are often associated with neurodegeneration (190). PGRN has been shown to trigger changes in the lipidome of human and mouse brains

(69,73,191,192), and to induce lipid accumulation in *GRN*$^{-/-}$ mouse microglia (107,193), but the mechanisms by which PGRN induces lipid metabolism dysfunction are unclear.

In this study, we utilized human iPSC-derived microglia to model PGRN deficiency. By comparing the transcriptomic profiles of *GRN*$^{-/-}$ (PGRN KO) and isogenic control (Ctrl) microglia, we found that PGRN loss leads to dysregulation of expression of genes related to cell proliferation, migration, immune response, inflammation, energy metabolism and lipid metabolism. We also showed that PGRN KO microglia accumulate more lipids in the form of lipid droplets. Lipidomic analysis showed that PGRN deficient microglia seem to accumulate more triacylglycerides (TAG) with saturated and monounsaturated fatty acids (FA). Lipopolysaccharide (LPS) activated PGRN KO microglia showed a distinct profile, with enrichment of TAGs with highly unsaturated and very long chain FA. By integrating lipidomics and transcriptomics data, we showed that the alterations of lipid metabolism resulting from PGRN loss are likely due to transcriptional dysregulation of genes involved in FA synthesis and β-oxidation. These results demonstrate a critical link between PGRN and lipid metabolism, and suggest that lipid abnormalities in microglia might contribute to neurodegeneration caused by *GRN* loss-of-function mutations.

3.3 Methods

Human iPSC lines and culture

PGRN KO (*GRN*$^{-/-}$) and Ctrl (*GRN*$^{+/+}$, isogenic control) human iPSC were both generated in the WTC11 background. Ctrl contains a TdTom under *TMEM119,* and it was generated from WTC11. PGRN KO iPSC was generated by Dr. Bruce R. Conklin (Gladstone

Institute, UCSF) (115) by mutagenizing the WTC11 iPSC by dual Cas9 D10A nickase in the exon 12, which resulted in a 10 base pair deletion in one allele, and a 7 bp insertion plus a 1 bp mutation in the second allele (Figure 3.1 B). To generated iTF-MG, we utilized the human inducible CRISPRi iTF-iPSC, obtained from Dr. Martin Kampmann (UCSF) (194). Human iPSCs were cultured in mTeSR Plus medium (STEMCELL Technologies) in 6-well plates (Corning) coated with Matrigel (Corning). Medium was changed daily, and cells were passed with ReleSR (STEMCELL Technologies) when 70-80% confluent.

Generation of iPSC-derived microglia

Microglia utilized for RNA-seq, lipidomics and lipid droplet accumulation experiments were differentiated from PGRN KO and Ctrl iPSC lines following a published protocol (195). Briefly, human iPSC were allowed to grow until 90-95% confluency. From day 0 (D0) to D3, cells were fed daily with mTeSR plus supplemented with 80 ng/ml BMP4. On D4, medium was replaced with StemPro-34 SFM medium (Gibco) as a base containing the following: 2mM GlutaMax (Gibco), 1x Antibiotic-Antimycotic (Gibco), 25 ng/mL bFGF, 100 ng/mL SCF and 80 ng/mL VEGF. On D6, medium was replaced with StemPro-34 SFM supplemented with 1x Antibiotic-Antimycotic, 50 ng/mL M-CSF, 50 ng/mL SCF, 50 ng/mL IL-3, 5 ng/mL Thrombopoietin and 50 ng/mL Flt3 ligand. On D10, supernatant was collected, cells were pelleted and resuspended in the same medium as D6. Every 4 days, from D14 until ~D25-D45, cells from the supernatant were pelleted then resuspended in StemPro-34 SFM supplemented with 1x Antibiotic-Antimycotic, 50 ng/mL M-CSF, 50 ng/mL Flt3l and 25 ng/mL GM-CSF, and returned to the same parental well. Starting from ~D25-D45, microglial progenitors floating in the medium were collected, pelleted and resuspended in microglia differentiation

medium containing RPMI-1640 (Gibco), plus 2mM GlutaMAX, 1x Antibiotic-Antimycotic, 10 ng/ml GM-CSF and 100 ng/ml IL-34. Microglial progenitors were plated into a new 6-well plate, and microglia was matured in the same media for 14 days, with full media change every 4 days. The parental wells were fed every 4 days with the media composed of StemPro-34 SFM supplemented with M-CSF, Flt ligand and GM-CSF. For immunocytochemistry and BODIPY staining, mature microglia were lifted with Accutase (STEMCELL Technologies) and replated in glass-bottom 8-well chambers (IBIDI) at approximately 100k cells/well a few days before the experiments. Cells were assayed at D14-D21. All cytokines were purchased from Peprotech.

Generation of iTF-MG

For OPTIR experiments, we utilized induced-transcription factor microglia-like cells (iTF-MG) derived from the inducible CRISPRi iTF-iPSC line, that were generated following a established protocol (194). Briefly, iTF-iPSC were allowed to grow until 90-95% confluency. On day (D0), iPSC colonies were dissociated as single cells with Accutase and replated on matrigel-coated 6-well plates in mTeSR Plus medium plus 10nM ROCK inhibitor, and 2ug/mL doxycycline (Sigma). On D2, medium was replaced with Advanced DMEM/F12 Medium (Gibco) as a base, plus 1x GlutaMax, 1x Antibiotic-Antimycotic, 2ug/mL doxycycline, 10 ng/ml GM-CSF, 100 ng/ml IL-34, and 50 nM TMP (MP Biomedical) to induce CRISPRi activity. On D4, cells were fed with the same medium as D2, and supplemented with 50 ng/ml M-CSF and 50 ng/ml TGFB1 (Peprotech). Medium was changed every 2 days, and iTF-MG were assayed at D10.

Knockdown of *GRN* in iTF-MG

To knockdown *GRN*, a sgRNA targeting *GRN* was lentivirally packaged in HEK293T cells, and transduced into CRISPRi iTF-iPSCs. The control iPSC were transduced with a scrambled sgRNA. Cells were selected with 2 µg/ml puromycin. To quantify *GRN* knockdown, total RNA was extracted from iPSC using PureLink RNA Mini Kit (ThermoFisher), and cDNA synthesized with the ProtoScript II First Strand cDNA Synthesis Kit (NEB). qPCR was performed on an Applied Biosystems QuantStudio 6 Pro Real-Time PCR System, using TaqMan probes (ThermoFisher) specific for *GRN* (Hs00963707_g1) and for *PPIA* (endogenous reference, Hs99999904_m1). Expression fold change was calculated using the ΔΔCt method.

RNA-sequencing (RNA-seq)

Sample processing and library preparation

For RNA-seq, we utilized 3 samples from 3 separate batches of iPSC-derived microglia of each genotype - PGRN KO and Ctrl. RNA was extracted using the PureLink RNA Mini Kit (ThermoFisher). Isolation of mRNA was done using NEBNext Poly(A) mRNA Magnetic Isolation Module (NEB, E7490S), and library prep using NEBNext Ultra II Directional RNA library prep kit (NEB, E7760S). Libraries were sequenced on Illumina NovaSeq 6000, at the UC Davis DNA Technology Core.

Counts matrix generation, quality control and RNA-seq differential expression analysis

Quality control for fastq files was performed with Rfastp 3.18. The quasi-mapping alignment tool Salmon v1.2.1 was used to map the filtered reads to the GRCh38 genome and to obtain the read counts for downstream analysis. Quality check was performed using

MultiQC 1.17. All subsequent analysis were performed on RStudio 4.3.1. Differential gene expression analysis was performed with the package DESeq2 1.40.0 (196). Identification of differentially expressed genes (DEG) was done using the Wald test, and based on log2FC values and FDR-corrected p-value of ≤ 0.05. Enrichment analysis for gene ontology (GO) terms and pathways among DEGs was performed using EnrichR (123), Metascape (127) and GSEA (197).

BODIPY 493/503 staining

iPSC-derived microglia were treated for 18 hours with 5 μg/ml LPS (lipopolysaccharide from E. coli, Sigma) in microglia differentiation medium to induce lipid droplet formation. Untreated and LPS-treated cells were fixed with 4% PFA for 10 min at room temperature (RT), then washed 3x with PBS. Fixed cells were incubated with BODIPY 493/503 (ThermoFisher) (1:1000 in PBS from 1 mg/ml stock solution in DMSO) for lipid droplet staining for 15 min at RT. Samples were washed three times with PBTA, then mounted with Prolong Diamond Antifade Mountant (Invitrogen) with DAPI for nuclei staining.

Immunocytochemistry

Cells were fixed with 4% PFA for 10 min at room temperature (RT), then washed 3x with PBS. For immunocytochemistry, fixed cells were incubated in blocking buffer containing PBTA (0.5% BSA and 0.1% Triton X-100 in PBS) plus 5% normal donkey serum for 1h at room temperature. Samples were then incubated with primary antibodies in blocking buffer overnight at 4ºC, washed three times with PBTA, then incubated with secondary antibody in blocking buffer for 1h at room temperature. Samples were washed three times with PBTA,

then mounted with Prolong Diamond Antifade Mountant (Invitrogen) with DAPI for nuclei staining. Antibodies used were 1:1000 rabbit anti-IBA1 (Wako, 019-19741), rabbit anti-PGRN (Atlas HPA008763, 1:125), 1:1000 donkey anti-rabbit Alexa Fluor 488 (Invitrogen, A-21206).

Image acquisition and analysis

Samples were imaged using a Leica SP8 confocal microscope, and image analysis was done in ImageJ2 (Fiji) software v2.14.0. For lipid droplet analysis, CTCF was calculated with the formula: CTCF = integrated density – (area of selected region of interest X mean fluorescence of background readings). Integrated density (IntDen) was calculated for the region of interest (ROI) in the field of view. Size and number of lipid droplets were calculated using the analyze particles function on Fiji.

OPTIR measurements

Sample processing

10-mm diameter CaF2 slides were placed in each well of the 24-well plate and were soaked in 70% ethanol for 15 minutes, then rinsed with MiliQ water twice. iTF-MG were plated at 25,000 cells per well the day before treatment. 100 uM of Azide palmitic acid and palmitic acid were added directly to the media, and the slides with treated cells were collected after 24 hours. The slides were rinsed with cold PBS once, incubated in 4% PFA at room temperature for 10 minutes, and then rinsed again with cold PBS twice. The cells on CaF 2 slides were stored in PBS at 4ºC until OPTIR measurements were taken.

Fluorescence integrated OPTIR setup

OPTIR imaging was performed on mIRage LS (Photothermal Spectroscopy Corp.). The system consists of a mid-IR pump beam and a visible probe beam. The mid-IR beam was a pulsed quantum cascade laser running at 100 kHz repetition rate and 1 to 10% duty cycle. The visible probe was a continuous wave laser with a center wavelength of 532 nm. Two geometries were used for the measurement: counter-propagation and co-propagation of the IR and visible beam. For counter-propagation, the mid-IR beam was focused below the sample substrate (CaF_2) with a reflective objective (40x, 0.78NA, Pike Technologies), and the visible beam was focused from above the sample substrate with a refractive objective (50x, 0.8NA, Olympus). For co-propagation, both the mid-IR and visible beam was focused with the reflective objective. Epi-detected light was collected and focused on a photodiode. The OPTIR signal was demodulated with a lock-in amplifier and the image was created by raster scanning with an XY motorized stage. The system was enclosed and purged under gentle nitrogen flow to minimize water vapor interference of spectra. For widefield fluorescence imaging, filter cube sets covering common fluorophore and fluorescence proteins in blue, green, red, and far-red channels were used. A camera with a high quantum yield was used to capture the fluorescence images.

OPTIR spectral acquisition, spetra and image analysis

Data presented were acquired with 0.5 μm pixel size. The recipe used for OPTIR spectral measurement was 200 cm^{-1}/s scan speed. The spectral scan range was 980 to 2300 cm^{-1}. The IR power at the sample was 6 mW for counter-propagation measurement. IR power was measured at 2096 cm^{-1}. OPTIR spectra were normalized with the IR laser power spectrum. For the spectra shown in the figures, raw spectra were normalized to total protein content at 1654 cm^{-1}. For spectral-based quantifications, whole spectral fitting was used with the peaks found

using smoothed second derivatives. The calculation of the ratio between newly synthesized lipids, total lipids, and protein was done using the area under the curve from the fitted results. OPTIR images were normalized to the IR power intensity at the corresponding wavenumber.

Lipidomics

Sample Processing

iPSC-derived microglia were treated for 18 hours with 5 μg/ml LPS (Lipopolysaccharide from E. coli, Sigma) in microglia differentiation medium. Treated and untreated cells were lifted with Accutase, counted, pelleted in PBS, and cell pellets were stored at -80ºC until the assay. Lipids from cell pellets were extracted using the Bligh Dyer method. The lower organic phase was taken and used for lipidomics analysis. Five microliters of internal standards (EquiSPLASH Lipidomix, Avanti Polar Lipids, 330731) was added to each sample prior to extraction.

HPLC-MS/MS method

HPLC-MS/MS was performed using a 1260 Infinity UHPLC System (Agilent) coupled to a Qtrap 6500 mass spectrometer (SCIEX). Samples were separated by HILIC on an X-Bridge amide column (Waters). Mobile phases included: A) 95% acetonitrile, 5% water with 10 mM ammonium acetate, B) 50% acetonitrile, 50% water with 10 mM ammonium acetate. HPLC and MS parameters followed the SCIEX Lipidyzer protocol, targeting 1200 lipid molecular species.

Data Analysis

HPLC peaks were integrated using MultiQuant software (SCIEX). Sums, averages, and standard deviations were calculated using custom R scripts. Peak areas were normalized

to the peak area of the corresponding internal standard and the provided cell number counts to account for any sample to sample variations during sample extraction or HPLC-MS/MS analysis. Statistical analyses, including PL-SDA, heatmaps, and volcano plots, were done using Metaboanalyst (198).

3.4 Results

Transcriptomic analysis of Ctrl and PGRN KO iPSC-derived microglia

We initiated our research by investigating the global transcriptome changes resulting from PGRN deficiency in human microglia (Figure 3.1 A). Microglia were generated from two human iPSC lines – PGRN KO ($GRN^{-/-}$), and an isogenic control – Ctrl ($GRN^{+/+}$). Both iPSC lines were in the WTC11 iPSC background, which was mutagenized to generate the PGRN KO iPSC (115) (Figure 3.1 B). PGRN KO and Ctrl microglia were generated following a protocol that uses cell adhesion as a selection factor (195) (Figure 3.1 C). Microglia exhibit the expected morphology and expressed the canonical marker Iba-1 (Figure 3.1 D). Knockout of *GRN* was confirmed on protein expression levels (Figure 3.1 D), and on mRNA levels through RNA-sequencing (RNA-seq) analysis, as *GRN* was the most significantly downregulated gene between PGRN KO and Ctrl cells.

We performed RNA-seq analysis in PGRN KO and Ctrl iPSC-derived microglia from 3 separate differentiations. Samples from biological replicates (PGRN KO and Ctrl) showed separation in principal component analysis (PCA) (Figure 3.2.1 A). After removing lowly expressed genes, we performed differential gene expression analysis. By comparing PGRN KO and Ctrl microglia, we identified 1,318 upregulated and 508 downregulated genes

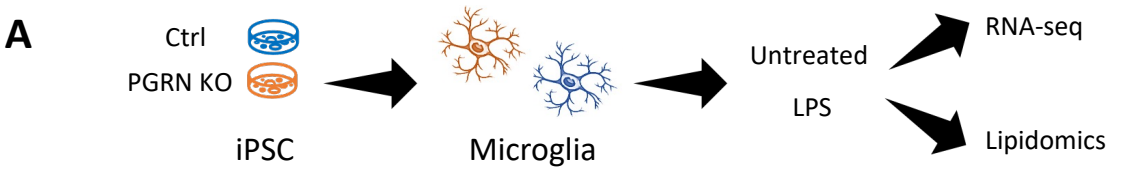
A
Ctrl
PGRN KO
iPSC
Microglia
Untreated
LPS
RNA-seq
Lipidomics

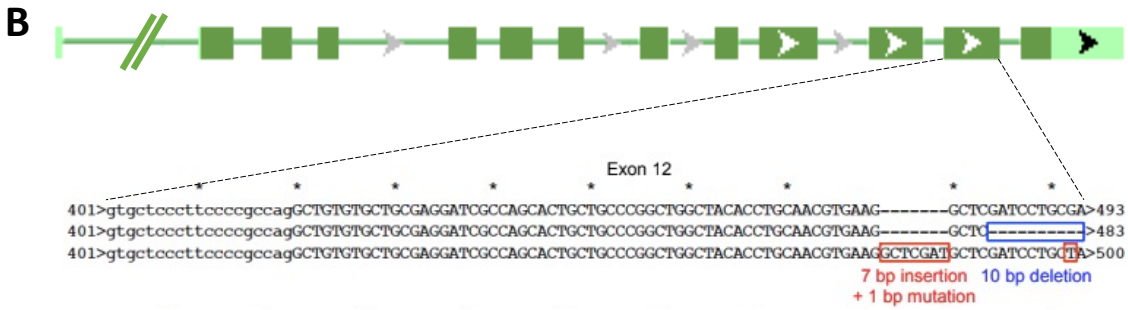
B
Exon 12
401>gtgctcccttccccgccagGCTGTGTGCTGCGAGGATCGCCAGCACTGCTGCCCGGCTGGCTACACCTGCAACGTGAAG-------GCTCGATCCTGCGA>493
401>gtgctcccttccccgccagGCTGTGTGCTGCGAGGATCGCCAGCACTGCTGCCCGGCTGGCTACACCTGCAACGTGAAG-------GCTC---------->483
401>gtgctcccttccccgccagGCTGTGTGCTGCGAGGATCGCCAGCACTGCTGCCCGGCTGGCTACACCTGCAACGTGAAGGCTCGATGCTCGATCCTGCTA>500
7 bp insertion
10 bp deletion
+ 1 bp mutation

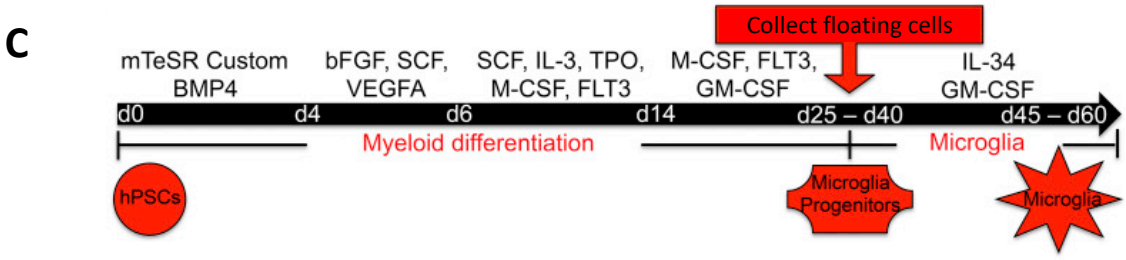
C
Collect floating cells
mTeSR Custom
BMP4
bFGF, SCF,
VEGFA
SCF, IL-3, TPO,
M-CSF, FLT3
M-CSF, FLT3,
GM-CSF
IL-34
GM-CSF
d0
d4
d6
d14
d25 – d40
d45 – d60
Myeloid differentiation
Microglia
hPSCs
Microglia
Progenitors
Microglia

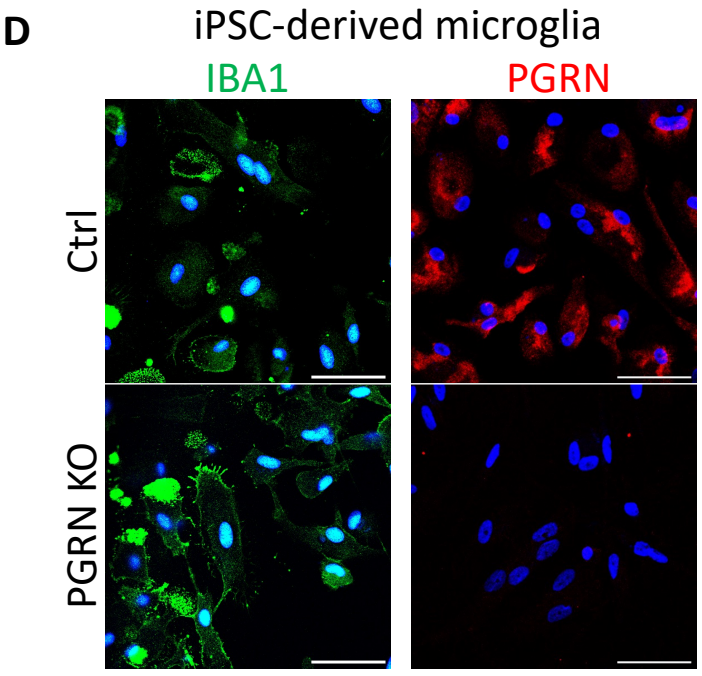
D
iPSC-derived microglia
IBA1
PGRN
Ctrl
PGRN KO

Figure 3.1 – Summary of experiment and characterization of iPSC-derived microglia
A – Summary of the experiment.
B – Diagram of the *GRN* gene, which contains 13 exons. The *GRN* region that was modified is depicted. The modification was generated by dual Cas9 D10A nickase in the exon 12, and resulted in a 10 base pair deletion in one allele, and a 7 bp insertion plus a 1 bp mutation in the second allele.
C – Diagram depicting the major steps of the microglial differentiation protocol. Diagram modified from Douvaras et al., 2017 (195).
D – Immunofluorescence representative images showing expression levels of PGRN and IBA1 in Ctrl and PGRN KO microglia (scale bars = 50 μm).

(absolute log2FC > 0.5, adjusted p-value < 0.05) (Figure 3.2.1 B). We then conducted gene set enrichment analysis to identify biological processes and pathways that were overrepresented among the differentially expressed genes (DEG) (Figure 3.2.1 C). Among the upregulated genes, we found a robust enrichment in cell-cycle related genes. Out of the 15 first enriched pathways of upregulated genes, 3 were related to cell cycle (G2M checkpoint, mitotic spindle and E2F targets) (Figure 3.2.1 C – Hallmark pathways). By visualizing all the upregulated and downregulated genes related to mitotic cell-cycle, we confirmed that the majority were indeed upregulated (Figure 3.2.1 D). This robust upregulation in cell-cycle genes has been reported in *GRN*$^{-/-}$ mouse microglia in a previous study (199), and it is consistent with findings that progranulin deficiency leads to microgliosis in the mouse and human brain (30–33,75,99).

Pathway enrichment analysis of upregulated genes in PGRN KO microglia also identified pathways related to the extracellular matrix (ECM) and cell adhesion, such as focal adhesion, extracellular matrix-receptor interaction, cell-adhesion molecules and Rap1 signaling pathway (Figure 3.2.1 C – KEGG pathways). Most genes related to epithelial-mesenchymal transition (EMT) were included in the ECM and cell adhesion terms. PGRN KO microglia showed upregulation of genes encoding ECM components such as collagens,

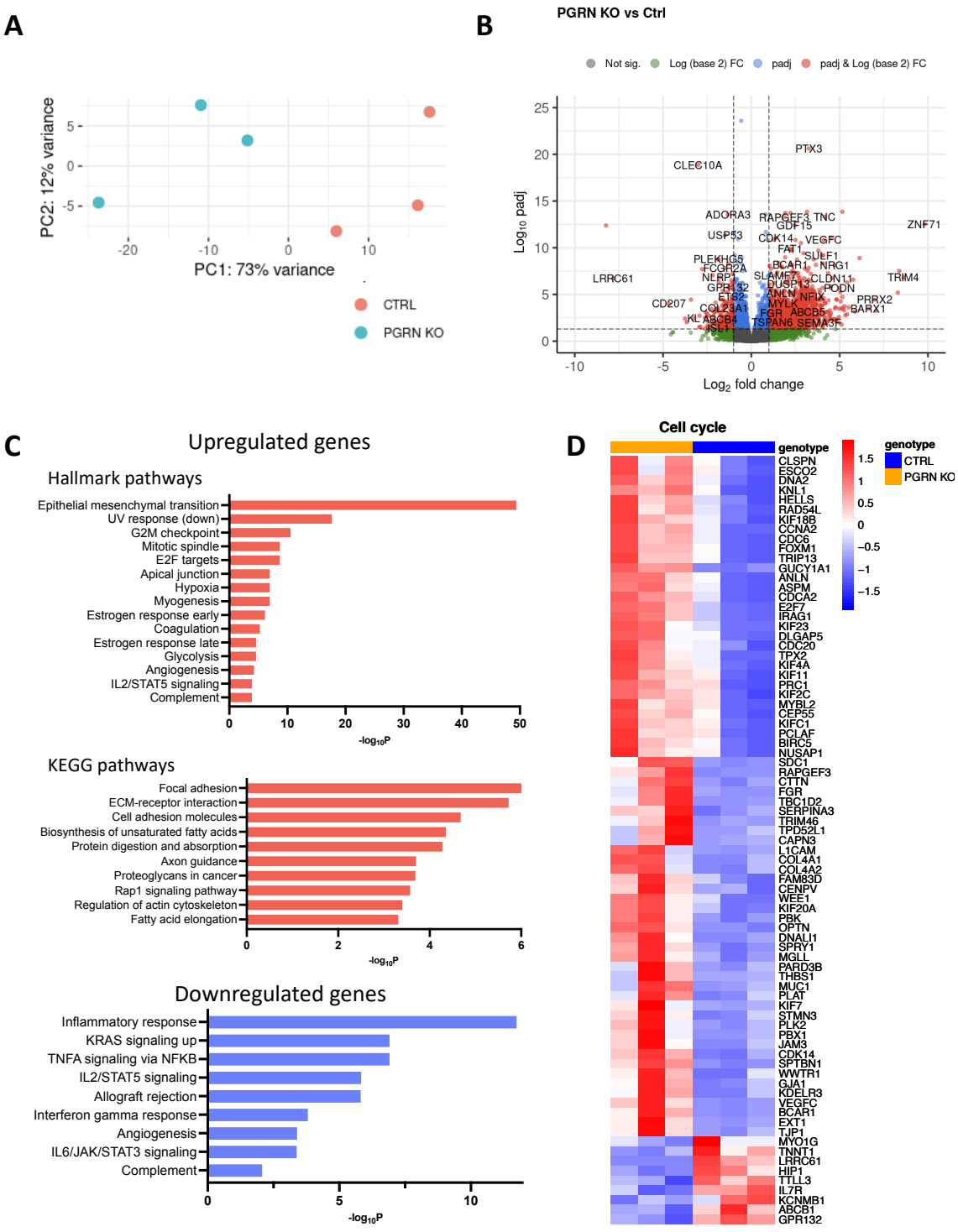

Figure 3.2.1 – RNA-seq analysis of PGRN KO and Ctrl microglia – part 1
A – Principal component analysis (PCA) plot of PGRN KO and Ctrl microglia samples.
B – Volcano plot of differential gene expression results of PGRN KO versus Ctrl microglia. 1,318 upregulated and 508 downregulated genes (red) were identified using the Wald test with

a log2FC cutoff of (abs)0.5 and p-adjusted value <0.05. *GRN* was the most downregulated gene and was excluded from the graph.
C – Bar graphs of Hallmark and KEGG enriched pathways across differentially expressed genes (DEG) between PGRN KO and Ctrl microglia. The first 500 upregulated genes (ordered by adjusted p-value) were used for the analysis due to the requirements of the software. Enrichment analysis of DEG was performed in GSEA.
D – Heatmap of expression levels of cell cycle related DEGs.

proteoglycans (syndecan, perlecan), and glycoproteins (tenascin, thrombospondin, laminin, periostin), and ECM-related genes such as matrix-degrading enzymes metalloproteinases (MMP), lysysl oxidase-like proteins (LOXL), and matrix metalloproteases (ADAMTS). ECM components can affect microglial activation, migration and proliferation (200). In fact, a top enriched pathway of upregulated genes in GO biological processes (not shown) was positive regulation of cell motility, including *MYLK*, *TJP1*, *CAV1*, *TWIST2*, *FGR* and *CCNA2*. Additionally, the focal adhesion enriched term in our data set included genes (*PDGFRA*, *PDGFRB*, *PDGFD*, *CAV1*, *TNC*, *VEGFC*, *PGF*, *MYLK*, *FLNC*, *MET*, *BCAR1*) that are related to cell motility. These results indicate that PGRN loss induces remodeling of the extracellular matrix and stimulates microglial cell migration.

Glycolysis was another enriched term of upregulated genes in PGRN KO microglia (Figure 3.2.1 C – Hallmark pathways), including genes such as *ALDH2, ALDH7A1, PGM1, CDK1, GPC1, GPC3, GPC4, EXT1, NT5E, VCAN, COL5A1, DEPDC1, SDC1, AK4, KDELR3, KIF20A, MET*. The upregulation of glycolysis genes suggests that loss of PGRN leads to dysregulation of energy metabolism in human microglia.

Lysosomal-related genes were also found to be upregulated. These included *TMEM25, GALNS, GM2A, TASL* and the lysosomal protease cathepsins *CTSZ* and *CTSV*. CTSZ has been shown to be upregulated in PGRN deficient human brains (171) and human-iPSC-derived

neurons (201). TMEM25 and TASL are involved in regulating lysosomal acidification (202,203). GM2A participates in the degradation of the glycosphingolipid ganglioside, which is increased in progranulin-deficient human and mouse brains (191).

Pathway enrichment analysis of downregulated genes showed that the most significant term was inflammatory response (Figure 3.2.1 C), which was also an enriched term among the upregulate genes. Since PGRN plays a critical role in the regulation of the immune and inflammatory responses (9,25,33,204), we looked at Reactome-defined immune system and Hallmark-defined inflammatory response DEGs (Figure 3.2.2 A). The heatmaps provided evidence that there is a combination of up and downregulated genes. Indeed, several pathways involved in the immune response were overrepresented among downregulated genes (TNF-α signaling via NF-kB, IL-2/STAT5, IFN-γ response, IL6/JAK/STAT3 signaling, complement) and upregulated genes (IL-2/STAT5, mTORC1, TNF-α signaling via NF-kB and TGF-β signaling pathways) (Figure 3.2.1 C). These results indicate that progranulin loss causes a change instead of a disturbance in the immune and inflammatory responses, as shown previously in PGRN deficient mouse microglia (199).

We also found genes involved in phagocytosis (*ALOX15, PLD4, P2RY6, CEACAM4, IL1B, TLR2, BIN2, PECAM1, AIF1, RARA, CD302*) to be downregulated, which suggests phagocytosis is impaired in our microglial model of PGRN deficiency. In line with these findings, several studies have shown that PGRN deficient microglia show deficits in phagocytosis (100,106,107).

A robust dysregulation of lipid metabolism genes was found in PGRN KO microglia. Among PGRN KO upregulated genes, two of top enriched terms were biosynthesis of unsaturated fatty acids (FA) and fatty acid elongation (Figure 3.2.1 C – KEGG pathways),

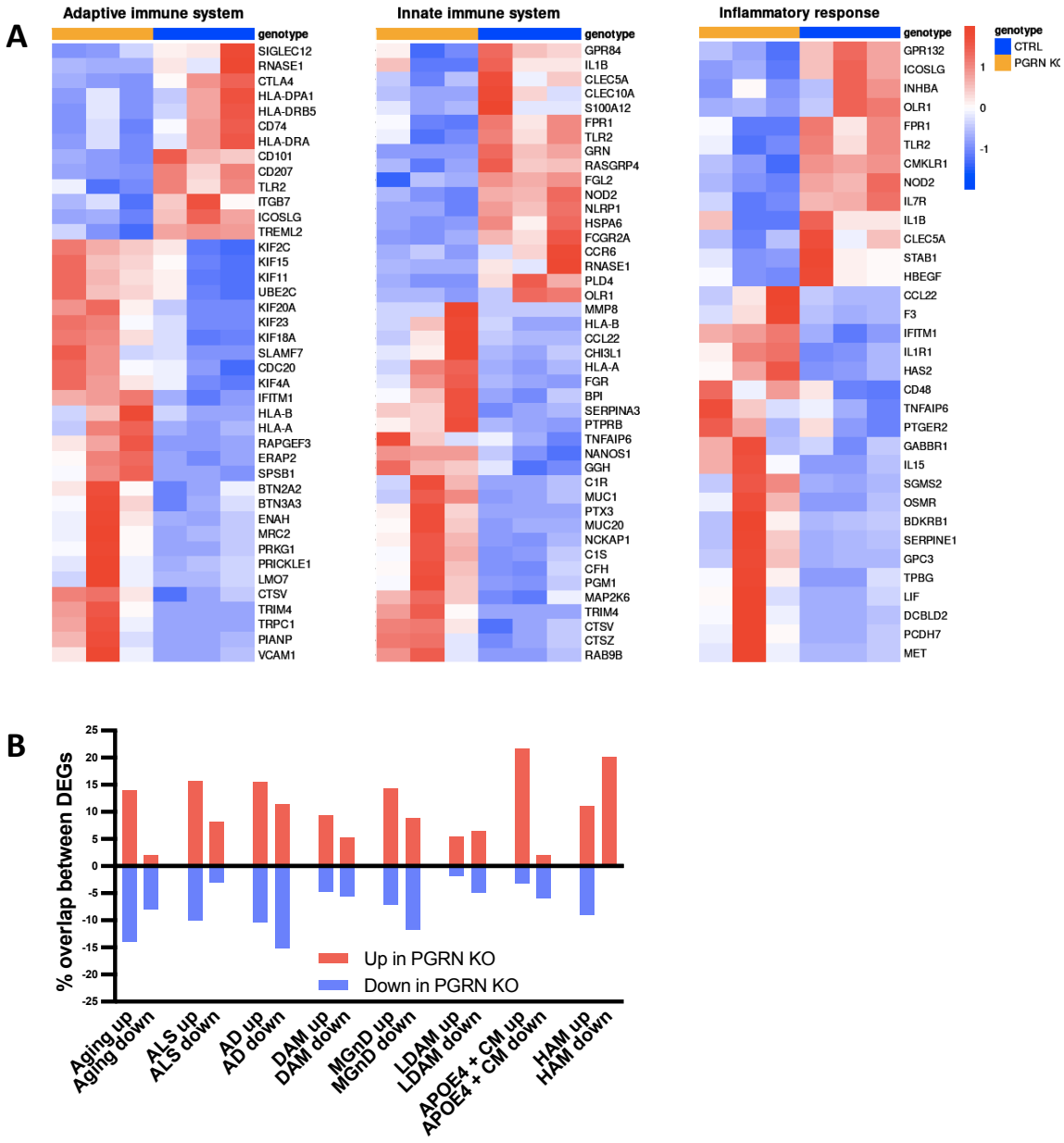

Figure 3.2.2 – RNA-seq analysis of PGRN KO and Ctrl microglia – part 2

A – Heatmaps of expression levels of DEG involved in adaptive immune system, innate immune system (Reactome) and inflammatory response (Hallmark) in PGRN KO and Ctrl microglia.

B – Overlap between genes changing in microglia in aging and neurodegeneration (aging), amypotrophic lateral sclerosis (ALS), Alzheimer's disease (AD), disease-associated microglia (DAM), neurodegenerative microglia (MGnD), lipid-droplet accumulating microglia (LDAM), APOE4, and human AD microglia (HAM), and genes upregulated (red) or downregulated (blue) in PGRN KO microglia. The percentage overlap denotes the fraction of genes in each gene list that are upregulated or downregulated in PGRN KO microglia.

which included the genes *ELOVL2, ELOVL4, ELOVL5, ELOVL6, ELOVL7, SCD, SCD5, ACOT2* and *ACOT1*. Elongation of very long–chain fatty acid (ELOVL) 1-7 family enzymes catalyze elongation of FAs beyond 12 carbons (205). ELOVL2 is responsible for elongation of C20–C22 polyunsaturated FAs (PUFA), ELOVL4 elongates extremely long saturated FAs and PUFAs > C26, ELOVL5 elongates C18–C20 PUFAs, ELOVL6 is responsible for elongation of saturated fatty acids (SFA) and monounsaturated fatty acids (MUFA) C16 or shorter, and finally ELOVL7 catalyzes elongation of saturated and unsaturated C16–C22 FAs (206). Stearoyl-CoA desaturase (SCD) are enzymes required for MUFA biosynthesis from SFA. MUFAs produced by SCD serve as substrates for the synthesis of various lipid categories, including phospholipids, triacylglycerides (TAG), and cholesteryl esters (CE) (207). Finally, acyl-CoA thioesterases (ACOT) control the balance between activated fatty acyl-CoAs and free FAs, by cleaving fatty acyl-CoAs into free FAs and CoA. The generation of Acyl-CoAs is a necessary step for FAs to undergo oxidation or be incorporated into complex lipids (208). Moreover, Acetyl-CoA carboxylase (ACC1, encoded by *ACACA*) was also upregulated. ACC1 is the first and rate-limiting enzyme of de novo fatty acid synthesis that catalyzes the carboxylation of acetyl-CoA to produce malonyl-CoA, the building block used for the biosynthesis of FAs (209). We also found upregulation of lipid sensing nuclear receptors *NR1H3* (that codes for LXRα) and *PPARG*. LXRα is a master regulator of lipid metabolism that regulates FA synthesis by controlling activation, elongation, and desaturation of FAs. In fact, it regulates all enzymes involved in synthesis of saturated or monounsaturated FAs (210,211). PPARγ regulates FA synthesis, storage and uptake (212). Genes involved in glycerophospholipid biosynthesis (*ACHE, PLA2G2D, ETNK2, GPD1, PLAAT4, OSBPL10*), TAG metabolism (*MGLL, ANGPTL4, GNB3, CAV1, APOC1*), and sphingolipid biosynthesis

(*ARSJ, ARSI, SGMS2, PRKD1, PLPP3, SGPP2)* were also upregulated. Among lipid related genes, we found downregulation of genes related to mitochondrial and peroxisomal β-oxidation of FAs, including *ALOX15, PIPOX, DLG4, ACADVL, ABCB1* and *ABCB4*. Among these, very long-chain acyl-coenzyme A dehydrogenase (VLCAD, encoded by *ACADVL*) is essential for FA catabolism, as it catalyzes the initial step of mitochondrial β-oxidation of long-chain (C14-C20) FAs (213). Our results support previous studies that showed upregulation of genes involved in lipid biosynthesis in FTD-GRN brains (214), and that suggest progranulin is involved in regulating lipid metabolism (73,107,215).

Next, we investigated the expression of homeostatic microglial genes, as diseased microglia show loss of homeostatic functions in mouse models of amyotrophic lateral sclerosis (ALS), Alzheimer's disease (AD), and multiple sclerosis (MS) (216). Within the 68 homeostatic genes, only 8 were downregulated (*CMKLR1*, *PALD1*, *IL10RA*, *CSF1R*, *MEF2A*, *SLC02B1*, *PMEPA1*, *SCAMP5*), and 5 upregulated (*GOLM1*, *TMEM119*, *BASP1*, *ITGA6*, *USP2*) in PGRN KO microglia. We also compared the transcriptomic profile of PGRN KO microglia with the profiles of murine microglia in aging (217), ALS murine model (218), AD murine model (219), disease-associated microglia (DAM) (220), MGnD (neurodegenerative microglia associated with ALS, MS and AD murine models) (216), lipid-accumulating microglia (LDAM) (107), human AD microglia (HAM) (221), and APOE4 iPSC-derived microglia (222). In general, we found poor convergence of transcriptional signatures between our dataset and the investigated datasets (Figure 3.2.2 B). The highest overlap was found between upregulated genes in our PGRN KO microglia model and APOE4 iPSC-derived microglia compared to APOE3 microglia (222). Interestingly, this study showed that human

APOE4 microglia exhibits lipid accumulation and exacerbated immune and inflammatory responses.

These results indicate that loss of PGRN induces transcriptional changes in genes involved in essential microglial functions, such as regulation of immune and inflammatory responses, microglia proliferation and migration, energy metabolism, phagocytosis, and lipid metabolism. These functions are often altered in neurodegenerative microglia (107,222,223). However, progranulin deficiency causes microglia to have a unique transcriptome signature that is different than previously described microglial states in neurodegeneration.

Transcriptomic analysis of LPS-treated Ctrl and PGRN KO iPSC-derived microglia

The proinflammatory bacterial endotoxin lipopolysaccharide (LPS) is a commonly used inducer of inflammation and activation in microglia (224). It has been shown that upon LPS treatment, *GRN*$^{-/-}$ murine microglia become hyperactivated (25), produce more complement proteins (33), and accumulate neutral lipids (107). Moreover, *GRN*$^{-/-}$ macrophages produce higher amounts of pro-inflammatory cytokines (TNFα and IL-6) when stimulated with LPS (24). To investigate the transcriptomic changes induced by PGRN deficiency in microglia stimulated with LPS, we treated iPSC-derived PGRN KO and Ctrl microglia with 5 ug/ml LPS for 18h, and performed RNA-seq analysis (Figure 3.1 A). Samples from biological replicates (PGRN KO-UNT, Ctrl-UNT, PGRN KO-LPS and Ctrl-LPS) clustered together in principal component analysis (PCA) (Figure 3.3 A). Untreated and LPS-treated samples clustered tightly along PC1, which accounted for 72% of the transcriptional variation observed across the datasets and illustrated the strong effect of LPS on the microglia transcriptome.

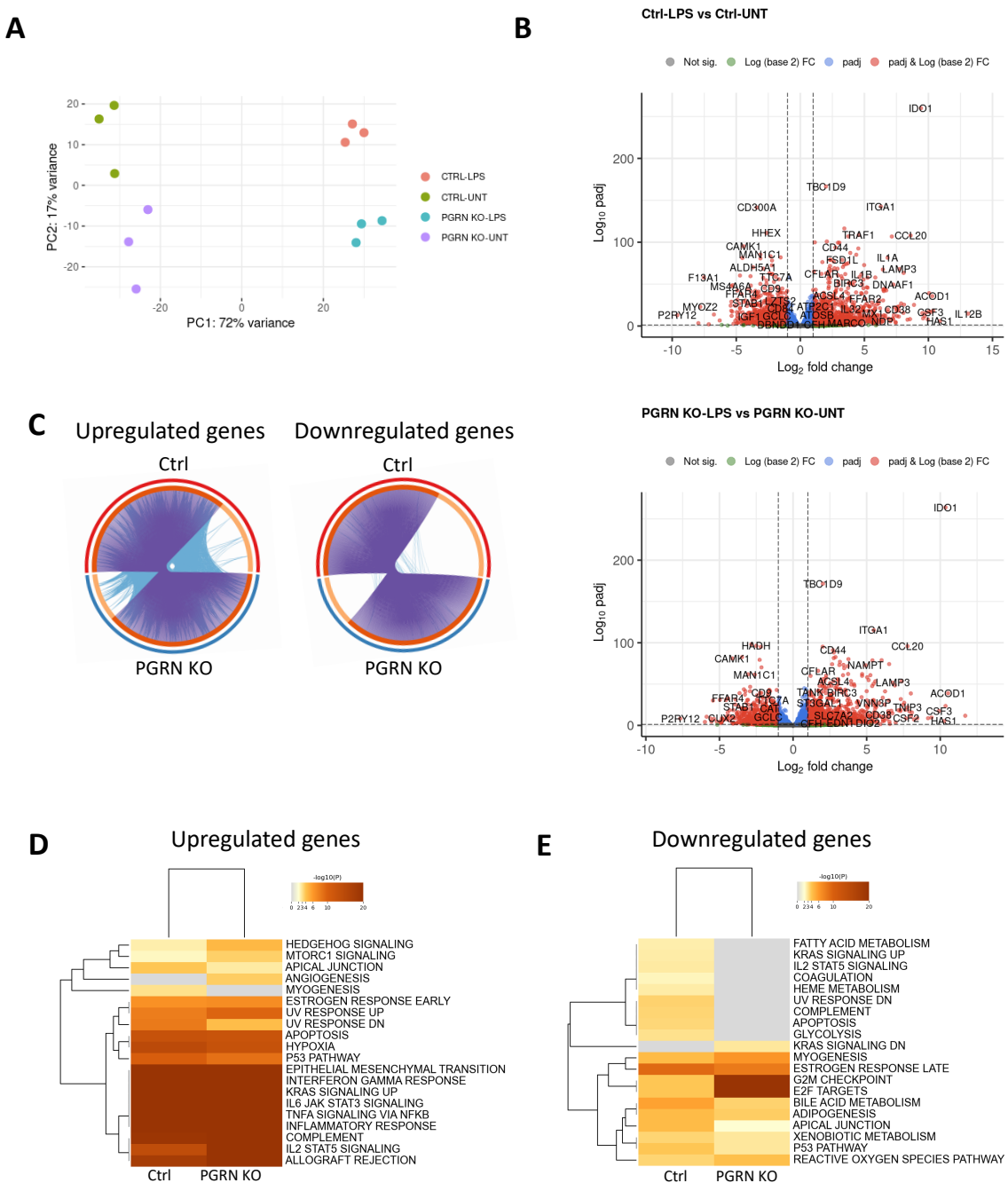

Figure 3.3 – RNA-seq analysis of LPS-treated PGRN KO and Ctrl microglia

A – Principal component analysis (PCA) plot of untreated and LPS-treated PGRN KO and Ctrl microglia samples.

B – Volcano plots of differential gene expression results of Ctrl-LPS vs Ctrl-UNT and PGRN KO-LPS vs PGRN KO-UNT microglia. Between Ctrl-LPS vs Ctrl-UNT, 1,389 upregulated and 1,558 downregulated genes (red) were identified. Between PGRN KO-LPS vs PGRN KO-UNT, 1,227 upregulated and 1,272 downregulated genes were identified. Differential gene

expression analysis was performed using the Wald test with a log2FC cutoff of (abs)1 and p-adjusted value <0.05.
C – Overlap between upregulated and downregulated DEGs in Ctrl-LPS vs Ctrl-UNT and PGRN KO-LPS vs PGRN KO-UNT. The purple curves link identical genes, and the blue curves link genes that belong to the same enriched ontology term. The inner circle represents gene lists, where hits are arranged along the arc. Genes that hit multiple lists are colored in dark orange, and genes unique to a list are shown in light orange. PGRN KO-LPS and Ctrl-LPS upregulated DEG lists share 850 genes, while the downregulated DEG lists share 884 genes.
D, E – Heatmaps of enriched terms across gene lists, colored by p-values. D and E show shared enriched terms of upregulated and downregulated DEGs in PGRN KO-LPS vs PGRN KO-UNT and Ctrl-LPS vs Ctrl-UNT microglia. Only the first 20 enriched terms are shown.

In order to understand the main effect of LPS in microglia, we compared Ctrl LPS-treated (Ctrl-LPS) and Ctrl untreated (Ctrl-UNT) microglia. We found a total of 1,389 upregulated and 1,558 downregulated genes (absolute log2FC > 1, adjusted p-value < 0.05) in Ctrl-LPS microglia (Figure 3.3 B). To determine the transcriptional changes induced by LPS in the absence of *GRN*, we compared PGRN KO-LPS and PGRN KO-UNT microglia, and identified 1,227 upregulated and 1,272 downregulated genes (Figure 3.3 B). By comparing the DEGs of upregulated and downregulated genes in Ctrl-LPS vs Ctrl-UNT and PGRN KO-LPS vs PGRN KO-UNT microglia, we found that there was a substantial overlap of the gene lists (Figure 3.3 C). Among the upregulated genes in PGRN KO-LPS and Ctrl-LPS, 850 DEGs were shared between gene lists, and among the downregulated genes, 884 genes were shared.

We then compared the enriched pathways of upregulated and downregulated genes between Ctrl-LPS vs Ctrl-UNT and PGRN KO-LPS vs PGRN KO-UNT microglia (Figure 3.3 D, E). Not surprisingly, we found that LPS-treated Ctrl and PGRN KO microglia shared virtually the same top enriched pathways of upregulated genes. In both Ctrl-LPS and PGRN KO-LPS, there was a robust enrichment of pathways related to activation of microglia and

inflammatory and immune system responses (hedgehog signaling, IFN-γ response, complement system, TNF-α signaling via NF-kB, IL6/JAK/STAT3 signaling, IL2/STAT5 signaling, p53 pathway, mTORC1 signaling, EMT) (Figure 3.3 D). These results were anticipated, since LPS is a stimulant known to robustly activate microglial cells, thereby eliciting inflammatory responses (224–226).

Upregulated genes involved in cell adhesion and ECM interaction (including the terms apical junction and EMT) were also abundant in both genotypes, suggesting LPS induces microglial remodeling of the ECM. Indeed, LPS induces morphological changes to microglia, such as retraction of processes and adoption of a more amoeboid morphology, and it induces microglia to alter ECM composition (227,228).

PGRN KO-LPS and Ctrl-LPS microglia also showed enrichment for genes involved in glycolysis, including *B4GALT1, TGFA, STC1, PLOD2, AK4, TXN, HK2, ISG20, ELF3, SSIT4, AGRN, CD44* and *IER3*. Interestingly, glycolysis was also enriched among downregulated genes, especially in Ctrl-LPS microglia (Figure 3.3 E). Some of these genes include *IDH1, GCLC, ADORA2B, STMN1, SLC25A10, ALDH7A1, PFKB, LHPP, SDC1*. LPS has been shown to induce glycolysis in microglia (229,230). However, these findings do not provide sufficient evidence to conclude whether glycolysis is upregulated in our model following LPS treatment. Further investigations are necessary to clarify this aspect.

LPS treatment induced dysregulation of a number of genes involved in lipid metabolism in both Ctrl and PGRN KO cells. Biosynthesis of fatty acids was an enriched pathway of upregulated genes (KEGG pathways), including *ELOVL2, ELOVL7, ACSL1, ACSL4* and *ACSL5*. Among these genes, long chain acyl-CoA synthetases (ACSL) stand out, since they catalyze the activation of FAs, i.e., synthesis of acyl-CoA using long-chain fatty

acids, which is the first step in FA metabolism and towards TAG synthesis or β-oxidation (231). Upregulated FA metabolism genes also included *NBN, GPD2, TP53INP2, G0S2, IL4I1, UBE2L6,* and *MGLL*. Moreover, several genes involved in lipid metabolism (including the terms adipogenesis and fatty acid metabolism) were downregulated, including lipoprotein lipase (*LPL*), genes involved in lipid transport and uptake (*FABP4, PPARG, CD36, SCARB1*), mitochondrial fatty acid β-oxidation (*HADH*), and encoding peroxisomes proteins (*PHYH*, *CAT*, *IDH1*). Additionally, the term "bile acid metabolism" includes peroxisome associated genes, encompassing *CAT, CRABP2, DHCR24, IDH2, MSH2, PEX6, ABCB1, ABCB4, SLC23A2, ABCC5, SLC27A2, ABCB9, HSD3B7, GSTK1*. These results align with prior findings indicating that LPS induces lipid accumulation by increased lipid synthesis (107,224,232) while decreasing FA oxidation (233).

Among the enriched pathways of downregulated genes (Figure 3.3 E), there was a clear enrichment in both genotypes for pathways involved in cell cycle (G2M checkpoint, E2F targets). Additionally, apoptosis was an enriched term of upregulated genes in both Ctrl-LPS and PGRN KO-LPS. LPS has been previously shown to induce microglial proliferation (234,235). However, these studies used a low dose (100 ng/ml) of LPS, while high LPS doses, such as the one used in this study (5 ug/ml), are cytotoxic and can cause microglia cell death (236). Our results suggest that LPS treatment leads to increased cell death and cell cycle arrest of human Ctrl and PGRN KO microglia, as in a second stage of activation of microglia characterized by increased microglial activation but reduction of cell proliferation (237).

Reactive oxygen species was another top enriched pathway of downregulated genes shared by Ctrl-LPS and PGRN KO-LPS. Within the reactive oxygen species term, several

genes have antioxidant properties, such as *GCLC, GPX3, CAT* and *PFKB*. This observation aligns with previous studies indicating that LPS induces oxidative stress (238).

Our primary analysis of differential gene expression showed that PGRN KO and Ctrl microglia exhibited very similar responses to LPS treatment, including robust activation of inflammatory pathways and dysregulation of lipid metabolism genes. To further dissect the differences between Ctrl and PGRN KO microglia in response to LPS, we directly compared the transcriptional profiles of PGRN KO and Ctrl microglia treated with LPS. We found a total of 1,147 upregulated and 679 downregulated genes (absolute log2FC > 0.25, adjusted p-value < 0.05) in PGRN KO-LPS microglia (Figure 3.4 A). As shown in Figure 3.4 B, pathway enrichment analysis revealed that PGRN KO-LPS samples exhibited significant enrichment of pathways associated with immune responses and inflammatory processes among both upregulated and downregulated gene sets. These results are congruent with our previous findings that PGRN KO microglia induces changes in the activation state of microglia.

Pathways related to cell cycle were also enriched among upregulated genes, such as mitotic spindle and G2/M checkpoint, suggesting increased cell proliferation. Surprisingly, the top enriched pathway of downregulated genes was MYC targets, including the transcription factor c-MYC, a regulator of cell cycle, apoptosis and DNA damage response (239). This pathway included several ribosomal genes. Traditionally, reduced protein synthesis is associated with decreased cell proliferation (240). However, it is possible that LPS-treated PGRN KO microglia show enhanced proliferation in comparison with LPS-treated controls, in spite of lower translational capacity due to downregulated ribosomal gene expression. In the case of acute myeloid leukemia, for instance, there is a notable decrease in protein synthesis within hematopoietic stem cells. This reduced protein synthesis is thought to

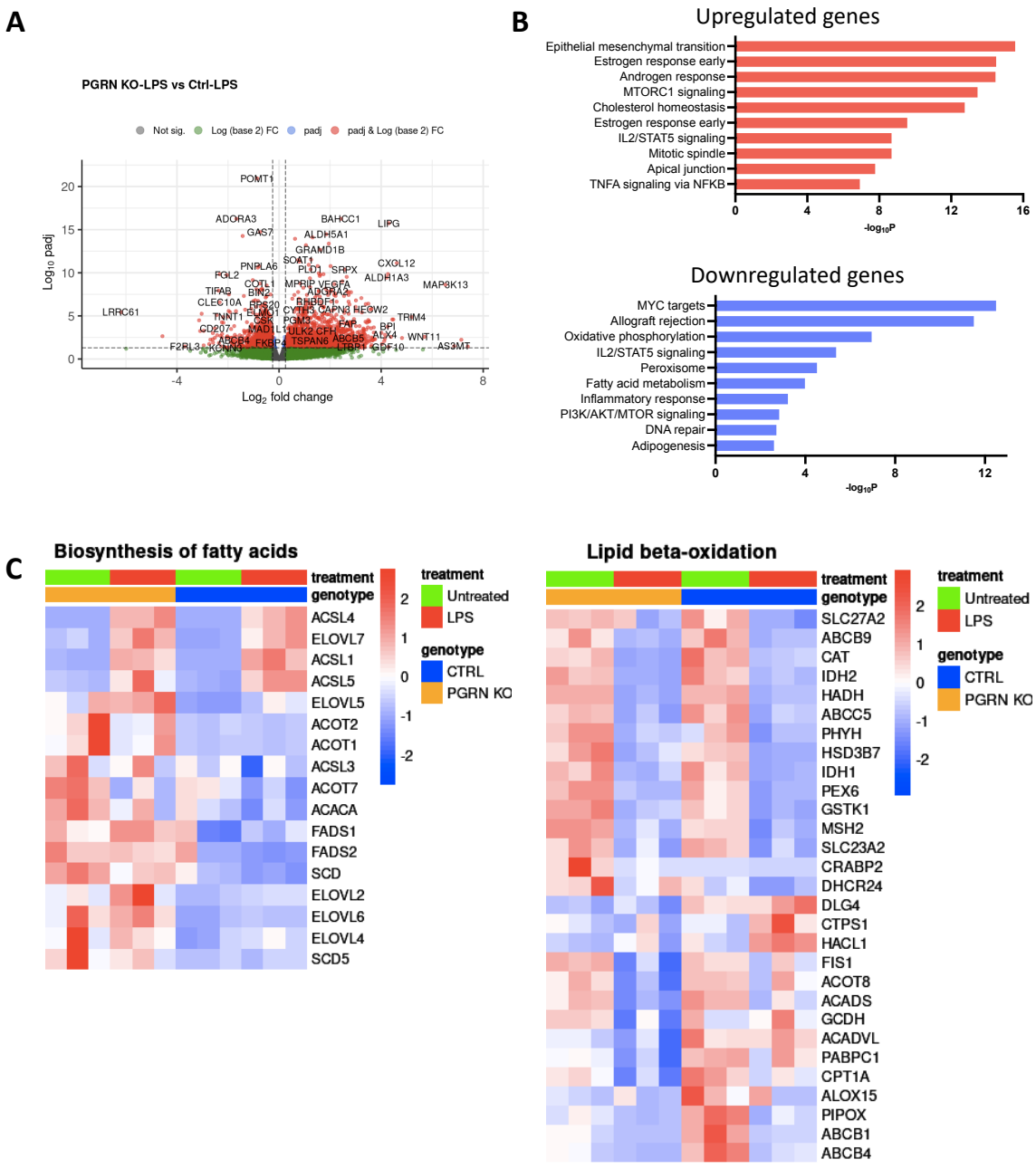

Figure 3.4 – PGRN KO microglia show dysregulation of lipid metabolism genes

A – Volcano plot of differential gene expression results of PGRN KO-LPS vs Ctrl-LPS microglia. 1,147 upregulated and 679 downregulated genes (red) were identified using the Wald test with a log2FC cutoff of (abs)0.25 and p-adjusted value < 0.05. *GRN* was the most downregulated gene and excluded from the graph.

B – Bar graphs of Hallmark enriched pathways across differentially expressed genes (DEG) between PGRN KO-LPS and Ctrl-LPS microglia. The first 500 upregulated genes (ordered by adjusted p-value) were used for the analysis due to the requirements of the software. Enrichment analysis of DEG was performed in GSEA.

C – Heatmaps of expression levels of DEG involved in biosynthesis of fatty acids and mitochondrial and peroxisomal lipid beta-oxidation.

contribute to the enhanced survival of these rapidly dividing cells under conditions of genotoxic stress (241).

Among downregulated genes, OXPHOS was one of the top enriched pathways. On the other hand, PGRN KO-LPS microglia also showed upregulation of several genes involved in glycolysis. LPS has been shown to cause a shift from OXPHOS to glycolysis in microglia, a phenotype of classically activated microglia (229,242,243). Our results suggest that LPS triggers a more pronounced energy metabolism dysfunction in PGRN KO microglia when compared to Ctrl, evidenced by inhibition of OXPHOS and enhanced glycolysis.

Several pathways related to lipid metabolism were dysregulated in PGRN KO-LPS microglia in comparison to Ctrl-LPS cells. Biosynthesis of unsaturated fatty acids was a top enriched pathway (KEGG) of upregulated genes, including *ACSL3, FADS2, FADS1, ACOT2, ACOT1, ACOT7, ELOVL2, ELOVL5, ELOVL6, SCD* and *SCD5*. Fatty acid desaturases FADS1 and FADS2 are responsible for the generation of long-chain PUFAs by introducing double bonds between carbons (244). Upregulated lipid-related genes also included *LIPG*, *DHCR24, PLD1*, *APOE, PPARA, PPARG, LIFR, STOM*. Overexpression of *LIPG, STOM* and *DHCR24* has been associated with lipid droplet (LD) accumulation (245–247), and knockdown of *PLD1* or *LIFR* decreased LD formation (248,249). *PPARA* and *PPARG* are lipid-sensing nuclear receptors that play a central role in lipid metabolism by regulating fatty acid uptake, synthesis, storage and oxidation (212). Furthermore, we identified upregulation of the transcription factor *HIF1A* and several of its target genes. HIF1α is a transcription factor that regulates adaptation

to hypoxia and plays a key role in activation of microglia, and regulates cell survival, migration and energy metabolism (250,251). HIF1α can also become activated by LPS in normoxic conditions (252,253) which in turn can trigger microglial activation and lipid accumulation (254). Among downregulated genes, peroxisome was one of the top enriched terms. Peroxisome-related genes included *FIS1, ACOT8, ABCB1, DLG4, ABCB4, CAT, CTPS1, PABPC1* and *HACL1*. Additionally, we observed downregulation of genes involved in mitochondrial FA β-oxidation (*GCDH, ACADVL, CPT1A, ACADS*) in LPS-treated PGRN KO microglia.

Figure 3.4 – C illustrates the expression changes in genes involved in lipid β-oxidation and synthesis of FAs due to PGRN deficiency and LPS treatment. Our results indicate that PGRN deficiency leads to dysregulated expression of genes associated with FA biosynthesis, metabolism and β-oxidation. Although LPS induces changes in many of these genes in both Ctrl and PGRN KO microglia, microglial activation induces an even more pronounced dysregulation of lipid metabolism in the context of PGRN deficiency.

PGRN loss induces lipid droplet formation in human microglia

PGRN KO deficiency has been shown to induce lipid droplet formation in *GRN*$^{-/-}$ mouse microglia (107,193) and human iPSC-derived neurons (70). Furthermore, LPS provokes lipid droplet accumulation (107,232) and induces enrichment of specific lipid species (224) in microglia. Additionally, our transcriptomic analysis revealed disturbances in lipid metabolism related genes in microglia caused by loss of PGRN at baseline and under LPS treatment. Therefore, we investigated if PGRN loss induces lipid accumulation in our microglia model by using BODIPY 493/503, a dye known for its specific affinity to neutral

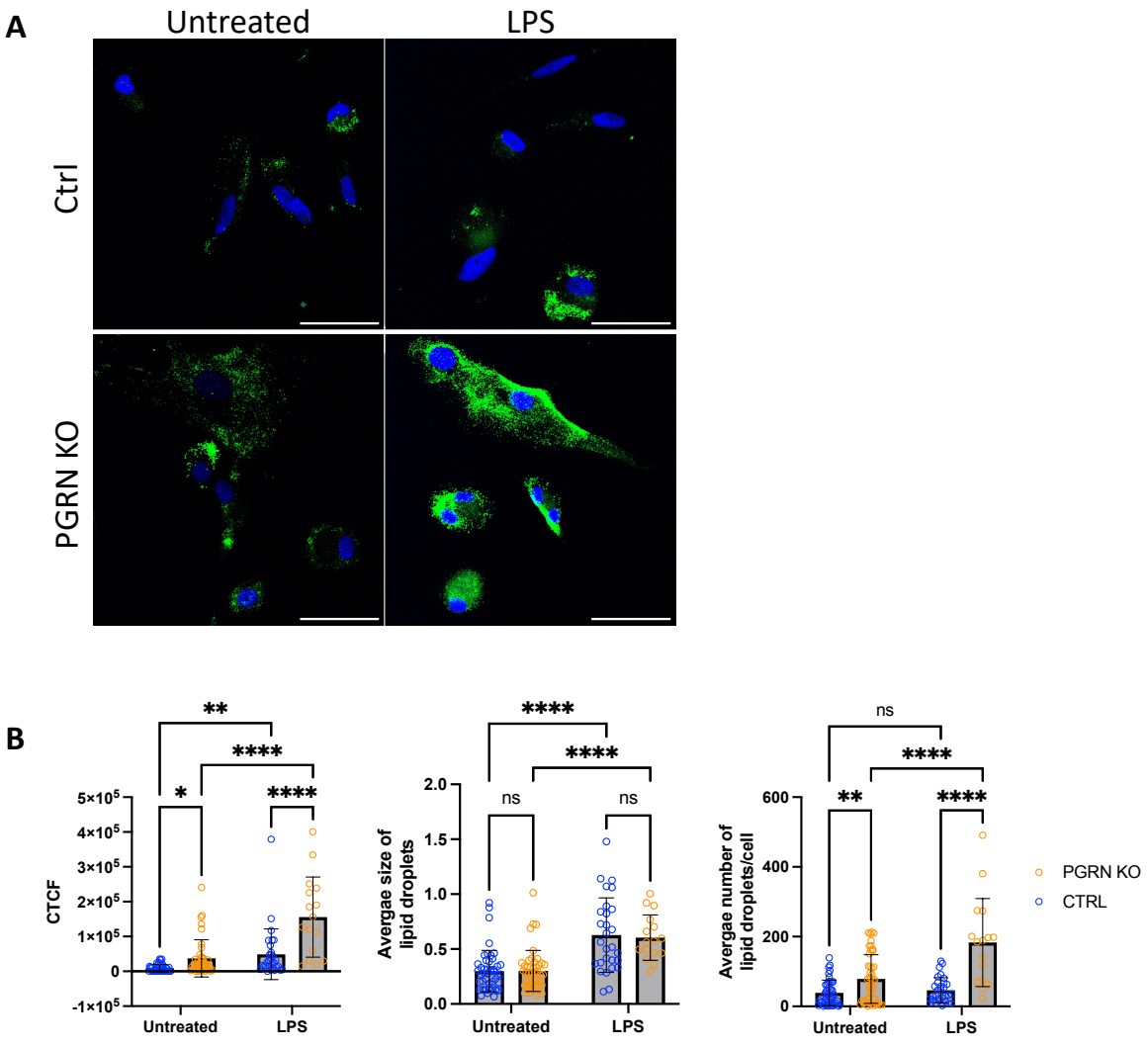

Figure 3.5 – PGRN deficiency leads to accumulation of lipid droplets in microglia
A – Representative images of lipid droplets in Ctrl and PGRN KO microglia by BODIPY 493/503 staining (green). Nuclei were stained with DAPI (blue).
B – Quantification of BODIPY 493/503 in untreated and LPS-treated Ctrl and PGRN KO microglia. CTCF = corrected total cell fluorescence. Scale bars = 50 µm.
Statistical significance was calculated by two-way ANOVA. Bars and error bars represent means ± SD. $^{*}p \leq 0.1$, $^{**}p \leq 0.01$, $^{***}p \leq 0.001$, $^{****}p \leq 0.0001$.

lipids (mostly TAGs and CEs) and frequently employed for lipid droplet detection. Notably,

PGRN KO microglia had significantly more lipid droplets than control cells (Figure 3.5 A, B),

evidenced by higher total BODIPY cell fluorescence and higher number of lipid droplets. When treated with LPS, both control cells and PGRN KO microglia showed increased accumulation of lipid droplets, as expected. However, LPS-treated PGRN KO cells showed a much higher lipid droplet accumulation when compared to controls (Figure 3.5 A, B).

We then investigated lipid accumulation and newly-synthetized lipids in another PGRN deficient human microglia model. We generated a *GRN* knockdown human iPSC-derived microglia line (PGRN KD), by transducing a CRISPRi inducible microglia iPSC cell line with a sgRNA targeting *GRN*. This iPSC-derived microglia model (iTF-microglia) showed the expected ramified microglial morphology and expressed the canonical microglia marker Iba-1 (Figure 3.6 A). Knockdown of *GRN* was confirmed at both mRNA and protein levels (Figure 3.6 A, B). Microglia were fed azide-conjugated paltimitic acid (azide-PA) for the detection of newly-synthetized lipids. Palmitic acid (PA) is the primary end product of FA synthesis in mammalian cells and can be further desaturated and elongated to generate a panel of FAs (255), which are further incorporated into newly-synthesized lipids such as TAGs, CEs and phospholipids through different metabolic processes. Azide was used as an infrared (IF) tag for the detection of newly synthetized lipids. By optical photothermal infrared (OPTIR) microscopy, total and newly-synthesized lipids were mapped with high resolution. Representative OPTIR images at 1744 cm^{-1} (total lipids), 2096 cm^{-1} (newly synthetized lipids), and 1654 cm^{-1} (total protein) are shown in Figure 3.6 C. An increased contrast was evident in both lipid-associated channels for PGRN KD cells. To address potential biomass-related variations in quantification, we normalized the total lipid image against the total protein image (1744/1654). Additionally, the ratio of the newly-synthesized lipid to total lipid was calculated (2096/1744). The ratioed results clearly illustrate increased levels of normalized total lipids

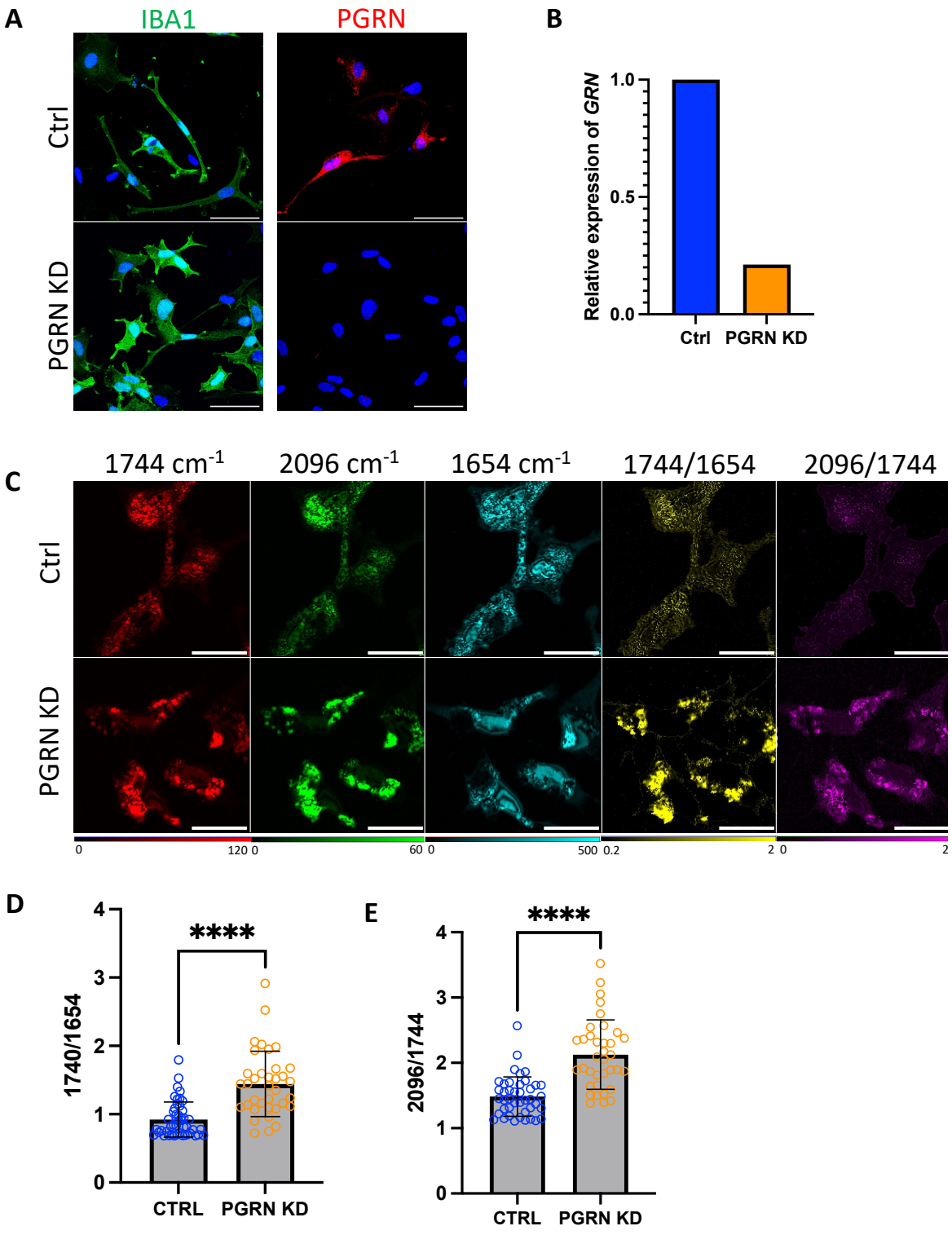

Figure 3.6 – PGRN deficiency leads to increase lipid synthesis and lipid accumulation in microglia

A – Immunofluorescence representative images showing expression levels of PGRN and IBA1 in Ctrl and PGRN-KD iTF-microglia. Sscale bars = 50 µm.

B – *GRN* mRNA expression in PGRN-KD and Ctrl microglia. *GRN* expression was normalized with *PPIA*. Knockdown efficiency was 78.8%.
C – Representative OPTIR images for Ctrl and PGRN-KD microglia at indicated wavenumbers and corresponding ratioed images and brightfield images. Scale bars = 20 μm.
D, E – Ratioed-image based quantification from Ctrl (n = 46) and PGRN-KD (n = 36) microglia. Statistical significance was calculated by two-tailed unpaired *t*-test. Bars and error bars represent means ± SD. $^{*}p \leq 0.1$, $^{**}p \leq 0.01$, $^{***}p \leq 0.001$, $^{****}p \leq 0.0001$.

and newly-synthesized lipid to total lipid ratio. To further validate these observations, we performed quantification based on the mean value extracted from single cells of the ratioed images (Figure 3.6 D, E). Consistent the imaging results, the normalized total lipids revealed a significant lipid accumulation in the PGRN KD microglia when compared to control cells (Figure 3.6 D). Moreover, the increased newly-synthesized to total lipids ratio (Figure 3.6 E) provides direct evidence on the increased lipid metabolism associated with PGRN KD microglia.

Lipidomic analysis of PGRN KO and Ctrl microglia

Previously, it has been shown that PGRN deficiency induces changes in the lipidome of mouse embyonic fibroblasts (73), and human and mouse brains (69,73,191,192). Based on our results and results from other studies, we hypothesized that PGRN loss also induces changes in the lipid profile of human microglia. To investigate that, we performed an unbiased targeted lipidomic analysis of PGRN KO and Ctrl microglia, treated and untreated with LPS (Figure 3.1 A). High-performance liquid chromatography with tandem mass spectrometry (HPLC-MS/MS) yielded 860 detected lipid species. Partial least squares discriminant analysis (PLS-DA) showed some separation between PGRN KO-LPS with Ctrl-LPS and Ctrl-UNT, but variability in PGRN KO-UNT overlapped with the other samples (Figure 3.7.1 A). The

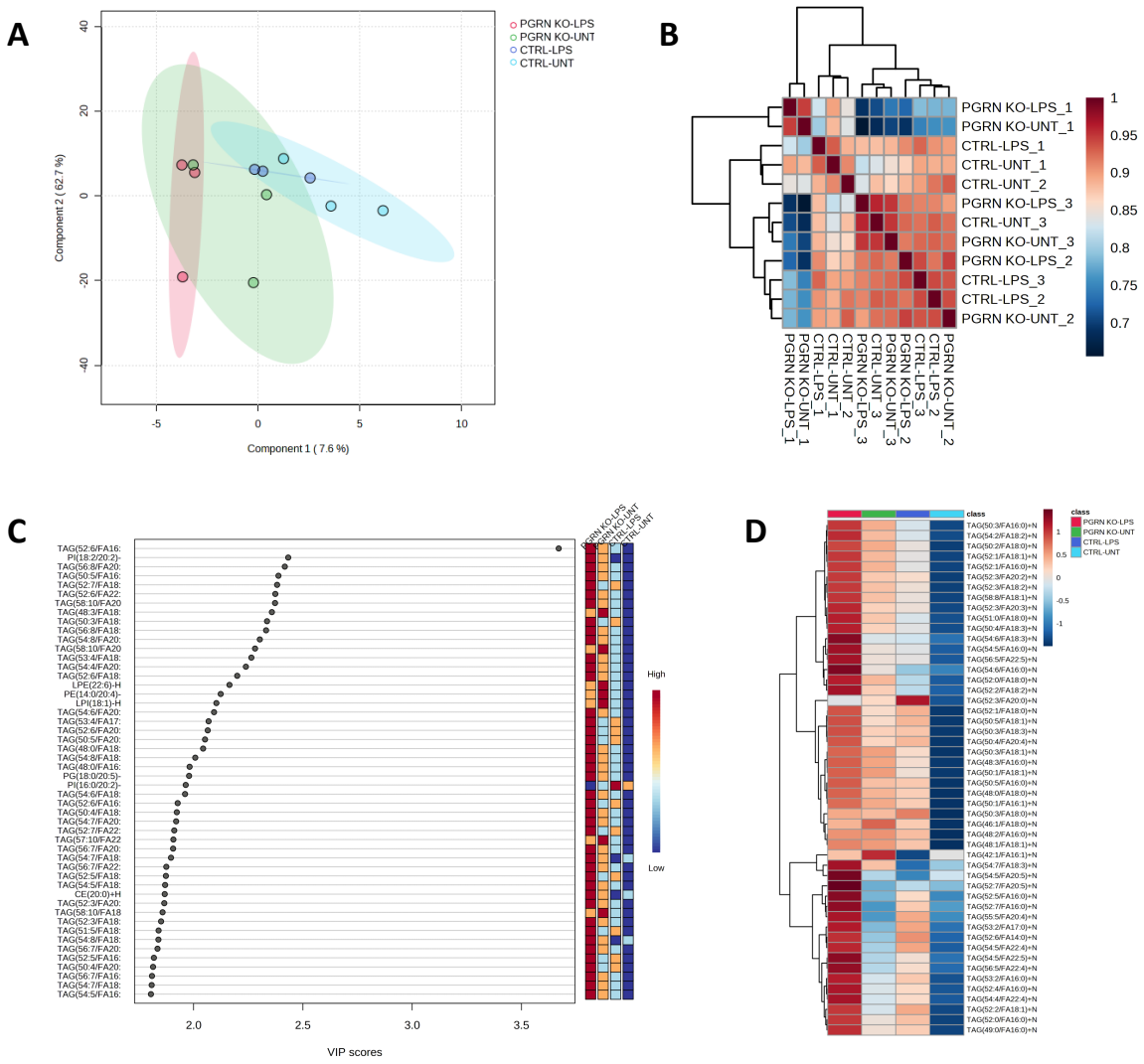

Figure 3.7.1 – Lipidomic analysis of PGRN KO and Ctrl microglia – part 1

A – Partial least squares discriminant analysis (PLS-DA) of PGRN KO-UNT, Ctrl-UNT, PGRN KO-LPS and PGRN KO-UNT samples.

B – Heatmap of the correlation matrix generated by the Pearson r correlation coefficient for all samples.

C – Variable importance in projection (VIP) plot displaying the top 50 most important lipid species identified by PLS-DA. The colored boxes on the right indicate the relative concentrations of the corresponding lipid species in each group of samples.

D – Heatmap of concentrations of the 50 most variable TAGs in all groups.

correlation matrix heatmap (Figure 3.7.1 B) suggested that the correlation patterns partially differed by batch, and two samples of PGRN KO microglia (PGRN KO-UNT_1 and PGRN KO-LPS_1) were poorly correlated with all other samples. Therefore, we removed these samples from subsequent analysis. Variable Importance in Projection (VIP) scores, which estimate the importance of each variable in the projection used in the PLS-DA, showed that the differences between the samples were mainly driven by TAGs (Figure 3.7.1 C). By plotting the 50 most variable TAGs on a heatmap, it was evident that TAGs progressively accumulate from untreated to LPS-treated samples, and from control to PGRN KO cells (Figure 3.7.1 D).

We then compared the lipid profiles of PGRN KO and Ctrl microglia at baseline. VIP scores revealed that most species contributing to group partitioning were TAGs, which were more abundant in PGRN KO (Figure 3.7.2 A). Through differential expression analysis, we found 18 upregulated and 5 downregulated lipid species (1.5 fold difference, p-value < 0.05) in PGRN KO microglia (Figure 3.7.2 B, Table 3.1). Among the upregulated species, 5 were TAGs, 7 phosphatidylethanolamines (PE) and 4 phosphatidylcholines (PC). Among the most variable lipids between PGRN KO and Ctrl cells (Figure 3.7.2 C), there was a trend of more abundant TAGs and phospholipids in PGRN KO microglia, although many of these species were not significantly differentially expressed. Therefore, we looked at the most variable phospholipids and TAGs separately. Among the most variable TAGs, there was a visual enrichment of TAGs with long chain (C16-C18) SFAs and MUFAs in PGRN KO microglia (Figure 3.7.2 D). Among phospholipids, there was an apparent decrease of phospholipids (mostly PE) with highly unsaturated very long chain fatty acids (VLCFA, fatty acids with 20 or more carbon atoms), and most of upregulated species contained long chain (14-20 carbons) SFAs and MUFAs (Figure 3.7.2 E). The accumulation of SFAs and MUFAs could be due to

PGRN KO-UNT vs Ctrl-UNT	
Lipid species	**Log2(FC)**
PS(14:0/20:1)	-4.656
PS(18:0/18:2)	-4.3262
PS(16:0/20:3)	-3.4121
PE(14:0/18:3)	-3.054
PE(O-18:0/22:4)	-0.90129
FFA 18:1	0.69638
PC(14:1/14:1)	0.76008
PC(18:2/18:3)	0.86322
PE(P-16:0/20:5)	0.8754
PC(18:1/20:5)	1.0064
PE(16:0/20:5)	1.0512
DCER(18:1)	1.1168
PC(18:0/18:3)	1.1224
PE(14:0/20:2)	1.2486
PE(18:1/20:5)	1.3727
TAG(44:0/FA16:0)	1.502
PE(P-18:0/18:3)	1.5138
PE(P-18:0/16:0)	1.6739
TAG(46:1/FA18:0)	2.1105
TAG(48:5/FA18:3)	2.9621
TAG(50:5/FA16:0)	3.4835
PE(14:0/20:4)	4.1068
TAG(57:10/FA22:6)	4.1939

Ctrl-LPS vs Ctrl-UNT	
Lipid species	**Log2(FC)**
CER(18:0)	0.74209
DAG(14:0/16:1)	1.9397
DCER(18:1)	1.6241
DCER(24:0)	2.3385
DCER(24:1)	1.7011
PE(14:0/18:2)	0.73935
PE(14:0/20:4)	3.0705
PE(16:0/14:0)	0.68057
PE(18:2/18:2)	0.65099
PG(16:0/14:0)	0.68177
PG(16:0/20:1)	0.8062
PG(18:0/20:2)	0.7206
PI(18:1/20:5)	-5.2533
TAG(46:1/FA18:0)	1.5332
TAG(47:1/FA14:0)	1.5655
TAG(48:0/FA18:0)	2.3869
TAG(48:1/FA18:1)	1.3083
TAG(48:2/FA16:0)	1.261
TAG(48:3/FA16:0)	1.731
TAG(48:4/FA20:4)	2.3215
TAG(49:0/FA16:0)	1.456
TAG(49:1/FA14:0)	2.0437
TAG(50:1/FA16:1)	1.6081
TAG(50:2/FA18:0)	1.3582
TAG(50:3/FA16:1)	1.5573
TAG(50:3/FA18:0)	1.6408
TAG(50:3/FA18:3)	2.651
TAG(50:4/FA20:4)	2.6992
TAG(50:5/FA16:0)	3.4018
TAG(50:5/FA18:2)	1.7387
TAG(51:0/FA18:0)	1.3761
TAG(51:1/FA16:0)	1.2994
TAG(51:2/FA17:0)	1.7553
TAG(52:0/FA16:0)	1.6597
TAG(52:0/FA20:0)	1.6946
TAG(52:2/FA18:1)	1.5124
TAG(52:3/FA20:0)	2.8252
TAG(52:3/FA20:2)	1.3027
TAG(52:6/FA14:0)	2.8855
TAG(53:2/FA16:0)	1.2798

PGRN KO-LPS vs PGRN KO-UNT	
Lipid species	**Log2(FC)**
CER(22:1)	-0.71381
LPE(18:3)	3.8834
PS(16:0/16:0)	-0.9336
PS(16:0/20:3)	3.5333
TAG(46:0/FA16:0)	-0.92696
TAG(47:1/FA17:0)	-2.0483
TAG(51:4/FA18:3)	1.9633
TAG(52:4/FA18:1)	1.5316
TAG(52:6/FA16:1)	2.4402
TAG(52:6/FA18:2)	2.1722
TAG(52:6/FA20:4)	2.5888
TAG(52:7/FA18:1)	3.2803
TAG(52:8/FA18:2)	5.9939
TAG(53:2/FA17:0)	1.4987
TAG(54:1/FA20:0)	1.4905
TAG(54:4/FA20:4)	1.5349
TAG(54:5/FA16:0)	1.5819
TAG(54:5/FA16:1)	1.4304
TAG(54:5/FA18:0)	1.3983
TAG(54:5/FA20:5)	2.069
TAG(54:6/FA16:0)	1.4831
TAG(54:6/FA18:3)	2.104
TAG(54:6/FA22:6)	2.5752
TAG(54:7/FA16:1)	1.9739
TAG(54:7/FA18:1)	2.222
TAG(54:7/FA18:3)	1.5352
TAG(54:7/FA20:4)	2.0408
TAG(54:7/FA20:5)	1.3298
TAG(54:7/FA22:5)	1.4435
TAG(54:8/FA22:6)	1.4262
TAG(55:1/FA16:0)	2.0367
TAG(55:1/FA18:1)	1.6028
TAG(55:3/FA18:2)	1.4818
TAG(55:5/FA20:4)	3.0608
TAG(56:5/FA16:0)	1.7467
TAG(56:5/FA22:4)	1.6378
TAG(56:6/FA18:0)	0.95729
TAG(56:7/FA18:1)	0.95634
TAG(56:9/FA20:4)	1.1741
TAG(60:12/FA22:6)	-1.8492

PGRN KO-LPS vs Ctrl-LPS	
Lipid species	**Log2(FC)**
CER(16:0)	-0.89195
CER(18:0)	-1.2439
DAG(18:1/22:5)	-2.0251
FFA 22:4	-1.383
PC(18:1/20:5)	1.2666
PC(18:1/22:4)	-1.0999
PC(18:2/20:5)	1.1481
PE(18:1/20:5)	1.3592
PE(O-18:0/20:3)	-1.5625
PE(P-18:1/16:0)	0.77695
PE(P-18:1/16:1)	0.92703
PG(14:0/20:2)	1.2265
PG(18:1/18:3)	0.76101
PG(18:1/20:2)	0.99758
PG(18:1/20:3)	1.0953
PI(16:0/20:2)	-5.1341
PI(18:2/20:2)	4.9201
TAG(46:1/FA16:0)	1.1811
TAG(48:0/FA14:0)	1.2589
TAG(48:3/FA16:0)	0.91675
TAG(48:3/FA18:3)	2.0437
TAG(50:0/FA18:0)	1.5305
TAG(50:1/FA16:0)	1.225
TAG(50:1/FA18:1)	0.82747
TAG(50:3/FA18:3)	1.0648
TAG(50:4/FA18:3)	1.603
TAG(52:0/FA18:0)	1.3122
TAG(52:1/FA16:0)	0.9046
TAG(52:1/FA18:1)	1.0266
TAG(52:2/FA18:2)	1.4662
TAG(52:3/FA20:3)	1.394
TAG(52:5/FA16:0)	1.801
TAG(52:7/FA20:5)	3.1973
TAG(53:4/FA16:0)	1.1229
TAG(54:3/FA18:0)	0.88352
TAG(54:3/FA20:3)	1.323
TAG(54:4/FA20:3)	0.9234
TAG(54:4/FA22:4)	1.0639
TAG(54:5/FA16:0)	1.7315
TAG(54:5/FA20:3)	1.4455
TAG(54:5/FA20:5)	2.5065
TAG(54:5/FA22:5)	1.5575
TAG(54:6/FA16:0)	1.9427
TAG(54:6/FA18:3)	2.1314
TAG(54:6/FA20:5)	2.2071
TAG(54:7/FA16:1)	1.3832
TAG(54:7/FA18:3)	3.5031
TAG(54:7/FA20:4)	2.2394
TAG(54:7/FA20:5)	1.6497
TAG(54:7/FA22:5)	1.5033
TAG(54:7/FA22:6)	1.88
TAG(54:8/FA20:4)	2.5741
TAG(54:8/FA20:5)	2.6268
TAG(55:1/FA16:0)	2.1069
TAG(55:1/FA18:1)	1.8561
TAG(55:5/FA18:2)	0.75806
TAG(55:5/FA20:4)	1.1425
TAG(56:5/FA16:0)	1.051
TAG(56:5/FA18:0)	1.0942
TAG(56:5/FA22:4)	1.1884
TAG(56:5/FA22:5)	1.0201
TAG(56:6/FA16:0)	1.2617
TAG(56:6/FA18:0)	1.7966
TAG(56:6/FA18:2)	1.2989
TAG(56:6/FA20:4)	1.3628
TAG(56:6/FA22:6)	1.3895
TAG(56:7/FA16:0)	1.8364
TAG(56:7/FA16:1)	1.149
TAG(56:7/FA20:4)	2.5149
TAG(56:7/FA20:5)	1.434
TAG(56:7/FA22:6)	1.7889
TAG(56:8/FA16:1)	1.9445
TAG(56:8/FA18:3)	2.3329
TAG(56:9/FA18:3)	2.2186
TAG(58:6/FA22:5)	1.3429
TAG(58:7/FA18:1)	0.88784

Table 3.1 – Differentially expressed lipids in untreated and LPS-treated Ctrl and PGRN KO microglia
Differentially expressed lipids species between groups and log2FC values. Differential expression analysis was calculated by t-test with a FC cutoff of 1.5 and p-adjusted value < 0.05.

elevated de novo lipogenesis, and enhanced activity of SCDs. Indeed, we found upregulation in PGRN KO microglia of *ACACA*, which encodes for first rate-limiting enzyme in de novo lipogenesis, which primary products are SFAs (209,256). *SCD1* and *SCD5* were also upregulated in PGRN KO microglia, and they generate MUFAs from SFAs. Interestingly, PGRN KO microglia showed upregulation of several genes encoding fatty acid elongases (ELOVLs), but enrichment of long (and not very long) chain FAs with 16 and 18 carbons. Nonetheless, ELOVL6, responsible for the elongation of C12-C16 acyl-CoAs was the most upregulated gene among all ELOVLs, suggesting increased activity of this enzyme. Moreover, the transcriptomic profile of PGRN KO microglia suggests these cells exhibit increased glycolysis, which can drive lipogenesis by providing citrate for the FA synthesis pathway (190,257). The downregulation of *ACADVL* could also play a role in lipid accumulation in PGRN KO cells. *ACADVL* deficiency causes very long-chain acyl-CoA dehydrogenase deficiency (VLCADD), a disease characterized by accumulation of C14-C20 fatty acids (258). Furthermore, the accumulation of TAGs can happen by transfer of fatty acids from membrane lipids. PGRN KO microglia show upregulation of genes encoding for the phospholipases *PLAAT4* and *PLA2G2D*, that hydrolyze FAs from membrane phospholipids (259). The decrease of expression of phospholipids with VLCFA and high unsaturation levels could be due to upregulation of these enzymes, especially PLA2G2D, that has more affinity to

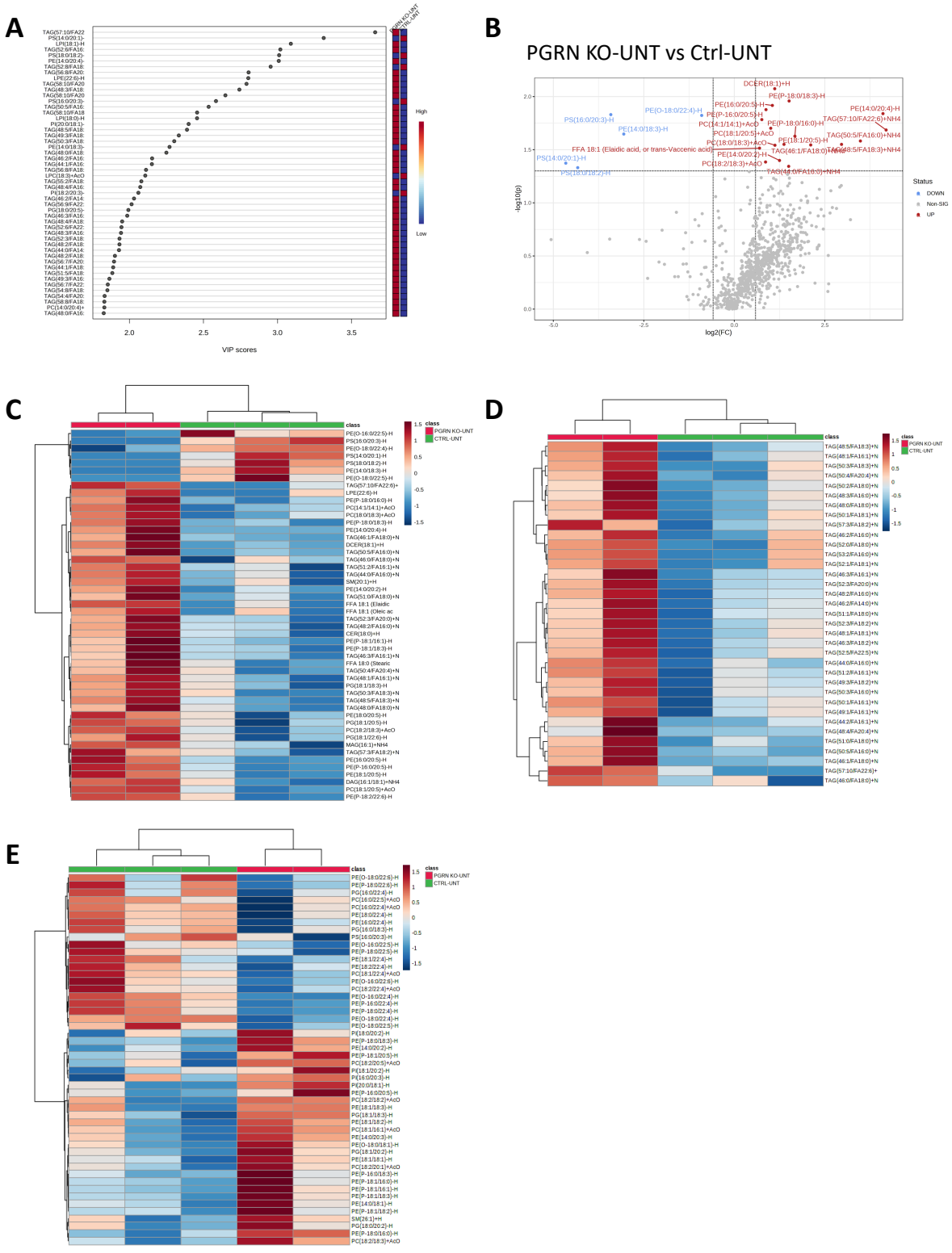

Figure 3.7.2 – Lipidomic analysis of PGRN KO and Ctrl microglia – part 2
A – Variable importance in projection (VIP) plot displaying the top 50 most important lipid species identified by PLS-DA between Ctrl-UNT and PGRN KO-UNT samples. The colored

boxes on the right indicate the relative concentrations of the corresponding lipid species in each group of samples.
B – Volcano plot of differentially expressed lipid species between PGRN KO-UNT and Ctrl-UNT microglia. Differential expression analysis was calculated by t-test with a FC cutoff of 1.5 and p-adjusted value < 0.05.
C – Heatmap of concentrations of the 50 most variable lipid species in PGRN KO-UNT and Ctrl-UNT samples.
D – Heatmap of concentrations of the 35 most variable TAGS in PGRN KO-UNT and Ctrl-UNT samples.
E – Heatmap of concentrations of the 50 most variable phospholipids in PGRN KO-UNT and Ctrl-UNT samples.

phosphatidylethanolamines and phosphatidylserines with highly unsaturated and very long acyl chains (260,261).

We then compared untreated and LPS-treated Ctrl microglia, to investigate the main effect of LPS in cell lipid composition. We found 1 downregulated and 39 upregulated lipid species (Figure 3.7.3 A, B; Table 3.1) in LPS-treated Ctrl cells. These included 27 upregulated TAGs, with an accumulation of TAGs with SFAs and MUFAs. By comparing untreated and LPS-treated PGRN KO microglia, we noticed an even higher enrichment of TAGs – upregulated TAGs made up 36 of the 40 differentially expressed lipids (Figure 3.7.3 C, D; Table 3.1). Compared to Ctrl-LPS, PGRN KO-LPS exhibited a preferential accumulation of TAGs with longer acyl chains and high unsaturation levels (Table 3.1). 36% of statically significant upregulated TAGs in PGRN KO-LPS had VLCFA, in comparison with only 18% of TAGs in Ctrl-LPS. Out of the VLCFA of TAGs in PGRN KO-LPS, 92% had 3 or more double bonds, compared with only 40% of the upregulated VLCFA in Ctrl-LPS. By directly comparing PGRN KO-LPS and Ctrl-LPS (Figure 3.7.3 E, F; Table 3.1), we found 76 differentially expressed lipid species, most of them upregulated, of which 59 were TAGs. Not surprisingly, there was a preferential accumulation of TAGs with long or very long unsaturated

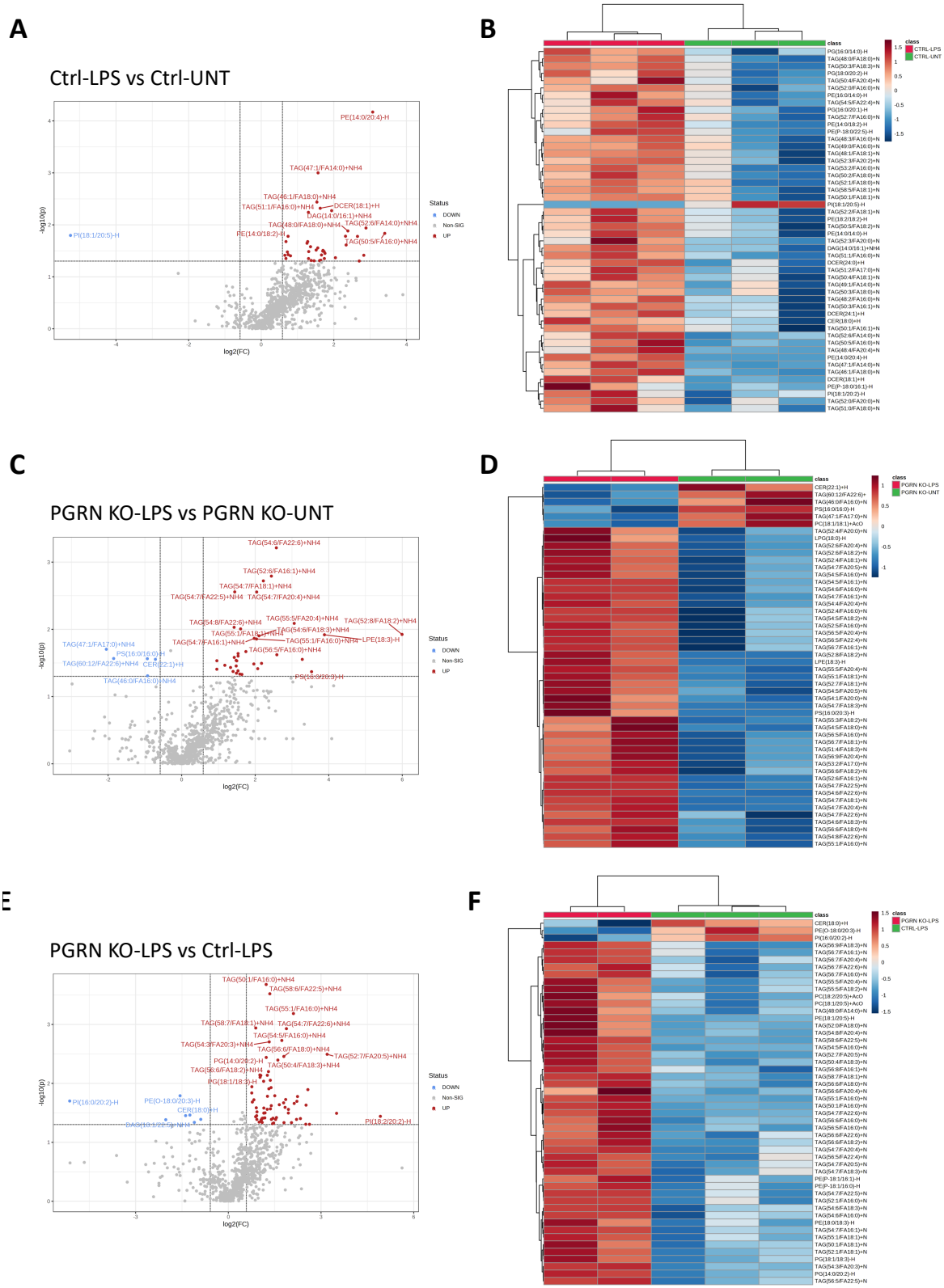
A
Ctrl-LPS vs Ctrl-UNT
PE(14:0/20:4)-H
TAG(47:1/FA14:0)+NH4
TAG(46:1/FA18:0)+NH4
TAG(51:1/FA16:0)+NH4
DCER(18:1)+H
DAG(14:0/16:1)+NH4
TAG(48:0/FA18:0)+NH4
TAG(52:6/FA14:0)+NH4
PE(14:0/18:2)-H
TAG(50:5/FA16:0)+NH4
PI(18:1/20:5)-H
-log10(p)
log2(FC)
Status
DOWN
Non-SIG
UP
B
class
CTRL-LPS
CTRL-UNT
C
PGRN KO-LPS vs PGRN KO-UNT
TAG(54:6/FA22:6)+NH4
TAG(52:6/FA16:1)+NH4
TAG(54:7/FA18:1)+NH4
TAG(54:7/FA22:5)+NH4
TAG(54:7/FA20:4)+NH4
TAG(54:8/FA22:6)+NH4
TAG(55:5/FA20:4)+NH4
TAG(52:8/FA18:2)+NH4
TAG(55:1/FA18:1)+NH4
TAG(54:6/FA18:3)+NH4
TAG(47:1/FA17:0)+NH4
TAG(54:7/FA16:1)+NH4
TAG(55:1/FA16:0)+NH4
LPE(18:3)-H
PS(16:0/18:0)-H
TAG(56:5/FA16:0)+NH4
TAG(60:12/FA22:6)+NH4
CER(22:1)+H
PS(16:3/20:3)-H
TAG(46:0/FA16:0)+NH4
D
class
PGRN KO-LPS
PGRN KO-UNT
E
PGRN KO-LPS vs Ctrl-LPS
TAG(50:1/FA16:0)+NH4
TAG(58:6/FA22:5)+NH4
TAG(55:1/FA16:0)+NH4
TAG(58:7/FA18:1)+NH4
TAG(54:7/FA22:6)+NH4
TAG(54:5/FA16:0)+NH4
TAG(54:3/FA20:3)+NH4
TAG(56:6/FA18:0)+NH4
TAG(52:7/FA20:5)+NH4
PG(14:0/20:2)-H
TAG(50:4/FA18:3)+NH4
TAG(56:6/FA18:2)+NH4
PG(18:1/18:3)-H
PI(16:0/20:2)-H
PE(O-18:0/20:3)-H
CER(18:0)+H
DAG(18:1/22:6)-NH4
PI(18:2/20:2)-H
F
class
PGRN KO-LPS
CTRL-LPS

Figure 3.7.3 – Lipidomic analysis of PGRN KO and Ctrl microglia – part 3
A, C, E – Volcano plot of differentially expressed lipid species. Differential expression analysis was calculated by t-test with a FC cutoff of 1.5 and p-adjusted value < 0.05.
B, D, F - F – Heatmaps of concentrations of the 50 most variable lipid species between each group.

fatty acyl chains in PGRN KO-LPS microglia (Table 3.1). The heatmaps of the most variable species further confirm these results and clearly show the enrichment of TAGs in LPS-treated samples (Figure 3.7.3 B, D, F). The increased expression of *ELOVL* genes (especially *ELOVL2* and *ELOVL5*) due to LPS treatment could explain the longer acyl chains present in LPS-treated PGRN KO microglia, and the high unsaturation levels are likely due to increased activity of the desaturase enzymes FADS1 and FADS2, that generate long-chain PUFAs. Moreover, we found downregulation of mitochondrial and peroxisomal-related genes in LPS-treated PGRN KO microglia, which suggests deficiency in β-oxidation of FAs, that could lead to lipid accumulation (262). Additionally, upregulation of key lipid-metabolism genes such as *LIPG* and *PLD1* could also be related to the robust intracellular accumulation of lipids in LPS-treated PGRN KO microglia.

Our lipidomics results confirm the accumulation of neutral lipids observed in PGRN deficient microglia, especially with LPS treatment, and further underscore the significant role that PGRN plays in lipid metabolism, particularly TAGs and phospholipids.

3.5 Discussion

In this study, we used human iPSC-derived microglia, a disease-relevant model, to examine complete PGRN deficiency. Recent research has shown that mouse microglia and

human iPSC-derived neurons lacking PGRN tend to accumulate lipid droplets (70,107,193), and PGRN deficient microglia exhibit a more pronounced increase in lipid droplets when stimulated with LPS (107). Our study substantiated these findings, by demonstrating that PGRN-deficient human microglia accumulated more lipid droplets under baseline conditions and upon activation with LPS treatment. We validate our results in another iPSC-derived microglia model for progranulin deficiency, that not only showed accumulation of total lipids but also increased levels of newly-synthetized neutral lipids through incorporation of palmitic acid.

Analysis of microglia lipid extracts showed that loss of progranulin also leads to changes in the lipidome. PGRN KO deficiency caused a preferential accumulation of TAGs in microglia, and the difference was more pronounced when microglia were stimulated with LPS. At baseline, PGRN KO microglia showed a trend for enrichment of TAGs with SFAs and MUFAs, while LPS-activated PGRN KO microglia accumulated TAGs with very long and highly unsaturated acyl chains. Changes in the lipidome of PGRN-deficient mouse embyonic fibroblasts and human and mouse brains have been previously reported (69,73,191,192). The lipid profile of LPS-treated PGRN KO microglia closely resembles the lipid profile of PGRN deficient MEFs described by Evers *et al*., 2017 (73). In this study, the authors reported accumulation of TAGs with long acyl chains and high unsaturation levels in *GRN*$^{-/-}$ MEFs, and a corresponding decrease in diacylglycerides (DAG) and phosphatidylserines (PS) of increased length and unsaturated bonds, which we did not replicate in our study. In spite of that, we found an apparent decrease in phospholipids (mainly PE) with highly unsaturated VLCFA in PGRN KO microglia. It has been hypothesized that the dysregulation in lipid metabolism could be attributed to lysosomal dysfunction resulting from PGRN loss. One of the hallmarks of CLN11

is the accumulation of lipofuscin in the lysosomes, a finding that provided the first clue on progranulin's involvement in lysosomal function (18). Furthermore, numerous studies have provided evidence supporting the crucial role of PGRN in the regulation of lysosomal function. PGRN regulates acidification of lysosomes (67), and PGRN loss leads to enlarged lysosomes with altered morphology (33,263), impaired lysosomal protease activity (19,264), impaired lysosomal regulation of lipids, including glycosphingolipids (68–70) and TAGs, PS and PEs (73), and upregulation of lysosomal genes (32,67,74,264). Although these changes are not always due to transcriptional dysregulation of specific enzymes, we found upregulation of several lysosomal genes in PGRN KO microglia.

Increased inflammation can result in accumulation of intracellular lipids in immune cells (190,265). Indeed, LPS-treated microglia show lipid droplet accumulation (107,232) and lipid droplets form in immune cells during activation and in response to inflammation (266,267). Moreover, lipid-accumulating APOE4 and ageing microglia show a pro-inflammatory phenotype (107,222). Most revealing, lipid-rich microglia from *GRN*$^{-/-}$ mice show elevated secretion of proinflammatory cytokines when compared to microglia with low lipid accumulation (107). In line with these observations, we found that in both control and PGRN KO microglia, LPS treatment induced transcriptomic changes that suggest a strong inflammatory response, and concomitant lipid accumulation. Nonetheless, in comparison to Ctrl microglia, PGRN KO microglia exhibit a mix of upregulated and downregulated genes related to inflammation at baseline and in response to LPS treatment, which raised uncertainty about the inflammatory profile of these cells compared to controls. Based on the stated above, we suggest that PGRN deficiency induces a pro-inflammatory response in microglia, that could partly explain the observed robust lipid accumulation.

We hypothesize that the lipid metabolism dysregulation that we observed in PGRN deficient cells might not only be due to lysosomal dysfunction and/or increased inflammation, but also due to metabolic changes towards increased FA synthesis and decreased FA β-oxidation. We found that PGRN KO microglia showed upregulation of genes encoding for enzymes responsible for de novo lipogenesis (*ACACA*), fatty acid elongation (*ELOVLs*), desaturation (*SCD1* and *SCD5*), and dysregulation of numerous genes involved in lipid metabolism, including genes that encode for major lipid sensing nuclear receptors such as LXRα and PPARγ. Moreover, PGRN KO microglia showed downregulation of β-oxidation genes, including *ACADVL,* an essential enzyme in the mitochondrial β-oxidation pathway. This transcriptional signature could explain the accumulation of TAGs, especially the ones containing SFA and MUFAs. When activated by LPS, the lipid profile dysregulation in PGRN KO microglia was more prominent, accompanied by further dysregulation of expression of some of the aforementioned enzymes and other lipid-related genes. Expression of desaturases *FADS1* and *FADS2*, fatty acid elongases *ELOVLs*, and the acyl-CoA synthetase *ACSL3* was increased in LPS-treated PGRN KO microglia, and could be partially responsible for the accumulation of highly saturated VLCFA in these cells. Lipid sensing nuclear receptors PPARα and PPARγ, that regulated several aspects of lipid metabolism, were also upregulated. We also noticed downregulation of numerous genes that play a key role in peroxisomal and mitochondrial β-oxidation. VLCFA are exclusively metabolized by β-oxidation in peroxisomes, and one of the hallmarks of peroxisomal disorders is the accumulation of VLCFA (268,269). On the other hand, defects in mitochondrial β-oxidation lead to accumulation of medium and long chain (up to 20 carbons) fatty acids (213,270). The dysregulation in lipid metabolism and fatty acid β-oxidation dysfunction in microglia may lead to a more pronounced

pro-inflammatory response, resulting in a vicious cycle of immune-metabolic dysregulation (190,271,272).

Pro-inflammatory stimuli, such as LPS, has been shown to cause a metabolic switch from OXPHOS to glycolysis in microglia (229,242). We observed decreased expression of OXPHOS genes in LPS-treated PGRN KO microglia compared to Ctrl, accompanied by upregulation of genes associated with glycolysis, while only glycolysis was upregulated in PGRN KO microglia at baseline. This indicates that PGRN loss results in deficits in mitochondrial function of activated microglia. That could be the result of a more pronounced pro-inflammatory profile of these cells, or a direct effect of progranulin loss in mitochondrial function that becomes prominent with microglial activation. PGRN deficiency has been previously linked to decreased mitochondrial respiration (131,170–172). However, further research is required to elucidate the underlying cause of the apparent OXPHOS dysfunction observed in activated PGRN KO microglia. The decrease mitochondrial OXPHOS can also indirectly result in increased lipid accumulation. A decreased OXPHOS results in disruption of the tricarboxylic acid cycle (TCA) cycle and induced glycolysis, that becomes enhanced to compensate for the OXPHOS dysfunction and energy depletion (273). The resulting excess citrate is then converted to acetyl-coA, that feeds the FA synthesis pathway and can be stored in lipid droplets (190,257).

Limitations of the study

The PLS-DA and correlation matrix heatmap of our lipidomics samples indicated batch effects. To substantiate our lipidomics analysis, our data requires validation with ideally a higher sample size. The lipidomics methodology used in this study doesn't allow for the

determination of detailed fatty acid composition of TAGs, so it would be of great value to perform a method that would allow that. Moreover, it would be interesting to investigate the transcriptomic and lipidomic profiles of PGRN KO microglia in a more complex model with multiple cell types, i.e., cerebral organoids. Additionally, it would be intriguing to explore whether recombinant PGRN can ameliorate the observed effects in PGRN KO microglia.

Chapter 4

Summary

CLN11 and FTD-GRN are highly debilitating neurodegenerative disorders caused by mutations in the *GRN* gene. While it is well established that mutations in *GRN* are the underlying cause of these diseases, the precise mechanisms through which PGRN contributes to neurodegeneration remain unknown. Unfortunately, there exists no cure for these conditions, and available treatments do not have the capability to halt or impede disease progression.

Many PGRN studies have relied on murine models to investigate PGRN and its brain function. While informative, these models imperfectly recapitulate human diseases, particularly those linked to PGRN. Additionally, research on PGRN involving human cells has primarily utilized 2D cultures, and focused on neuronal models. In our study, we took a distinct

approach, generating *GRN* null human iPSC-derived forebrain organoids and microglia to explore the effects of loss-of function of PGRN loss in brain cells.

In chapter 2, we investigated PGRN loss within forebrain organoids, enabling an investigation of the impact of PGRN deficiency on both neuronal and glial populations. In contrast to conventional 2D cell cultures, 3D cerebral organoids provide a more physiologically relevant milieu that partly replicates the cellular diversity and structural features of the human brain. Through scRNA-seq, we found pronounced mitochondrial dysfunction in response to PGRN loss across all identified cell types, characterized by the downregulation of electron transport chain (ETC) genes. In line with these findings, PGRN KO organoids showed diminished mitochondrial respiration. PGRN-deficient organoids also exhibited increased cellular reactive oxygen species (ROS), which we hypothesize may be a result of impaired oxidative phosphorylation, particularly compromised activity of complexes I and III. Elevated ROS levels can induce lipid peroxidation, primarily targeting polyunsaturated fatty acids (PUFAs) within cell membranes. Our study corroborated exacerbated lipid peroxidation within PGRN-deficient organoids, consistent with the findings of excessive ROS. Given that lipid peroxidation is a hallmark of ferroptosis, an iron-dependent form of cell death associated with increased lipid peroxidation, we hypothesized that PGRN-deficient cells might exhibit heightened susceptibility to ferroptosis. Our results not only validated this hypothesis but also revealed that this increased vulnerability was accompanied by intracellular ferrous iron accumulation. In PGRN-deficient neurons, we identified the downregulation of several ferroptosis suppressor genes, particularly GPX4, a pivotal regulator of ferroptosis, suggesting that neurons could be particularly susceptible to ferroptotic cell death in the context of PGRN deficiency. This study revealed a complex interplay between

mitochondrial dysfunction, oxidative stress, and an amplified susceptibility to ferroptosis in the context of PGRN deficiency, highlighting the potential role of these features as early contributors to neurodegeneration associated with PGRN deficiency.

PGRN plays a pivotal role in regulating the function of microglia—a cell type instrumental in neurodegeneration resulting from PGRN loss, and that is absent in our organoid model. Therefore, in chapter 3, we ventured to investigate PGRN loss using a human iPSC-derived microglia model. Previous research had showed at the accumulation of lipid droplets in PGRN-deficient microglia. We confirmed these findings, and observed augmented lipid droplet accumulation in PGRN-deficient human microglia under baseline conditions and following microglial activation induced by LPS treatment. Through lipidomic analysis, we further investigated alterations in lipid composition within PGRN-deficient microglia. Our findings revealed a preference of PGRN-deficient microglia for accumulating TAGs, with a more pronounced effect following LPS stimulation. Interestingly, we detected distinct TAG profiles in untreated and LPS-activated microglia - TAGs exhibited an enrichment of saturated and monounsaturated fatty acids at baseline, and very long and highly unsaturated acyl chains after LPS activation. The perturbation in lipid metabolism observed in PGRN-deficient microglia may arise from various factors, including lysosomal dysfunction and exacerbated inflammation. Indeed, our RNA-seq analysis showed dysregulation in genes associated with lysosomes and those involved in the inflammatory response within PGRN-deficient microglia. Moreover, transcriptomic analysis unveiled the upregulation of genes responsible for de novo lipogenesis, fatty acid elongation, and the dysregulation of numerous genes related to lipid metabolism in PGRN-deficient microglia. When it came to LPS-treated microglia, the dysfunction in lipid metabolism was even more pronounced, featuring the upregulation of

genes implicated in fatty acid desaturation and the downregulation of several genes related to mitochondrial and peroxisomal β-oxidation. These findings suggest the involvement of multiple factors in lipid accumulation within microglia due to PGRN loss, including lysosomal dysfunction, exaggerated inflammation, and metabolic shifts in metabolism that favor increased fatty acid synthesis while suppressing β-oxidation. Interestingly, our transcriptomic analysis also shed light on the fact that PGRN loss results in the downregulation of OXPHOS genes in activated microglia. This disruption in energy metabolism may be linked to the observed decline in mitochondrial function within PGRN-deficient organoids, as elucidated in Chapter 2, and could indirectly contribute to increased lipid accumulation.

In addition to the well-established connection between PGRN mutations and FTD and NCL, PGRN has been linked to several other neurodegenerative conditions, including ALS, AD, and PD. However, how PGRN affects these diseases is unknown. Consequently, investigating the role of PGRN in various cell types within the central nervous system is of paramount importance. Our study provides offers insights into PGRN function, and further research holds the potential to address the limited therapeutic options for these devastating diseases.

REFERENCES

1. Nicholson AM, Gass J, Petrucelli L, Rademakers R. Progranulin axis and recent developments in frontotemporal lobar degeneration. Alzheimers Res Ther [Internet]. 2012 Jan 23;4(1):1–8. Available from: https://alzres.biomedcentral.com/articles/10.1186/alzrt102

2. Neumann M, Sampathu DM, Kwong LK, Truax AC, Micsenyi MC, Chou TT, et al. Ubiquitinated TDP-43 in frontotemporal lobar degeneration and amyotrophic lateral sclerosis. Science [Internet]. 2006;314(5796):130–3. Available from: http://dx.doi.org/10.1126/science.1134108

3. Wauters E, Van Mossevelde S, Van der Zee J, Cruts M, Van Broeckhoven C. Modifiers of GRN-Associated Frontotemporal Lobar Degeneration. Trends Mol Med [Internet]. 2017 Oct;23(10):962–79. Available from: http://dx.doi.org/10.1016/j.molmed.2017.08.004

4. Baker M, Mackenzie IR, Pickering-Brown SM, Gass J, Rademakers R, Lindholm C, et al. Mutations in progranulin cause tau-negative frontotemporal dementia linked to chromosome 17. Nature [Internet]. 2006 Jul 16;442. Available from: https://www.nature.com/articles/nature05016

5. Cruts M, Gijselinck I, Van Der Zee J, Engelborghs S, Wils H, Pirici D, et al. Null mutations in progranulin cause ubiquitin-positive frontotemporal dementia linked to chromosome 17q21. Nature 2006 442:7105 [Internet]. 2006 Jul 16;442(7105):920–4. Available from: http://dx.doi.org/10.1038/nature05017

6. Gass J, Cannon A, Mackenzie IR, Boeve B, Baker M, Adamson J, et al. Mutations in progranulin are a major cause of ubiquitin-positive frontotemporal lobar degeneration. Hum Mol Genet [Internet]. 2006 Oct 15;15(20):2988–3001. Available from: http://dx.doi.org/10.1093/hmg/ddl241

7. Arai T, Hasegawa M, Akiyama H, Ikeda K, Nonaka T, Mori H, et al. TDP-43 is a component of ubiquitin-positive tau-negative inclusions in frontotemporal lobar degeneration and amyotrophic lateral sclerosis. Biochem Biophys Res Commun [Internet]. 2006 Dec 22;351(3):602–11. Available from: http://dx.doi.org/10.1016/j.bbrc.2006.10.093

8. Gass J, Prudencio M, Stetler C, Petrucelli L. Progranulin: an emerging target for FTLD therapies. Brain Res [Internet]. 2012 Jun 26;1462:118–28. Available from: http://dx.doi.org/10.1016/j.brainres.2012.01.047

9. Rhinn H, Tatton N, McCaughey S, Kurnellas M, Rosenthal A. Progranulin as a therapeutic target in neurodegenerative diseases. Trends Pharmacol Sci [Internet]. 2022 Aug 1;43(8):641–52. Available from: http://www.cell.com/article/S0165614721002327/fulltext

10. van Swieten JC, Heutink P. Mutations in progranulin (GRN) within the spectrum of clinical and pathological phenotypes of frontotemporal dementia. Lancet Neurol [Internet]. 2008 Oct;7(10):965–74. Available from: http://dx.doi.org/10.1016/S1474-4422(08)70194-7

11. Smith KR, Damiano J, Franceschetti S, Carpenter S, Canafoglia L, Morbin M, et al. Strikingly different clinicopathological phenotypes determined by progranulin-mutation dosage. Am J Hum Genet [Internet]. 2012 Jun 8;90(6):1102–7. Available from: https://pubmed.ncbi.nlm.nih.gov/22608501/

12. Mole SE, Anderson G, Band HA, Berkovic SF, Cooper JD, Kleine Holthaus S-M, et al. Clinical challenges and future therapeutic approaches for neuronal ceroid lipofuscinosis. Lancet Neurol [Internet]. 2019 Jan;18(1):107–16. Available from: http://dx.doi.org/10.1016/S1474-4422(18)30368-5

13. Simonati A, Williams RE. Neuronal Ceroid Lipofuscinosis: The Multifaceted Approach to the Clinical Issues, an Overview. Front Neurol [Internet]. 2022 Mar 11;13:811686. Available from: http://dx.doi.org/10.3389/fneur.2022.811686

14. Huin V, Barbier M, Bottani A, Lobrinus JA, Clot F, Lamari F, et al. Homozygous GRN mutations: unexpected phenotypes and new insights into pathological and molecular mechanisms. Brain - A Journal of Neurology [Internet]. 2020 Jan 1;143(1):303–19. Available from: https://inserm.hal.science/inserm-03014481

15. Canafoglia L, Morbin M, Scaioli V, Pareyson D, D'Incerti L, Fugnanesi V, et al. Recurrent generalized seizures, visual loss, and palinopsia as phenotypic features of neuronal ceroid lipofuscinosis due to progranulin gene mutation. Epilepsia [Internet]. 2014 Jun;55(6):e56-9. Available from: http://dx.doi.org/10.1111/epi.12632

16. Almeida MR, Macário MC, Ramos L, Baldeiras I, Ribeiro MH, Santana I. Portuguese family with the co-occurrence of frontotemporal lobar degeneration and neuronal ceroid lipofuscinosis phenotypes due to progranulin gene mutation. Neurobiol Aging [Internet]. 2016 May;41:200.e1-200.e5. Available from: http://dx.doi.org/10.1016/j.neurobiolaging.2016.02.019

17. Kamate M, Detroja M, Hattiholi V. Neuronal ceroid lipofuscinosis type-11 in an adolescent. Brain Dev [Internet]. 2019 Jun;41(6):542–5. Available from: http://dx.doi.org/10.1016/j.braindev.2019.03.004

18. Götzl JK, Mori K, Damme M, Fellerer K, Tahirovic S, Kleinberger G, et al. Common pathobiochemical hallmarks of progranulin-associated frontotemporal lobar degeneration and neuronal ceroid lipofuscinosis. Acta Neuropathol [Internet]. 2014 Mar 12;127(6):845–60. Available from: https://link.springer.com/article/10.1007/s00401-014-1262-6

19. Ward ME, Chen R, Huang H-YY, Ludwig C, Telpoukhovskaia M, Taubes A, et al. Individuals with progranulin haploinsufficiency exhibit features of neuronal ceroid lipofuscinosis. Sci Transl Med [Internet]. 2017 Apr;9(385):1–11. Available from: http://stm.sciencemag.org/

20. Nalls MA, Blauwendraat C, Vallerga CL, Heilbron K, Bandres-Ciga S, Chang D, et al. Identification of novel risk loci, causal insights, and heritable risk for Parkinson's disease: a meta-genome wide association study. Lancet Neurol [Internet]. 2019 Dec 1;18(12):1091. Available from: https://www.ncbi.nlm.nih.gov/pmc/articles/PMC8422160/

21. van Blitterswijk M, Mullen B, Wojtas A, Heckman MG, Diehl NN, Baker MC, et al. Genetic modifiers in carriers of repeat expansions in the C9ORF72 gene. Mol Neurodegener [Internet]. 2014;9:38. Available from: https://www.ncbi.nlm.nih.gov/pmc/articles/PMC4190282/

22. Nag S, Schneider JA. Limbic-predominant age-related TDP43 encephalopathy (LATE) neuropathological change in neurodegenerative diseases. Nat Rev Neurol [Internet]. 2023 Sep;19(9):525–41. Available from: http://dx.doi.org/10.1038/s41582-023-00846-7

23. Bellenguez C, Küçükali F, Jansen IE, Kleineidam L, Moreno-Grau S, Amin N, et al. New insights into the genetic etiology of Alzheimer's disease and related dementias. Nat Genet [Internet]. 2022 Apr 1;54(4):412. Available from: https://www.ncbi.nlm.nih.gov/pmc/articles/PMC9005347/

24. Yin F, Banerjee R, Thomas B, Zhou P, Qian L, Jia T, et al. Exaggerated inflammation, impaired host defense, and neuropathology in progranulin-deficient mice. J Exp Med [Internet]. 2010 Jan 18;207(1):117–28. Available from: https://pubmed.ncbi.nlm.nih.gov/20026663/

25. Martens LH, Zhang J, Barmada SJ, Zhou P, Kamiya S, Sun B, et al. Progranulin deficiency promotes neuroinflammation and neuron loss following toxin-induced injury. J Clin Invest [Internet]. 2022 Jan 4;132(1). Available from: http://dx.doi.org/10.1172/JCI157161

26. Kayasuga Y, Chiba S, Suzuki M, Kikusui T, Matsuwaki T, Yamanouchi K, et al. Alteration of behavioural phenotype in mice by targeted disruption of the progranulin gene. Behav Brain Res [Internet]. 2007 Dec 28;185(2):110–8. Available from: http://dx.doi.org/10.1016/j.bbr.2007.07.020

27. Petkau TL, Neal SJ, Milnerwood A, Mew A, Hill AM, Orban P, et al. Synaptic dysfunction in progranulin-deficient mice. Neurobiol Dis [Internet]. 2012 Feb;45(2):711–22. Available from: http://dx.doi.org/10.1016/j.nbd.2011.10.016

28. Petkau TL, Life B, Lu G, Yang J, Fornes O, Wasserman W, et al. Human progranulin-expressing mice as a novel tool for the development of progranulin-modulating therapeutics. Neurobiol Dis [Internet]. 2021 Jun;153:105314. Available from: http://dx.doi.org/10.1016/j.nbd.2021.105314

29. Petkau TL, Hill A, Leavitt BR. Core neuropathological abnormalities in progranulin-deficient mice are penetrant on multiple genetic backgrounds. Neuroscience [Internet]. 2016 Feb 19;315:175–95. Available from: http://dx.doi.org/10.1016/j.neuroscience.2015.12.006

30. Ahmed Z, Sheng H, Xu Y-F, Lin W-L, Innes AE, Gass J, et al. Accelerated lipofuscinosis and ubiquitination in granulin knockout mice suggest a role for progranulin in successful aging. Am J Pathol [Internet]. 2010 Jul;177(1):311–24. Available from: https://pubmed.ncbi.nlm.nih.gov/20522652/

31. Zhang J, Velmeshev D, Hashimoto K, Huang YH, Hofmann JW, Shi X, et al. Neurotoxic microglia promote TDP-43 proteinopathy in progranulin deficiency. Nature [Internet]. 2020 Aug 31;588(7838):459–65. Available from: https://www.nature.com/articles/s41586-020-2709-7

32. Tanaka Y, Chambers JK, Matsuwaki T, Yamanouchi K, Nishihara M. Possible involvement of lysosomal dysfunction in pathological changes of the brain in aged progranulin-deficient mice. Acta Neuropathologica Communications [Internet]. 2014 Jan 27;2(1):1–15. Available from: https://actaneurocomms.biomedcentral.com/articles/10.1186/s40478-014-0078-x

33. Lui H, Zhang J, Makinson SR, Cahill MK, Kelley KW, Huang H-YY, et al. Progranulin Deficiency Promotes Circuit-Specific Synaptic Pruning by Microglia via Complement Activation. Cell [Internet]. 2016 May 5;165(4):921–35. Available from: http://dx.doi.org/10.1016/j.cell.2016.04.001

34. Bhandari V, Palfree RGE, Bateman A. Isolation and sequence of the granulin precursor cDNA from human bone marrow reveals tandem cysteine-rich granulin domains. Proceedings of the National Academy of Sciences [Internet]. 1992 Mar 1;89(5):1715–9. Available from: https://www.pnas.org/doi/abs/10.1073/pnas.89.5.1715

35. Holler CJ, Taylor G, Deng Q, Kukar T. Intracellular Proteolysis of Progranulin Generates Stable, Lysosomal Granulins that Are Haploinsufficient in Patients with Frontotemporal Dementia Caused by GRN Mutations. eNeuro [Internet]. 2017 Aug 18;4(4). Available from: http://dx.doi.org/10.1523/ENEURO.0100-17.2017

36. Palfree RGE, Bennett HPJ, Bateman A. The Evolution of the Secreted Regulatory Protein Progranulin. PLoS One [Internet]. 2015 Aug 6;10(8):e0133749. Available from: http://dx.doi.org/10.1371/journal.pone.0133749

37. Bateman A, Belcourt D, Bennett H, Lazure C, Solomon S. Granulins, a novel class of peptide from leukocytes. Biochem Biophys Res Commun [Internet]. 1990 Dec 31;173(3):1161–8. Available from: http://dx.doi.org/10.1016/s0006-291x(05)80908-8

38. Salazar DA, Butler VJ, Argouarch AR, Hsu T-Y, Mason A, Nakamura A, et al. The Progranulin Cleavage Products, Granulins, Exacerbate TDP-43 Toxicity and Increase TDP-43 Levels. J Neurosci [Internet]. 2015 Jun 24;35(25):9315–28. Available from: http://dx.doi.org/10.1523/JNEUROSCI.4808-14.2015

39. Mohan S, Sampognaro PJ, Argouarch AR, Maynard JC, Welch M, Patwardhan A, et al. Processing of progranulin into granulins involves multiple lysosomal proteases and is affected in frontotemporal lobar degeneration. Mol Neurodegener [Internet]. 2021 Aug 3;16(1):51. Available from: http://dx.doi.org/10.1186/s13024-021-00472-1

40. Kao AW, McKay A, Singh PP, Brunet A, Huang EJ. Progranulin, lysosomal regulation and neurodegenerative disease. Nature Publishing Group [Internet]. 2017 Jun 1;18(6):325–33. Available from: http://dx.doi.org/10.1038/nrn.2017.36

41. Almeida S, Zhou L, Gao F-B. Progranulin, a glycoprotein deficient in frontotemporal dementia, is a novel substrate of several protein disulfide isomerase family proteins. PLoS One [Internet]. 2011 Oct 18;6(10):e26454. Available from: http://dx.doi.org/10.1371/journal.pone.0026454

42. De Muynck L, Van Damme P. Cellular effects of progranulin in health and disease. J Mol Neurosci [Internet]. 2011 Nov;45(3):549–60. Available from: http://dx.doi.org/10.1007/s12031-011-9553-z

43. Hu F, Padukkavidana T, Vægter CB, Brady OA, Zheng Y, Mackenzie IR, et al. Sortilin-Mediated Endocytosis Determines Levels of the Frontotemporal Dementia Protein, Progranulin. Neuron [Internet]. 2010 Nov;68(4):654–67. Available from: http://www.sciencedirect.com/science/article/pii/S0896627310007762

44. Petoukhov E, Fernando S, Mills F, Shivji F, Hunter D, Krieger C, et al. Activity-dependent secretion of progranulin from synapses. J Cell Sci [Internet]. 2013 Dec 1;126(Pt 23):5412–21. Available from: http://dx.doi.org/10.1242/jcs.132076

45. Benussi L, Ciani M, Tonoli E, Morbin M, Palamara L, Albani D, et al. Loss of exosomes in progranulin-associated frontotemporal dementia. Neurobiol Aging [Internet]. 2016 Apr;40:41–9. Available from: http://dx.doi.org/10.1016/j.neurobiolaging.2016.01.001

46. Suh H-S, Choi N, Tarassishin L, Lee SC. Regulation of progranulin expression in human microglia and proteolysis of progranulin by matrix metalloproteinase-12 (MMP-12). PLoS One [Internet]. 2012 Apr 11;7(4):e35115. Available from: http://dx.doi.org/10.1371/journal.pone.0035115

47. Zhu J, Nathan C, Jin W, Sim D, Ashcroft GS, Wahl SM, et al. Conversion of proepithelin

to epithelins: roles of SLPI and elastase in host defense and wound repair. Cell [Internet]. 2002 Dec 13;111(6):867–78. Available from: http://dx.doi.org/10.1016/s0092-8674(02)01141-8

48. Kessenbrock K, Fröhlich L, Sixt M, Lämmermann T, Pfister H, Bateman A, et al. Proteinase 3 and neutrophil elastase enhance inflammation in mice by inactivating antiinflammatory progranulin. J Clin Invest [Internet]. 2008 Jul;118(7):2438–47. Available from: http://dx.doi.org/10.1172/JCI34694

49. Xu D, Suenaga N, Edelmann MJ, Fridman R, Muschel RJ, Kessler BM. Novel MMP-9 substrates in cancer cells revealed by a label-free quantitative proteomics approach. Mol Cell Proteomics [Internet]. 2008 Nov;7(11):2215–28. Available from: http://dx.doi.org/10.1074/mcp.M800095-MCP200

50. Butler GS, Dean RA, Tam EM, Overall CM. Pharmacoproteomics of a metalloproteinase hydroxamate inhibitor in breast cancer cells: dynamics of membrane type 1 matrix metalloproteinase-mediated membrane protein shedding. Mol Cell Biol [Internet]. 2008 Aug;28(15):4896–914. Available from: http://dx.doi.org/10.1128/MCB.01775-07

51. Bai X-H, Wang D-W, Kong L, Zhang Y, Luan Y, Kobayashi T, et al. ADAMTS-7, a direct target of PTHrP, adversely regulates endochondral bone growth by associating with and inactivating GEP growth factor. Mol Cell Biol [Internet]. 2009 Aug;29(15):4201–19. Available from: http://dx.doi.org/10.1128/MCB.00056-09

52. Zhou X, Sun L, de Oliveira FB, Qi X, Brown WJ, Smolka MB, et al. Prosaposin facilitates sortilin-independent lysosomal trafficking of progranulin. J Cell Biol [Internet]. 2015;210(6):991–1002. Available from: http://dx.doi.org/10.1083/jcb.201502029

53. Lee CW, Stankowski JN, Chew J, Cook CN, Lam Y-W, Almeida S, et al. The lysosomal protein cathepsin L is a progranulin protease. Mol Neurodegener [Internet]. 2017 Jul 25;12(1):55. Available from: http://dx.doi.org/10.1186/s13024-017-0196-6

54. Zhou X, Paushter DH, Feng T, Sun L, Reinheckel T, Hu F. Lysosomal processing of progranulin. 2017;1–6. Available from: http://dx.doi.org/10.1186/s13024-017-0205-9

55. Bateman A, Bennett HPJ. The granulin gene family: from cancer to dementia. Bioessays [Internet]. 2009 Nov;31(11):1245–54. Available from: http://onlinelibrary.wiley.com/doi/10.1002/bies.200900086/abstract

56. Jian J, Konopka J, Liu C. Insights into the role of progranulin in immunity, infection, and inflammation. J Leukoc Biol [Internet]. 2013 Feb;93(2):199–208. Available from: http://dx.doi.org/10.1189/jlb.0812429

57. He Z, Ong CHP, Halper J, Bateman A. Progranulin is a mediator of the wound response. Nat Med [Internet]. 2003 Feb;9(2):225–9. Available from: http://dx.doi.org/10.1038/nm816

58. He Z, Bateman A. Progranulin Gene Expression Regulates Epithelial Cell Growth and Promotes Tumor Growth in Vivo1. Cancer Res. 1999;59:3222–9.

59. Toh H, Cao M, Daniels E, Bateman A. Expression of the growth factor progranulin in endothelial cells influences growth and development of blood vessels: a novel mouse model. PLoS One [Internet]. 2013 May 31;8(5):e64989. Available from: http://dx.doi.org/10.1371/journal.pone.0064989

60. Toh H, Chitramuthu BP, Bennett HPJ, Bateman A. Structure, function, and mechanism of progranulin; the brain and beyond. J Mol Neurosci [Internet]. 2011 Nov;45(3):538–48. Available from: http://dx.doi.org/10.1007/s12031-011-9569-4

61. Brandes F, Borrmann M, Buschmann D, Meidert AS, Reithmair M, Langkamp M, et al. Progranulin signaling in sepsis, community-acquired bacterial pneumonia and COVID-19: a comparative, observational study. Intensive Care Med Exp [Internet]. 2021 Sep 3;9(1):43. Available from: http://dx.doi.org/10.1186/s40635-021-00406-7

62. Zou S, Luo Q, Song Z, Zhang L, Xia Y, Xu H, et al. Contribution of Progranulin to Protective Lung Immunity During Bacterial Pneumonia. J Infect Dis [Internet]. 2017 Jun 1;215(11):1764–73. Available from: http://dx.doi.org/10.1093/infdis/jix197

63. Tang W, Lu Y, Tian Q-Y, Zhang Y, Guo F-J, Liu G-Y, et al. The growth factor progranulin binds to TNF receptors and is therapeutic against inflammatory arthritis in mice. Science [Internet]. 2011 Apr 22;332(6028):478–84. Available from: http://dx.doi.org/10.1126/science.1199214

64. Okura H, Yamashita S, Ohama T, Saga A, Yamamoto-Kakuta A, Hamada Y, et al. HDL/apolipoprotein A-I binds to macrophage-derived progranulin and suppresses its conversion into proinflammatory granulins. J Atheroscler Thromb [Internet]. 2010 Jun 30;17(6):568–77. Available from: http://dx.doi.org/10.5551/jat.3921

65. Chitramuthu BP, Bennett HPJ, Bateman A. Progranulin: a new avenue towards the understanding and treatment of neurodegenerative disease. Brain [Internet]. 2017 Dec 1;140(12):3081–104. Available from: http://dx.doi.org/10.1093/brain/awx198

66. Bateman A, Cheung ST, Bennett HPJ. A Brief Overview of Progranulin in Health and Disease. In: Bateman A, Bennett HPJ, Cheung ST, editors. Progranulin: Methods and Protocols [Internet]. New York, NY: Springer New York; 2018. p. 3–15. Available from: https://doi.org/10.1007/978-1-4939-8559-3_1

67. Tanaka Y, Suzuki G, Matsuwaki T, Hosokawa M, Serrano G, Beach TG, et al. Progranulin regulates lysosomal function and biogenesis through acidification of lysosomes. Human Molecular Genetics [Internet]. 2017;26(5):969–88. Available from: http://dx.doi.org/10.1093/hmg/ddx011

68. Arrant AE, Roth JR, Boyle NR, Kashyap SN, Hoffmann MQ, Murchison CF, et al. Impaired

β-glucocerebrosidase activity and processing in frontotemporal dementia due to progranulin mutations. Acta Neuropathol Commun [Internet]. 2019 Dec 23;7(1):218. Available from: http://dx.doi.org/10.1186/s40478-019-0872-6

69. Logan T, Simon MJ, Rana A, Cherf GM, Srivastava A, Davis SS, et al. Rescue of a lysosomal storage disorder caused by Grn loss-of-function with a brain penetrant progranulin biologic. Cell [Internet]. 2021 Sep 9;184(18):4651. Available from: https://www.ncbi.nlm.nih.gov/pmc/articles/PMC8489356/

70. Valdez C, Ysselstein D, Young TJ, Zheng J, Krainc D. Progranulin mutations result in impaired processing of prosaposin and reduced glucocerebrosidase activity. Hum Mol Genet [Internet]. 2020 Mar 27;29(5):716–26. Available from: http://dx.doi.org/10.1093/hmg/ddz229

71. Beel S, Moisse M, Damme M, Muynck LD, Robberecht W, Van Den Bosch L, et al. Progranulin functions as a cathepsin D chaperone to stimulate axonal outgrowth in vivo. 2017;26(15):2850–63. Available from: http://dx.doi.org/10.1093/hmg/ddx162

72. Valdez C, Wong YC, Schwake M, Bu G, Wszolek ZK, Krainc D. Progranulin-mediated deficiency of cathepsin D results in FTD and NCL-like phenotypes in neurons derived from FTD patients. Hum Mol Genet [Internet]. 2017 Dec;26(24):4861–72. Available from: https://dx.doi.org/10.1093/hmg/ddx364

73. Evers BM, Rodriguez-Navas C, Tesla RJ, Prange-Kiel J, Wasser CR, Yoo KS, et al. Lipidomic and Transcriptomic Basis of Lysosomal Dysfunction in Progranulin Deficiency. Cell Rep [Internet]. 2017;20(11):2565–74. Available from: http://dx.doi.org/10.1016/j.celrep.2017.08.056

74. Tanaka Y, Matsuwaki T, Yamanouchi K, Nishihara M. INCREASED LYSOSOMAL BIOGENESIS IN ACTIVATED MICROGLIA AND EXACERBATED NEURONAL DAMAGE AFTER TRAUMATIC BRAIN INJURY IN PROGRANULIN-DEFICIENT MICE. Neuroscience [Internet]. 2013;250:8–19. Available from: http://dx.doi.org/10.1016/j.neuroscience.2013.06.049

75. Roberson ED, Filiano AJ, Martens LH, Young AH, Warmus BA, Zhou P, et al. Dissociation of Frontotemporal Dementia–Related Deficits and Neuroinflammation in Progranulin Haploinsufficient Mice. J Neurosci [Internet]. 2013 Mar 3;33(12):5352. Available from: https://www.ncbi.nlm.nih.gov/pmc/articles/PMC3740510/

76. Matsuwaki T, Asakura R, Suzuki M, Yamanouchi K, Nishihara M. Age-dependent changes in progranulin expression in the mouse brain. J Reprod Dev [Internet]. 2011 Feb;57(1):113–9. Available from: http://dx.doi.org/10.1262/jrd.10-116s

77. Daniel R, He Z, Carmichael KP, Halper J, Bateman A. Cellular localization of gene expression for progranulin. J Histochem Cytochem [Internet]. 2000 Jul;48(7):999–1009.

Available from: http://dx.doi.org/10.1177/002215540004800713

78. Lü L, Luo L, Lu Y, Chen L, Xu J, Guo K. Progranulin expression in neural stem cells and their differentiated cell lineages: An immunocytochemical study. Mol Med Rep [Internet]. 2013 Nov;8(5):1359–64. Available from: https://www.spandidos-publications.com/10.3892/mmr.2013.1664

79. Petkau TL, Neal S j., Orban P c., MacDonald J l., Hill A m., Lu G, et al. Progranulin expression in the developing and adult murine brain. J Comp Neurol [Internet]. 2010 Oct;518(19):3931–47. Available from: http://onlinelibrary.wiley.com/doi/10.1002/cne.22430/abstract

80. Kuse Y, Tsuruma K, Mizoguchi T, Shimazawa M, Hara H. Progranulin deficiency causes the retinal ganglion cell loss during development. Sci Rep [Internet]. 2017 May 10;7(1):1679. Available from: http://dx.doi.org/10.1038/s41598-017-01933-8

81. Gao X, Joselin AP, Wang L, Kar A, Ray P, Bateman A, et al. Progranulin promotes neurite outgrowth and neuronal differentiation by regulating GSK-3β. Protein Cell [Internet]. 2010 Jun;1(6):552–62. Available from: http://dx.doi.org/10.1007/s13238-010-0067-1

82. Van Damme P, Van Hoecke A, Lambrechts D, Vanacker P, Bogaert E, van Swieten J, et al. Progranulin functions as a neurotrophic factor to regulate neurite outgrowth and enhance neuronal survival. J Cell Biol [Internet]. 2008 Apr 7;181(1):37–41. Available from: http://dx.doi.org/10.1083/jcb.200712039

83. Gass J, Lee WC, Cook C, Finch N, Stetler C, Jansen-West K, et al. Progranulin regulates neuronal outgrowth independent of sortilin. Mol Neurodegener [Internet]. 2012 Jul 10;7:33. Available from: http://dx.doi.org/10.1186/1750-1326-7-33

84. Kleinberger G, Wils H, Ponsaerts P, Joris G, Timmermans J-P, Van Broeckhoven C, et al. Increased caspase activation and decreased TDP-43 solubility in progranulin knockout cortical cultures. J Neurochem [Internet]. 2010 Nov;115(3):735–47. Available from: http://dx.doi.org/10.1111/j.1471-4159.2010.06961.x

85. Kim J-Y, Kim DH, Kim JH, Yang YS, Oh W, Lee EH, et al. Umbilical cord blood mesenchymal stem cells protect amyloid-β42 neurotoxicity via paracrine. World J Stem Cells [Internet]. 2012 Nov 26;4(11):110–6. Available from: http://dx.doi.org/10.4252/wjsc.v4.i11.110

86. Almeida S, Zhang Z, Coppola G, Mao W, Futai K, Karydas A, et al. Induced Pluripotent Stem Cell Models of Progranulin-Deficient Frontotemporal Dementia Uncover Specific Reversible Neuronal Defects. Cell Rep [Internet]. 2012 Oct;2(4):789–98. Available from: http://www.ncbi.nlm.nih.gov/pmc/articles/PMC3532907/

87. Guo A, Tapia L, Bamji SX, Cynader MS, Jia W. Progranulin deficiency leads to enhanced cell vulnerability and TDP-43 translocation in primary neuronal cultures. Brain Res

[Internet]. 2010 Dec 17;1366:1–8. Available from: http://dx.doi.org/10.1016/j.brainres.2010.09.099

88. Xu J, Xilouri M, Bruban J, Shioi J, Shao Z, Papazoglou I, et al. Extracellular progranulin protects cortical neurons from toxic insults by activating survival signaling. Neurobiol Aging [Internet]. 2011 Dec 1;32(12):2326.e5-2326.e16. Available from: http://dx.doi.org/10.1016/J.NEUROBIOLAGING.2011.06.017

89. Davis SE, Roth JR, Aljabi Q, Hakim AR, Savell KE, Day JJ, et al. Delivering progranulin to neuronal lysosomes protects against excitotoxicity. J Biol Chem [Internet]. 2021 Sep;297(3):100993. Available from: http://dx.doi.org/10.1016/j.jbc.2021.100993

90. De Muynck L, Herdewyn S, Beel S, Scheveneels W, Van Den Bosch L, Robberecht W, et al. The neurotrophic properties of progranulin depend on the granulin E domain but do not require sortilin binding. Neurobiol Aging [Internet]. 2013 Nov;34(11):2541–7. Available from: http://dx.doi.org/10.1016/j.neurobiolaging.2013.04.022

91. Neill T, Buraschi S, Goyal A, Sharpe C, Natkanski E, Schaefer L, et al. EphA2 is a functional receptor for the growth factor progranulin. J Cell Biol [Internet]. 2016 Dec 5;215(5):687–703. Available from: http://dx.doi.org/10.1083/jcb.201603079

92. Tapia L, Milnerwood A, Guo A, Mills F, Yoshida E, Vasuta C, et al. Progranulin Deficiency Decreases Gross Neural Connectivity But Enhances Transmission at Individual Synapses. J Neurosci [Internet]. 2011 Aug;31(31):11126–32. Available from: http://www.jneurosci.org/content/31/31/11126

93. Tanaka Y, Matsuwaki T, Yamanouchi K, Nishihara M. Exacerbated inflammatory responses related to activated microglia after traumatic brain injury in progranulin-deficient mice. Neuroscience [Internet]. 2013 Feb 12;231:49–60. Available from: http://dx.doi.org/10.1016/j.neuroscience.2012.11.032

94. Naphade SB, Kigerl KA, Jakeman LB, Kostyk SK, Popovich PG, Kuret J. Progranulin expression is upregulated after spinal contusion in mice. Acta Neuropathol [Internet]. 2010 Jan;119(1):123–33. Available from: http://dx.doi.org/10.1007/s00401-009-0616-y

95. Moisse K, Volkening K, Leystra-Lantz C, Welch I, Hill T, Strong MJ. Divergent patterns of cytosolic TDP-43 and neuronal progranulin expression following axotomy: Implications for TDP-43 in the physiological response to neuronal injury [Internet]. Brain Research Jan, 2009 p. 202–11. Available from: http://www.sciencedirect.com/science/article/pii/S0006899308025110

96. Ohmi K, Greenberg DS, Rajavel KS, Ryazantsev S, Li HH, Neufeld EF. Activated microglia in cortex of mouse models of mucopolysaccharidoses I and IIIB. Proc Natl Acad Sci U S A [Internet]. 2003 Feb 18;100(4):1902–7. Available from: http://dx.doi.org/10.1073/pnas.252784899

97. Mendsaikhan A, Tooyama I, Walker DG. Microglial Progranulin: Involvement in Alzheimer's Disease and Neurodegenerative Diseases. Cells 2019, Vol 8, Page 230 [Internet]. 2019 Mar 11;8(3):230. Available from: https://www.mdpi.com/2073-4409/8/3/230/htm

98. Philips T, De Muynck L, Thu HNT, Weynants B, Vanacker P, Dhondt J, et al. Microglial upregulation of progranulin as a marker of motor neuron degeneration. J Neuropathol Exp Neurol [Internet]. 2010 Dec;69(12):1191–200. Available from: http://dx.doi.org/10.1097/NEN.0b013e3181fc9aea

99. Ahmed Z, Mackenzie IRA, Hutton ML, Dickson DW. Progranulin in frontotemporal lobar degeneration and neuroinflammation. J Neuroinflammation [Internet]. 2007 Feb;4:7. Available from: http://www.ncbi.nlm.nih.gov/pmc/articles/PMC1805428/

100. Pickford F, Marcus J, Camargo LM, Xiao Q, Graham D, Mo J-R, et al. Progranulin is a chemoattractant for microglia and stimulates their endocytic activity. Am J Pathol [Internet]. 2011 Jan;178(1):284–95. Available from: http://dx.doi.org/10.1016/j.ajpath.2010.11.002

101. Tian Q, Zhao Y, Mundra JJ, Gonzalez-Gugel E, Jian J, Uddin SMZ, et al. Three TNFR-binding domains of PGRN act independently in inhibition of TNF-alpha binding and activity. Front Biosci [Internet]. 2014 Jun 1;19(7):1176–85. Available from: http://dx.doi.org/10.2741/4274

102. Chen X, Chang J, Deng Q, Xu J, Nguyen TA, Martens LH, et al. Progranulin does not bind tumor necrosis factor (TNF) receptors and is not a direct regulator of TNF-dependent signaling or bioactivity in immune or neuronal cells. J Neurosci [Internet]. 2013 May 22;33(21):9202–13. Available from: http://dx.doi.org/10.1523/JNEUROSCI.5336-12.2013

103. Lang I, Füllsack S, Wajant H. Lack of Evidence for a Direct Interaction of Progranulin and Tumor Necrosis Factor Receptor-1 and Tumor Necrosis Factor Receptor-2 From Cellular Binding Studies. Front Immunol [Internet]. 2018 Apr 23;9:793. Available from: http://dx.doi.org/10.3389/fimmu.2018.00793

104. Park B, Buti L, Lee S, Matsuwaki T, Spooner E, Brinkmann MM, et al. Granulin is a soluble cofactor for toll-like receptor 9 signaling. Immunity [Internet]. 2011 Apr 22;34(4):505–13. Available from: http://dx.doi.org/10.1016/j.immuni.2011.01.018

105. Moresco EMY, Beutler B. Special delivery: granulin brings CpG DNA to Toll-like receptor 9. Immunity [Internet]. 2011 Apr 22;34(4):453–5. Available from: http://dx.doi.org/10.1016/j.immuni.2011.04.001

106. Minami SS, Min SW, Krabbe G, Wang C, Zhou Y, Asgarov R, et al. Progranulin Protects against Amyloid β Deposition and Toxicity in Alzheimer's Disease Mouse Models.

Nature medicine [Internet]. 2014 Oct 1;20(10):1157. Available from: http://dx.doi.org/10.1038/NM.3672

107. Marschallinger J, Iram T, Zardeneta M, Lee SE, Lehallier B, Haney MS, et al. Lipid-droplet-accumulating microglia represent a dysfunctional and proinflammatory state in the aging brain. Nat Neurosci [Internet]. 2020 Feb 1;23(2):194–208. Available from: https://doi.org/10.1038/s41593-019-0566-1

108. Kao AW, Eisenhut RJ, Martens LH, Nakamura A, Huang A, Bagley JA, et al. A neurodegenerative disease mutation that accelerates the clearance of apoptotic cells. Proc Natl Acad Sci U S A [Internet]. 2011 Mar 15;108(11):4441–6. Available from: https://www.ncbi.nlm.nih.gov/pmc/articles/PMC3060230/

109. Tao J, Ji F, Wang F, Liu B, Zhu Y. Neuroprotective effects of progranulin in ischemic mice. Brain Res [Internet]. 2012 Feb 3;1436:130–6. Available from: http://dx.doi.org/10.1016/j.brainres.2011.11.063

110. Menzel L, Kleber L, Friedrich C, Hummel R, Dangel L, Winter J, et al. Progranulin protects against exaggerated axonal injury and astrogliosis following traumatic brain injury. Glia [Internet]. 2017 Feb;65(2):278–92. Available from: http://dx.doi.org/10.1002/glia.23091

111. Marsan E, Velmeshev D, Ramsey A, Patel RK, Zhang J, Koontz M, et al. Astroglial toxicity promotes synaptic degeneration in the thalamocortical circuit in frontotemporal dementia with GRN mutations. J Clin Invest [Internet]. 2023 Mar 15;133(6). Available from: http://dx.doi.org/10.1172/JCI164919

112. Liddelow SA, Guttenplan KA, Clarke LE, Bennett FC, Bohlen CJ, Schirmer L, et al. Neurotoxic reactive astrocytes are induced by activated microglia. Nature [Internet]. 2017 Jan 26;541(7638):481–7. Available from: http://dx.doi.org/10.1038/nature21029

113. Tanaka Y, Cakir B, Xiang Y, Sullivan GJ, Park IH. Synthetic Analyses of Single-Cell Transcriptomes from Multiple Brain Organoids and Fetal Brain. Cell Rep [Internet]. 2020 Feb 11;30(6):1682-1689.e3. Available from: http://dx.doi.org/10.1016/J.CELREP.2020.01.038

114. Sloan SA, Andersen J, Paşca AM, Birey F, Paşca SP. Generation and assembly of human brain region–specific three-dimensional cultures. Nat Protoc [Internet]. 2018 Sep 1;13(9):2062–85. Available from: https://doi.org/10.1038/s41596-018-0032-7

115. de Majo M, Koontz M, Marsan E, Salinas N, Ramsey A, Kuo YM, et al. Granulin loss of function in human mature brain organoids implicates astrocytes in TDP-43 pathology. Stem Cell Reports [Internet]. 2023 Mar 3;18(3):706. Available from: https://www.ncbi.nlm.nih.gov/pmc/articles/PMC10031303/

116. Bossolasco P, Cimini S, Maderna E, Bardelli D, Canafoglia L, Cavallaro T, et al. GRN−/−

iPSC-derived cortical neurons recapitulate the pathological findings of both frontotemporal lobar degeneration and neuronal ceroidolipofuscinosis. Neurobiol Dis [Internet]. 2022 Dec 1;175:105891. Available from: http://dx.doi.org/10.1016/J.NBD.2022.105891

117. Petkau TL, Kosior N, de Asis K, Connolly C, Leavitt BR. Selective depletion of microglial progranulin in mice is not sufficient to cause neuronal ceroid lipofuscinosis or neuroinflammation. J Neuroinflammation [Internet]. 2017 Nov 17;14(1):1–11. Available from: https://jneuroinflammation.biomedcentral.com/articles/10.1186/s12974-017-1000-9

118. Petkau TL, Blanco J, Leavitt BR. Conditional loss of progranulin in neurons is not sufficient to cause neuronal ceroid lipofuscinosis-like neuropathology in mice. Neurobiol Dis [Internet]. 2017 Oct;106:14–22. Available from: http://dx.doi.org/10.1016/j.nbd.2017.06.012

119. Lee C, Frew J, Weilinger NL, Wendt S, Cai W, Sorrentino S, et al. hiPSC-derived GRN-deficient astrocytes delay spiking activity of developing neurons. Neurobiol Dis [Internet]. 2023 Jun 1;181:106124. Available from: http://dx.doi.org/10.1016/J.NBD.2023.106124

120. Yoon SJ, Elahi LS, Pașca AM, Marton RM, Gordon A, Revah O, et al. Reliability of human cortical organoid generation. Nat Methods [Internet]. 2019;16(1):75–8. Available from: http://dx.doi.org/10.1038/s41592-018-0255-0

121. Hippen AA, Falco MM, Weber LM, Erkan EP, Zhang K, Doherty JA, et al. miQC: An adaptive probabilistic framework for quality control of single-cell RNA-sequencing data. PLoS Comput Biol [Internet]. 2021 Aug 1;17(8):e1009290. Available from: https://journals.plos.org/ploscompbiol/article?id=10.1371/journal.pcbi.1009290

122. Franzén O, Gan LM, Björkegren JLM. PanglaoDB: a web server for exploration of mouse and human single-cell RNA sequencing data. Database [Internet]. 2019 Jan 1;2019(1). Available from: https://dx.doi.org/10.1093/database/baz046

123. Chen EY, Tan CM, Kou Y, Duan Q, Wang Z, Meirelles GV, et al. Enrichr: Interactive and collaborative HTML5 gene list enrichment analysis tool. BMC Bioinformatics [Internet]. 2013 Apr 15;14(1):1–14. Available from: https://bmcbioinformatics.biomedcentral.com/articles/10.1186/1471-2105-14-128

124. Vértesy Á, Eichmüller OL, Naas J, Novatchkova M, Esk C, Balmaña M, et al. Gruffi: an algorithm for computational removal of stressed cells from brain organoid transcriptomic datasets. EMBO J [Internet]. 2022 Sep 1;41(17):e111118. Available from: https://onlinelibrary.wiley.com/doi/full/10.15252/embj.2022111118

125. Glasauer SMK, Goderie SK, Rauch JN, Guzman E, Audouard M, Bertucci T, et al. Human

tau mutations in cerebral organoids induce a progressive dyshomeostasis of cholesterol. Stem Cell Reports [Internet]. 2022 Sep 9;17(9):2127. Available from: https://www.ncbi.nlm.nih.gov/pmc/articles/PMC9481908/

126. Nowakowski TJ, Bhaduri A, Pollen AA, Alvarado B, Mostajo-Radji MA, Di Lullo E, et al. Spatiotemporal gene expression trajectories reveal developmental hierarchies of the human cortex. Science [Internet]. 2017 Dec 8;358(6368):1318–23. Available from: https://www.science.org/doi/10.1126/science.aap8809

127. Zhou Y, Zhou B, Pache L, Chang M, Khodabakhshi AH, Tanaseichuk O, et al. Metascape provides a biologist-oriented resource for the analysis of systems-level datasets. Nat Commun [Internet]. 2019 Apr 3;10(1):1523. Available from: http://dx.doi.org/10.1038/s41467-019-09234-6

128. Smeitink J, Van Den Heuvel L, DiMauro S. The genetics and pathology of oxidative phosphorylation. Nature Reviews Genetics 2001 2:5 [Internet]. 2001 May;2(5):342–52. Available from: https://www.nature.com/articles/35072063

129. Tanaka Y, Ito S-I, Honma Y, Hasegawa M, Kametani F, Suzuki G, et al. Dysregulation of the progranulin-driven autophagy-lysosomal pathway mediates secretion of the nuclear protein TDP-43. J Biol Chem [Internet]. 2023 Nov;299(11):105272. Available from: http://dx.doi.org/10.1016/j.jbc.2023.105272

130. Chang MC, Srinivasan K, Friedman BA, Suto E, Modrusan Z, Lee WP, et al. Progranulin deficiency causes impairment of autophagy and TDP-43 accumulation. J Exp Med [Internet]. 2017 Sep 9;214(9):2611–28. Available from: https://www.ncbi.nlm.nih.gov/pmc/articles/PMC5584112/

131. Rodríguez-Periñán G, de la Encarnación A, Moreno F, López de Munain A, Martínez A, Martín-Requero Á, et al. Progranulin Deficiency Induces Mitochondrial Dysfunction in Frontotemporal Lobar Degeneration with TDP-43 Inclusions. Antioxid Redox Signal [Internet]. 2023;12(3). Available from: http://dx.doi.org/10.3390/antiox12030581

132. Casey JM, Melandri D, Arber C, Soutar M, Holler CJ, Kukar T, et al. Haploinsufficiency of progranulin causes cell type specific impairments in PINK1/Parkin mitophagy. Alzheimers Dement [Internet]. 2023 Jun;19(S1):e064195. Available from: https://onlinelibrary.wiley.com/doi/full/10.1002/alz.064195

133. Zhou D, Zhou M, Wang Z, Fu Y, Jia M, Wang X, et al. PGRN acts as a novel regulator of mitochondrial homeostasis by facilitating mitophagy and mitochondrial biogenesis to prevent podocyte injury in diabetic nephropathy. Cell Death & Disease 2019 10:7 [Internet]. 2019 Jul 8;10(7):1–16. Available from: https://www.nature.com/articles/s41419-019-1754-3

134. Zhao T, Zhu Y, Morinibu A, Kobayashi M, Shinomiya K, Itasaka S, et al. HIF-1-mediated

metabolic reprogramming reduces ROS levels and facilitates the metastatic colonization of cancers in lungs. Scientific Reports 2014 4:1 [Internet]. 2014 Jan 23;4(1):1–7. Available from: https://www.nature.com/articles/srep03793

135. Li HS, Zhou YN, Li L, Li SF, Long D, Chen XL, et al. HIF-1α protects against oxidative stress by directly targeting mitochondria. Redox Biology [Internet]. 2019 Jul 1;25:101109. Available from: https://www.ncbi.nlm.nih.gov/pmc/articles/PMC6859547/

136. Taylor CT, Scholz CC. The effect of HIF on metabolism and immunity. Nature Reviews Nephrology 2022 18:9 [Internet]. 2022 Jun 20;18(9):573–87. Available from: https://www.nature.com/articles/s41581-022-00587-8

137. Bolaños JP. Bioenergetics and redox adaptations of astrocytes to neuronal activity. J Neurochem [Internet]. 2016 Oct 1;139:115–25. Available from: https://onlinelibrary.wiley.com/doi/full/10.1111/jnc.13486

138. Arimoto-Matsuzaki K, Saito H, Takekawa M. TIA1 oxidation inhibits stress granule assembly and sensitizes cells to stress-induced apoptosis. Nature Communications 2016 7:1 [Internet]. 2016 Jan 7;7(1):1–10. Available from: https://www.nature.com/articles/ncomms10252

139. Divakaruni AS, Jastroch M. A practical guide for the analysis, standardization and interpretation of oxygen consumption measurements. Nature Metabolism 2022 4:8 [Internet]. 2022 Aug 15;4(8):978–94. Available from: https://www.nature.com/articles/s42255-022-00619-4

140. Balaban RS, Nemoto S, Finkel T. Mitochondria, Oxidants, and Aging. Cell [Internet]. 2005 Feb 25;120(4):483–95. Available from: http://dx.doi.org/10.1016/J.CELL.2005.02.001

141. Yin D. Biochemical basis of lipofuscin, ceroid, and age pigment-like fluorophores. Free Radical Biology and Medicine [Internet]. 1996 Jan 1;21(6):871–88. Available from: http://dx.doi.org/10.1016/0891-5849(96)00175-X

142. Anderson GW, Goebel HH, Simonati A. Human pathology in NCL. Biochimica et Biophysica Acta (BBA) - Molecular Basis of Disease [Internet]. 2013 Nov 1;1832(11):1807–26. Available from: http://dx.doi.org/10.1016/J.BBADIS.2012.11.014

143. Moreno-García A, Kun A, Calero O, Medina M, Calero M. An overview of the role of lipofuscin in age-related neurodegeneration. Front Neurosci [Internet]. 2018 Jul 5;12(JUL):352489. Available from: http://dx.doi.org/10.3389/FNINS.2018.00464/BIBTEX

144. Weiss RH, Estabrook RW. The mechanism of cumene hydroperoxide-dependent lipid peroxidation: The significance of oxygen uptake. Arch Biochem Biophys [Internet].

1986 Nov 15;251(1):336–47. Available from: http://dx.doi.org/10.1016/0003-9861(86)90081-0

145. Dixon SJ, Lemberg KM, Lamprecht MR, Skouta R, Zaitsev EM, Gleason CE, et al. Ferroptosis: An Iron-Dependent Form of Nonapoptotic Cell Death. Cell [Internet]. 2012 May 25;149(5):1060–72. Available from: http://dx.doi.org/10.1016/J.CELL.2012.03.042

146. Yang WS, Sriramaratnam R, Welsch ME, Shimada K, Skouta R, Viswanathan VS, et al. Regulation of Ferroptotic Cancer Cell Death by GPX4. Cell [Internet]. 2014 Jan 16;156(1–2):317–31. Available from: http://dx.doi.org/10.1016/J.CELL.2013.12.010

147. Stockwell BR, Friedmann Angeli JP, Bayir H, Bush AI, Conrad M, Dixon SJ, et al. Ferroptosis: A Regulated Cell Death Nexus Linking Metabolism, Redox Biology, and Disease. Cell [Internet]. 2017 Oct 5;171(2):273–85. Available from: http://dx.doi.org/10.1016/J.CELL.2017.09.021

148. Zhou N, Yuan X, Du Q, Zhang Z, Shi X, Bao J, et al. FerrDb V2: update of the manually curated database of ferroptosis regulators and ferroptosis-disease associations. Nucleic Acids Res [Internet]. 2023 Jan 1;51(D1):D571. Available from: https://www.ncbi.nlm.nih.gov/pmc/articles/PMC9825716/

149. Yang Y, Tetti M, Vohra T, Adolf C, Seissler J, Hristov M, et al. BEX1 Is Differentially Expressed in Aldosterone-Producing Adenomas and Protects Human Adrenocortical Cells from Ferroptosis. Hypertension [Internet]. 2021 May 1;77(5):1647–58. Available from: https://www.ahajournals.org/doi/abs/10.1161/HYPERTENSIONAHA.120.16774

150. Lu J, Holmgren A. The thioredoxin antioxidant system. Free Radical Biology and Medicine [Internet]. 2014 Jan 8;66:75–87. Available from: http://dx.doi.org/10.1016/J.FREERADBIOMED.2013.07.036

151. Llabani E, Hicklin RW, Lee HY, Motika SE, Crawford LA, Weerapana E, et al. Diverse compounds from pleuromutilin lead to a thioredoxin inhibitor and inducer of ferroptosis. Nature Chemistry 2019 11:6 [Internet]. 2019 May 13;11(6):521–32. Available from: https://www.nature.com/articles/s41557-019-0261-6

152. Bai L, Yan F, Deng R, Gu R, Zhang X, Bai J. Thioredoxin-1 Rescues MPP+/MPTP-Induced Ferroptosis by Increasing Glutathione Peroxidase 4. 2021 Jul 1;58(7):3187–97. Available from: https://pubmed.ncbi.nlm.nih.gov/33634378/

153. Yang WS, Stockwell BR. Synthetic Lethal Screening Identifies Compounds Activating Iron-Dependent, Nonapoptotic Cell Death in Oncogenic-RAS-Harboring Cancer Cells. Chem Biol [Internet]. 2008 Mar 21;15(3):234–45. Available from: http://dx.doi.org/10.1016/J.CHEMBIOL.2008.02.010

154. Hou W, Xie Y, Song X, Sun X, Lotze MT, Zeh HJ, et al. Autophagy promotes ferroptosis by degradation of ferritin. Autophagy [Internet]. 2016 Aug 2;12(8):1425–8. Available

from: https://www.tandfonline.com/doi/abs/10.1080/15548627.2016.1187366

155. Du J, Wang T, Li Y, Zhou Y, Wang X, Yu X, et al. DHA inhibits proliferation and induces ferroptosis of leukemia cells through autophagy dependent degradation of ferritin. Free Radical Biology and Medicine [Internet]. 2019 Feb 1;131:356–69. Available from: http://dx.doi.org/10.1016/J.FREERADBIOMED.2018.12.011

156. Liu J, Ren Z, Yang L, Zhu L, Li Y, Bie C, et al. The NSUN5-FTH1/FTL pathway mediates ferroptosis in bone marrow-derived mesenchymal stem cells. Cell Death Discovery 2022 8:1 [Internet]. 2022 Mar 5;8(1):1–11. Available from: https://www.nature.com/articles/s41420-022-00902-z

157. Kim EH, Shin D, Lee J, Jung AR, Roh JL. CISD2 inhibition overcomes resistance to sulfasalazine-induced ferroptotic cell death in head and neck cancer. Cancer Lett [Internet]. 2018 Sep 28;432:180–90. Available from: http://dx.doi.org/10.1016/J.CANLET.2018.06.018

158. Yuan H, Li X, Zhang X, Kang R, Tang D. CISD1 inhibits ferroptosis by protection against mitochondrial lipid peroxidation. Biochem Biophys Res Commun [Internet]. 2016 Sep 16;478(2):838–44. Available from: http://dx.doi.org/10.1016/J.BBRC.2016.08.034

159. Chen X, Yu C, Kang R, Tang D. Iron Metabolism in Ferroptosis. Frontiers in Cell and Developmental Biology [Internet]. 2020 Oct 7;8. Available from: https://www.ncbi.nlm.nih.gov/pmc/articles/PMC7575751/

160. Tang D, Chen X, Kang R, Kroemer G. Ferroptosis: molecular mechanisms and health implications. Cell Research 2020 31:2 [Internet]. 2020 Dec 2;31(2):107–25. Available from: https://www.nature.com/articles/s41422-020-00441-1

161. Zhang S, Xin W, Anderson GJ, Li R, Gao L, Chen S, et al. Double-edge sword roles of iron in driving energy production versus instigating ferroptosis. Cell Death & Disease 2021 13:1 [Internet]. 2022 Jan 10;13(1):1–13. Available from: https://www.nature.com/articles/s41419-021-04490-1

162. Swerdlow RH. Mitochondria and Mitochondrial Cascades in Alzheimer's Disease. J Alzheimers Dis [Internet]. 2018;62(3):1403. Available from: https://www.ncbi.nlm.nih.gov/pmc/articles/PMC5869994/

163. Schapira AHV. Mitochondrial dysfunction in Parkinson's disease. Cell Death Differ [Internet]. 2007 Jul;14(7):1261–6. Available from: http://dx.doi.org/10.1038/SJ.CDD.4402160

164. Muyderman H, Chen T. Mitochondrial dysfunction in amyotrophic lateral sclerosis – a valid pharmacological target? Br J Pharmacol [Internet]. 2014;171(8):2191. Available from: https://www.ncbi.nlm.nih.gov/pmc/articles/PMC3976630/

165. Bakare AB, Lesnefsky EJ, Iyer S. Leigh Syndrome: A Tale of Two Genomes. Front Physiol [Internet]. 2021 Aug 11;12. Available from: https://www.ncbi.nlm.nih.gov/pmc/articles/PMC8385445/

166. Das AM, Jolly RD, Kohlschütter A. Anomalies of mitochondrial ATP synthase regulation in four different types of neuronal ceroid lipofuscinosis. Mol Genet Metab [Internet]. 1999;66(4):349–55. Available from: https://pubmed.ncbi.nlm.nih.gov/10191128/

167. Pezzini F, Gismondi F, Tessa A, Tonin P, Carrozzo R, Mole SE, et al. Involvement of the mitochondrial compartment in human NCL fibroblasts. Biochem Biophys Res Commun [Internet]. 2011 Dec 9;416(1–2):159–64. Available from: http://dx.doi.org/10.1016/J.BBRC.2011.11.016

168. Doccini S, Morani F, Nesti C, Pezzini F, Calza G, Soliymani R, et al. Proteomic and functional analyses in disease models reveal CLN5 protein involvement in mitochondrial dysfunction. Cell Death Discovery [Internet]. 2020 Dec 1;6(1). Available from: https://www.ncbi.nlm.nih.gov/pmc/articles/PMC7105465/

169. Luiro K, Kopra O, Blom T, Gentile M, Mitchison HM, Hovatta I, et al. Batten disease (JNCL) is linked to disturbances in mitochondrial, cytoskeletal, and synaptic compartments. J Neurosci Res [Internet]. 2006 Oct 1;84(5):1124–38. Available from: https://onlinelibrary.wiley.com/doi/full/10.1002/jnr.21015

170. Miedema SSM, Mol MO, Koopmans FTW, Hondius DC, van Nierop P, Menden K, et al. Distinct cell type-specific protein signatures in GRN and MAPT genetic subtypes of frontotemporal dementia. Acta Neuropathologica Communications [Internet]. 2022 Dec 1;10(1):1–20. Available from: https://actaneurocomms.biomedcentral.com/articles/10.1186/s40478-022-01387-8

171. Huang M, Modeste E, Dammer E, Merino P, Taylor G, Duong DM, et al. Network analysis of the progranulin-deficient mouse brain proteome reveals pathogenic mechanisms shared in human frontotemporal dementia caused by GRN mutations. Acta Neuropathologica Communications 2020 8:1 [Internet]. 2020 Oct 7;8(1):1–25. Available from: https://actaneurocomms.biomedcentral.com/articles/10.1186/s40478-020-01037-x

172. Rosen EY, Wexler EM, Versano R, Coppola G, Gao F, Winden KD, et al. Functional Genomic Analyses Identify Pathways Dysregulated by Progranulin Deficiency Implicating Wnt Signaling. Neuron [Internet]. 2011 Sep 9;71(6). Available from: http://www.ncbi.nlm.nih.gov/pmc/articles/PMC3633414/

173. Reinecke F, Smeitink JAM, van der Westhuizen FH. OXPHOS gene expression and control in mitochondrial disorders. Biochimica et Biophysica Acta (BBA) - Molecular Basis of Disease [Internet]. 2009 Dec 1;1792(12):1113–21. Available from: http://dx.doi.org/10.1016/J.BBADIS.2009.04.003

174. Barnham KJ, Masters CL, Bush AI. Neurodegenerative diseases and oxidative stress. Nature Reviews Drug Discovery 2004 3:3 [Internet]. 2004;3(3):205–14. Available from: https://www.nature.com/articles/nrd1330

175. Mukherjee AB, Appu AP, Sadhukhan T, Casey S, Mondal A, Zhang Z, et al. Emerging new roles of the lysosome and neuronal ceroid lipofuscinoses. Mol Neurodegener [Internet]. 2019 Jan 16;14(1). Available from: https://www.ncbi.nlm.nih.gov/pmc/articles/PMC6335712/

176. Guo CY, Sun L, Chen XP, Zhang DS. Oxidative stress, mitochondrial damage and neurodegenerative diseases. Neural Regeneration Res [Internet]. 2013 Jul 7;8(21):2003. Available from: https://www.ncbi.nlm.nih.gov/pmc/articles/PMC4145906/

177. Ashraf A, Jeandriens J, Parkes HG, So PW. Iron dyshomeostasis, lipid peroxidation and perturbed expression of cystine/glutamate antiporter in Alzheimer's disease: Evidence of ferroptosis. Redox Biology [Internet]. 2020 May 1;32:101494. Available from: http://dx.doi.org/10.1016/J.REDOX.2020.101494

178. Mahoney-Sánchez L, Bouchaoui H, Ayton S, Devos D, Duce JA, Devedjian JC. Ferroptosis and its potential role in the physiopathology of Parkinson's Disease. Prog Neurobiol [Internet]. 2021 Jan 1;196:101890. Available from: http://dx.doi.org/10.1016/J.PNEUROBIO.2020.101890

179. Wang T, Tomas D, Perera ND, Cuic B, Luikinga S, Viden A, et al. Ferroptosis mediates selective motor neuron death in amyotrophic lateral sclerosis. Cell Death Differ [Internet]. 2022 Jun 1;29(6):1187–98. Available from: https://pubmed.ncbi.nlm.nih.gov/34857917/

180. Li X, Cheng S, Hu H, Zhang X, Xu J, Wang R, et al. Progranulin protects against cerebral ischemia-reperfusion (I/R) injury by inhibiting necroptosis and oxidative stress. Biochem Biophys Res Commun [Internet]. 2020 Jan 15;521(3):569–76. Available from: http://dx.doi.org/10.1016/J.BBRC.2019.09.111

181. Chen T, Shi R, Suo Q, Wu S, Liu C, Huang S, et al. Progranulin released from microglial lysosomes reduces neuronal ferroptosis after cerebral ischemia in mice. J Cereb Blood Flow Metab [Internet]. 2023 Apr 1;43(4):505–17. Available from: https://journals.sagepub.com/doi/full/10.1177/0271678X221145090

182. Tian R, Abarientos A, Hong J, Hashemi SH, Yan R, Dräger N, et al. Genome-wide CRISPRi/a screens in human neurons link lysosomal failure to ferroptosis. Nat Neurosci [Internet]. 2021 Jul 1;24(7):1020. Available from: https://www.ncbi.nlm.nih.gov/pmc/articles/PMC8254803/

183. Ward DM, Cloonan SM. Mitochondrial Iron in Human Health and Disease. Annu Rev

Physiol [Internet]. 2019 Feb 2;81:453. Available from: https://www.ncbi.nlm.nih.gov/pmc/articles/PMC6641538/

184. Zhang Y, Swanda RV, Nie L, Liu X, Wang C, Lee H, et al. mTORC1 couples cyst(e)ine availability with GPX4 protein synthesis and ferroptosis regulation. 2021;12(1):1–14. Available from: https://www.nature.com/articles/s41467-021-21841-w

185. Swanda RV, Ji Q, Wu X, Yan J, Dong L, Mao Y, et al. Lysosomal cystine governs ferroptosis sensitivity in cancer via cysteine stress response. Mol Cell [Internet]. 2023 Sep 21;83(18):3347-3359.e9. Available from: http://dx.doi.org/10.1016/J.MOLCEL.2023.08.004

186. Ren JX, Sun X, Yan XL, Guo ZN, Yang Y. Ferroptosis in Neurological Diseases. Front Cell Neurosci [Internet]. 2020 Jul 13;14:554464. Available from: http://dx.doi.org/10.3389/FNCEL.2020.00218/BIBTEX

187. Jin X, Yamashita T. Microglia in central nervous system repair after injury. J Biochem [Internet]. 2016 May 1;159(5):491–6. Available from: https://dx.doi.org/10.1093/jb/mvw009

188. Leng F, Edison P. Neuroinflammation and microglial activation in Alzheimer disease: where do we go from here? Nature Reviews Neurology 2020 17:3 [Internet]. 2020 Dec 14;17(3):157–72. Available from: https://www.nature.com/articles/s41582-020-00435-y

189. Wu Y, Shao W, Todd TW, Tong J, Yue M, Koga S, et al. Microglial lysosome dysfunction contributes to white matter pathology and TDP-43 proteinopathy in GRN-associated FTD. Cell Rep [Internet]. 2021;36(8):109581. Available from: https://doi.org/10.1016/j.celrep.2021.109581

190. Chausse B, Kakimoto PA, Kann O. Microglia and lipids: how metabolism controls brain innate immunity. Semin Cell Dev Biol [Internet]. 2021 Apr 1;112:137–44. Available from: http://dx.doi.org/10.1016/J.SEMCDB.2020.08.001

191. Boland S, Swarup S, Ambaw YA, Malia PC, Richards RC, Fischer AW, et al. Deficiency of the frontotemporal dementia gene GRN results in gangliosidosis. Nature Communications 2022 13:1 [Internet]. 2022 Oct 7;13(1):1–13. Available from: https://www.nature.com/articles/s41467-022-33500-9

192. Reifschneider A, Robinson S, van Lengerich B, Gnörich J, Logan T, Heindl S, et al. Loss of TREM2 rescues hyperactivation of microglia, but not lysosomal deficits and neurotoxicity in models of progranulin deficiency. EMBO J [Internet]. 2022 Feb 15;41(4):e109108. Available from: https://onlinelibrary.wiley.com/doi/full/10.15252/embj.2021109108

193. Zhang T, Feng T, Wu K, Guo J, Nana AL, Yang G, et al. Progranulin deficiency results in

sex-dependent alterations in microglia in response to demyelination. Acta Neuropathol [Internet]. 2023 Apr 30;146(1):97–119. Available from: https://link.springer.com/article/10.1007/s00401-023-02578-w

194. Dräger NM, Sattler SM, Huang CT-L, Teter OM, Leng K, Hashemi SH, et al. A CRISPRi/a platform in human iPSC-derived microglia uncovers regulators of disease states. Nat Neurosci [Internet]. 2022 Sep;25(9):1149–62. Available from: http://dx.doi.org/10.1038/s41593-022-01131-4

195. Douvaras P, Sun B, Wang M, Kruglikov I, Lallos G, Zimmer M, et al. Directed Differentiation of Human Pluripotent Stem Cells to Microglia. Stem Cell Reports [Internet]. 2017;8(6):1516–24. Available from: http://dx.doi.org/10.1016/j.stemcr.2017.04.023

196. Love MI, Huber W, Anders S. Moderated estimation of fold change and dispersion for RNA-seq data with DESeq2. Genome Biol [Internet]. 2014 Dec 5;15(12):1–21. Available from: https://genomebiology.biomedcentral.com/articles/10.1186/s13059-014-0550-8

197. Subramanian A, Tamayo P, Mootha VK, Mukherjee S, Ebert BL, Gillette MA, et al. Gene set enrichment analysis: a knowledge-based approach for interpreting genome-wide expression profiles. Proc Natl Acad Sci U S A [Internet]. 2005 Oct 25;102(43):15545–50. Available from: http://dx.doi.org/10.1073/pnas.0506580102

198. Pang Z, Chong J, Zhou G, De Lima Morais DA, Chang L, Barrette M, et al. MetaboAnalyst 5.0: narrowing the gap between raw spectra and functional insights. Nucleic Acids Res [Internet]. 2021 Jul 2;49(W1):W388–96. Available from: https://dx.doi.org/10.1093/nar/gkab382

199. Telpoukhovskaia MA, Liu K, Sayed FA, Etchegaray JI, Xie M, Zhan L, et al. Discovery of small molecules that normalize the transcriptome and enhance cysteine cathepsin activity in progranulin-deficient microglia. Sci Rep [Internet]. 2020 Dec 1;10(1):1–12. Available from: https://www.ncbi.nlm.nih.gov/pmc/articles/PMC7426857/

200. Crapser JD, Arreola MA, Tsourmas KI, Green KN. Microglia as hackers of the matrix: sculpting synapses and the extracellular space. Cellular and Molecular Immunology [Internet]. 2021;18(11):2472–88. Available from: http://dx.doi.org/10.1038/s41423-021-00751-3

201. Elia L, Herting B, Alijagic A, Buselli C, Wong L, Morrison G, et al. Frontotemporal Dementia Patient Neurons With Progranulin Deficiency Display Protein Dyshomeostasis. bioRxiv [Internet]. 2023 Jan 20;2023.01.18.524611. Available from: https://www.biorxiv.org/content/10.1101/2023.01.18.524611v1

202. Zhang H, Tian X, Lu X, Xu D, Guo Y, Dong Z, et al. TMEM25 modulates neuronal excitability and NMDA receptor subunit NR2B degradation. J Clin Invest [Internet].

2019 Aug 8;129(9):3864. Available from: https://www.ncbi.nlm.nih.gov/pmc/articles/PMC6715386/

203. Custódio TF, Killer M, Yu D, Puente V, Teufel DP, Pautsch A, et al. Molecular basis of TASL recruitment by the peptide/histidine transporter 1, PHT1. Nature Communications 2023 14:1 [Internet]. 2023 Sep 14;14(1):1–12. Available from: https://www.nature.com/articles/s41467-023-41420-5

204. Lan YJ, Sam NB, Cheng MH, Pan HF, Gao J. Progranulin as a Potential Therapeutic Target in Immune-Mediated Diseases. J Inflamm Res [Internet]. 2021;14:6543. Available from: https://www.ncbi.nlm.nih.gov/pmc/articles/PMC8655512/

205. Jakobsson A, Westerberg R, Jacobsson A. Fatty acid elongases in mammals: their regulation and roles in metabolism. Prog Lipid Res [Internet]. 2006 May;45(3):237–49. Available from: http://dx.doi.org/10.1016/j.plipres.2006.01.004

206. Sassa T, Kihara A. Metabolism of very long-chain Fatty acids: genes and pathophysiology. Biomol Ther [Internet]. 2014 Feb;22(2):83–92. Available from: http://dx.doi.org/10.4062/biomolther.2014.017

207. Bond LM, Miyazaki M, O'Neill LM, Ding F, Ntambi JM. Chapter 6 - Fatty Acid Desaturation and Elongation in Mammals. In: Ridgway ND, McLeod RS, editors. Biochemistry of Lipids, Lipoproteins and Membranes (Sixth Edition) [Internet]. Boston: Elsevier; 2016. p. 185–208. Available from: https://www.sciencedirect.com/science/article/pii/B9780444634382000067

208. Franklin MP, Sathyanarayan A, Mashek DG. Acyl-CoA Thioesterase 1 (ACOT1) Regulates PPARα to Couple Fatty Acid Flux With Oxidative Capacity During Fasting. Diabetes [Internet]. 2017 Aug;66(8):2112–23. Available from: http://dx.doi.org/10.2337/db16-1519

209. Wang Y, Yu W, Li S, Guo D, He J, Wang Y. Acetyl-CoA Carboxylases and Diseases. Front Oncol [Internet]. 2022 Mar 11;12:836058. Available from: http://dx.doi.org/10.3389/fonc.2022.836058

210. McFadden JW, Corl BA. Activation of liver X receptor (LXR) enhances de novo fatty acid synthesis in bovine mammary epithelial cells. J Dairy Sci [Internet]. 2010 Oct;93(10):4651–8. Available from: http://dx.doi.org/10.3168/jds.2010-3202

211. Jalil A, Bourgeois T, Ménégaut L, Lagrost L, Thomas C, Masson D. Revisiting the Role of LXRs in PUFA Metabolism and Phospholipid Homeostasis. Int J Mol Sci [Internet]. 2019 Aug 2;20(15). Available from: http://dx.doi.org/10.3390/ijms20153787

212. Varga T, Czimmerer Z, Nagy L. PPARs are a unique set of fatty acid regulated transcription factors controlling both lipid metabolism and inflammation. Biochim Biophys Acta [Internet]. 2011 Aug;1812(8):1007–22. Available from:

http://dx.doi.org/10.1016/j.bbadis.2011.02.014

213. Chen T, Tong F, Wu X-Y, Zhu L, Yi Q-Z, Zheng J, et al. Novel ACADVL variants resulting in mitochondrial defects in long-chain acyl-CoA dehydrogenase deficiency. J Zhejiang Univ Sci B [Internet]. 2020 Nov;21(11):885–96. Available from: http://dx.doi.org/10.1631/jzus.B2000339

214. Chen-Plotkin AS, Geser F, Plotkin JB, Clark CM, Kwong LK, Yuan W, et al. Variations in the progranulin gene affect global gene expression in frontotemporal lobar degeneration. Hum Mol Genet [Internet]. 2008 May 15;17(10):1349–62. Available from: http://dx.doi.org/10.1093/hmg/ddn023

215. Vandevrede L, Rojas JC, Wang P, Heuer HW, Karydas AM, Ljubenkov PA, et al. Lipid metabolism dysfunction in progranulin mutation carriers: Unbiased metabolomics reveals strong relationship to clinical status in FTLD. Alzheimers Dement [Internet]. 2020 Dec;16(S5). Available from: https://alz-journals.onlinelibrary.wiley.com/doi/10.1002/alz.046594

216. Krasemann S, Madore C, Cialic R, Baufeld C, Calcagno N, El Fatimy R, et al. The TREM2-APOE Pathway Drives the Transcriptional Phenotype of Dysfunctional Microglia in Neurodegenerative Diseases. Immunity [Internet]. 2017 Sep 19;47(3):566-581.e9. Available from: http://dx.doi.org/10.1016/J.IMMUNI.2017.08.008

217. Holtman IR, Raj DD, Miller JA, Schaafsma W, Yin Z, Brouwer N, et al. Induction of a common microglia gene expression signature by aging and neurodegenerative conditions: a co-expression meta-analysis. Acta neuropathologica communications [Internet]. 2015 May 23;3:31. Available from: https://pubmed.ncbi.nlm.nih.gov/26001565/

218. Chiu IM, Morimoto ETA, Goodarzi H, Liao JT, O'Keeffe S, Phatnani HP, et al. A neurodegeneration-specific gene-expression signature of acutely isolated microglia from an amyotrophic lateral sclerosis mouse model. Cell Rep [Internet]. 2013 Jul 25;4(2):385–401. Available from: https://pubmed.ncbi.nlm.nih.gov/23850290/

219. Wang Y, Cella M, Mallinson K, Ulrich JD, Young KL, Robinette ML, et al. TREM2 lipid sensing sustains the microglial response in an Alzheimer's disease model. Cell [Internet]. 2015 Mar 15;160(6):1061–71. Available from: https://pubmed.ncbi.nlm.nih.gov/25728668/

220. Keren-Shaul H, Spinrad A, Weiner A, Matcovitch-Natan O, Dvir-Szternfeld R, Ulland TK, et al. A Unique Microglia Type Associated with Restricting Development of Alzheimer's Disease. Cell [Internet]. 2017 Jun 15;169(7):1276-1290.e17. Available from: https://pubmed.ncbi.nlm.nih.gov/28602351/

221. Srinivasan K, Friedman BA, Etxeberria A, Huntley MA, van der Brug MP, Foreman O, et

al. Alzheimer's Patient Microglia Exhibit Enhanced Aging and Unique Transcriptional Activation. Cell Rep [Internet]. 2020 Jun 6;31(13):107843. Available from: https://www.ncbi.nlm.nih.gov/pmc/articles/PMC7422733/

222. Victor MB, Leary N, Luna X, Meharena HS, Scannail AN, Bozzelli PL, et al. Lipid accumulation induced by APOE4 impairs microglial surveillance of neuronal-network activity. Cell Stem Cell [Internet]. 2022 Aug 4;29(8):1197-1212.e8. Available from: http://dx.doi.org/10.1016/J.STEM.2022.07.005

223. Gao C, Jiang J, Tan Y, Chen S. Microglia in neurodegenerative diseases: mechanism and potential therapeutic targets. Signal Transduction and Targeted Therapy 2023 8:1 [Internet]. 2023 Sep 22;8(1):1–37. Available from: https://www.nature.com/articles/s41392-023-01588-0

224. Blank M, Enzlein T, Hopf C. LPS-induced lipid alterations in microglia revealed by MALDI mass spectrometry-based cell fingerprinting in neuroinflammation studies. Scientific Reports 2022 12:1 [Internet]. 2022 Feb 21;12(1):1–13. Available from: https://www.nature.com/articles/s41598-022-06894-1

225. Chen Z, Jalabi W, Shpargel KB, Farabaugh KT, Dutta R, Yin X, et al. Lipopolysaccharide-induced microglial activation and neuroprotection against experimental brain injury is independent of hematogenous TLR4. J Neurosci [Internet]. 2012 Aug 22;32(34):11706–15. Available from: http://dx.doi.org/10.1523/JNEUROSCI.0730-12.2012

226. Lively S, Schlichter LC. Microglia Responses to Pro-inflammatory Stimuli (LPS, IFNγ+TNFα) and Reprogramming by Resolving Cytokines (IL-4, IL-10). Front Cell Neurosci [Internet]. 2018 Jul 24;12:215. Available from: http://dx.doi.org/10.3389/fncel.2018.00215

227. La Torre ME, Panaro MA, Ruggiero M, Polito R, Cianciulli A, Filannino FM, et al. Extracellular Vesicles Cargo in Modulating Microglia Functional Responses. Biology [Internet]. 2022 Sep 29;11(10). Available from: http://dx.doi.org/10.3390/biology11101426

228. Lively S, Schlichter LC. The microglial activation state regulates migration and roles of matrix-dissolving enzymes for invasion. J Neuroinflammation [Internet]. 2013 Jun 21;10:75. Available from: https://www.ncbi.nlm.nih.gov/pmc/articles/PMC3693964/

229. Nair S, Sobotka KS, Joshi P, Gressens P, Fleiss B, Thornton C, et al. Lipopolysaccharide-induced alteration of mitochondrial morphology induces a metabolic shift in microglia modulating the inflammatory response in vitro and in vivo. Glia [Internet]. 2019 Jun;67(6):1047–61. Available from: http://dx.doi.org/10.1002/glia.23587

230. Liu X, Jiang N, Zhou W. Various Energetic Metabolism of Microglia in Response to Different Stimulations. Molecules [Internet]. 2023 Jun 1;28(11). Available from:

http://dx.doi.org/10.3390/molecules28114501

231. Li LO, Klett EL, Coleman RA. Acyl-CoA synthesis, lipid metabolism and lipotoxicity. Biochim Biophys Acta [Internet]. 2010 Mar;1801(3):246–51. Available from: http://dx.doi.org/10.1016/j.bbalip.2009.09.024

232. Khatchadourian A, Bourque SD, Richard VR, Titorenko VI, Maysinger D. Dynamics and regulation of lipid droplet formation in lipopolysaccharide (LPS)-stimulated microglia. Biochim Biophys Acta [Internet]. 2012 Apr;1821(4):607–17. Available from: http://dx.doi.org/10.1016/j.bbalip.2012.01.007

233. Raulien N, Friedrich K, Strobel S, Rubner S, Baumann S, von Bergen M, et al. Fatty Acid Oxidation Compensates for Lipopolysaccharide-Induced Warburg Effect in Glucose-Deprived Monocytes. Front Immunol [Internet]. 2017 May 29;8:609. Available from: http://dx.doi.org/10.3389/fimmu.2017.00609

234. He Y, Taylor N, Yao X, Bhattacharya A. Mouse primary microglia respond differently to LPS and poly(I:C) in vitro. Sci Rep [Internet]. 2021 May 17;11(1):10447. Available from: http://dx.doi.org/10.1038/s41598-021-89777-1

235. Liu H, Hu X, Jiang R, Cai J, Lin Q, Fan Z, et al. CQMUH-011 Inhibits LPS-Induced Microglia Activation and Ameliorates Brain Ischemic Injury in Mice. Inflammation [Internet]. 2021 Aug;44(4):1345–58. Available from: http://dx.doi.org/10.1007/s10753-021-01420-3

236. Ahn SK, Hong S, Park YM, Choi JY, Lee WT, Park KA, et al. Protective effects of agmatine on lipopolysaccharide-injured microglia and inducible nitric oxide synthase activity. Life Sci [Internet]. 2012 Dec 17;91(25–26):1345–50. Available from: http://dx.doi.org/10.1016/j.lfs.2012.10.010

237. Ponomarev ED, Shriver LP, Dittel BN. CD40 expression by microglial cells is required for their completion of a two-step activation process during central nervous system autoimmune inflammation. J Immunol [Internet]. 2006 Feb 1;176(3):1402–10. Available from: http://dx.doi.org/10.4049/jimmunol.176.3.1402

238. Wang T, Qin L, Liu B, Liu Y, Wilson B, Eling TE, et al. Role of reactive oxygen species in LPS-induced production of prostaglandin E2 in microglia. J Neurochem [Internet]. 2004 Feb;88(4):939–47. Available from: http://dx.doi.org/10.1046/j.1471-4159.2003.02242.x

239. Adachi S, Obaya AJ, Han Z, Ramos-Desimone N, Wyche JH, Sedivy JM. c-Myc is necessary for DNA damage-induced apoptosis in the G(2) phase of the cell cycle. Mol Cell Biol [Internet]. 2001 Aug;21(15):4929–37. Available from: http://dx.doi.org/10.1128/MCB.21.15.4929-4937.2001

240. Cheng Z, Mugler CF, Keskin A, Hodapp S, Chan LY-L, Weis K, et al. Small and Large

Ribosomal Subunit Deficiencies Lead to Distinct Gene Expression Signatures that Reflect Cellular Growth Rate. Mol Cell [Internet]. 2019 Jan 3;73(1):36-47.e10. Available from: http://dx.doi.org/10.1016/j.molcel.2018.10.032

241. Chua BA, Van Der Werf I, Jamieson C, Signer RAJ. Post-Transcriptional Regulation of Homeostatic, Stressed, and Malignant Stem Cells. Cell Stem Cell [Internet]. 2020 Feb 6;26(2):138–59. Available from: http://dx.doi.org/10.1016/j.stem.2020.01.005

242. Lauro C, Limatola C. Metabolic Reprograming of Microglia in the Regulation of the Innate Inflammatory Response. Front Immunol [Internet]. 2020 Mar 20;11:493. Available from: http://dx.doi.org/10.3389/fimmu.2020.00493

243. Zubova SG, Suvorova II, Karpenko MN. Macrophage and microglia polarization: focus on autophagy-dependent reprogramming. Front Biosci [Internet]. 2022 Jan 20;14(1):3. Available from: http://dx.doi.org/10.31083/j.fbs1401003

244. Lattka E, Illig T, Koletzko B, Heinrich J. Genetic variants of the FADS1 FADS2 gene cluster as related to essential fatty acid metabolism. Curr Opin Lipidol [Internet]. 2010 Feb;21(1):64–9. Available from: http://dx.doi.org/10.1097/MOL.0b013e3283327ca8

245. Cadenas C, Vosbeck S, Edlund K, Grgas K, Madjar K, Hellwig B, et al. LIPG-promoted lipid storage mediates adaptation to oxidative stress in breast cancer. Int J Cancer [Internet]. 2019 Aug 15;145(4):901–15. Available from: http://dx.doi.org/10.1002/ijc.32138

246. Mai M, Guo X, Huang Y, Zhang W, Xu Y, Zhang Y, et al. DHCR24 Knockdown Induces Tau Hyperphosphorylation at Thr181, Ser199, Ser262, and Ser396 Sites via Activation of the Lipid Raft-Dependent Ras/MEK/ERK Signaling Pathway in C8D1A Astrocytes. Mol Neurobiol [Internet]. 2022 Sep;59(9):5856–73. Available from: http://dx.doi.org/10.1007/s12035-022-02945-w

247. Wu S-C, Lo Y-M, Lee J-H, Chen C-Y, Chen T-W, Liu H-W, et al. Stomatin modulates adipogenesis through the ERK pathway and regulates fatty acid uptake and lipid droplet growth. Nat Commun [Internet]. 2022 Jul 19;13(1):4174. Available from: http://dx.doi.org/10.1038/s41467-022-31825-z

248. Hussain SS, Tran T-M, Ware TB, Luse MA, Prevost CT, Ferguson AN, et al. RalA and PLD1 promote lipid droplet growth in response to nutrient withdrawal. Cell Rep [Internet]. 2021 Jul 27;36(4):109451. Available from: http://dx.doi.org/10.1016/j.celrep.2021.109451

249. Wang T, Yan R, Xu X, Yu H, Wu J, Yang Y, et al. Effects of leukemia inhibitory factor receptor on the adipogenic differentiation of human bone marrow mesenchymal stem cells. Mol Med Rep [Internet]. 2019 Jun;19(6):4719–26. Available from: http://dx.doi.org/10.3892/mmr.2019.10140

250. Wang X, Ma J, Fu Q, Zhu L, Zhang Z, Zhang F, et al. Role of hypoxia-inducible factor-1α in autophagic cell death in microglial cells induced by hypoxia. Mol Med Rep [Internet]. 2017 Apr;15(4):2097–105. Available from: http://dx.doi.org/10.3892/mmr.2017.6277

251. Bok S, Kim Y-E, Woo Y, Kim S, Kang S-J, Lee Y, et al. Hypoxia-inducible factor-1α regulates microglial functions affecting neuronal survival in the acute phase of ischemic stroke in mice. Oncotarget [Internet]. 2017 Dec 19;8(67):111508–21. Available from: http://dx.doi.org/10.18632/oncotarget.22851

252. Viola A, Munari F, Sánchez-Rodríguez R, Scolaro T, Castegna A. The Metabolic Signature of Macrophage Responses. Front Immunol [Internet]. 2019 Jul 3;10:1462. Available from: http://dx.doi.org/10.3389/fimmu.2019.01462

253. Frede S, Stockmann C, Freitag P, Fandrey J. Bacterial lipopolysaccharide induces HIF-1 activation in human monocytes via p44/42 MAPK and NF-kappaB. Biochem J [Internet]. 2006 Jun 15;396(3):517–27. Available from: http://dx.doi.org/10.1042/BJ20051839

254. Bensaad K, Favaro E, Lewis CA, Peck B, Lord S, Collins JM, et al. Fatty acid uptake and lipid storage induced by HIF-1α contribute to cell growth and survival after hypoxia-reoxygenation. Cell Rep [Internet]. 2014 Oct 9;9(1):349–65. Available from: http://dx.doi.org/10.1016/j.celrep.2014.08.056

255. Jump DB. Mammalian fatty acid elongases. Methods Mol Biol [Internet]. 2009;579:375–89. Available from: http://dx.doi.org/10.1007/978-1-60761-322-0_19

256. Broadfield LA, Pane AA, Talebi A, Swinnen JV, Fendt S-M. Lipid metabolism in cancer: New perspectives and emerging mechanisms. Dev Cell [Internet]. 2021 May 17;56(10):1363–93. Available from: http://dx.doi.org/10.1016/j.devcel.2021.04.013

257. Bhat N, Mani A. Dysregulation of Lipid and Glucose Metabolism in Nonalcoholic Fatty Liver Disease. Nutrients [Internet]. 2023 May 16;15(10). Available from: http://dx.doi.org/10.3390/nu15102323

258. Remec ZI, Groselj U, Drole Torkar A, Zerjav Tansek M, Cuk V, Perko D, et al. Very Long-Chain Acyl-CoA Dehydrogenase Deficiency: High Incidence of Detected Patients With Expanded Newborn Screening Program. Front Genet [Internet]. 2021 Apr 27;12:648493. Available from: http://dx.doi.org/10.3389/fgene.2021.648493

259. Murakami M, Sato H, Taketomi Y. Updating Phospholipase A2 Biology. Biomolecules [Internet]. 2020 Oct 19;10(10). Available from: http://dx.doi.org/10.3390/biom10101457

260. Murakami M, Miki Y, Sato H, Murase R, Taketomi Y, Yamamoto K. Group IID, IIE, IIF and III secreted phospholipase A2s. Biochim Biophys Acta Mol Cell Biol Lipids [Internet]. 2019 Jun;1864(6):803–18. Available from: http://dx.doi.org/10.1016/j.bbalip.2018.08.014

261. Ferchaud-Roucher V, Rudolph MC, Jansson T, Powell TL. Fatty acid and lipid profiles in primary human trophoblast over 90h in culture. Prostaglandins Leukot Essent Fatty Acids [Internet]. 2017 Jun;121:14–20. Available from: http://dx.doi.org/10.1016/j.plefa.2017.06.001

262. Loving BA, Bruce KD. Lipid and Lipoprotein Metabolism in Microglia. Front Physiol [Internet]. 2020 Apr 28;11:393. Available from: http://dx.doi.org/10.3389/fphys.2020.00393

263. Elia LP, Mason AR, Alijagic A, Finkbeiner S. Genetic Regulation of Neuronal Progranulin Reveals a Critical Role for the Autophagy-Lysosome Pathway. J Neurosci [Internet]. 2019 Apr 24;39(17):3332–44. Available from: http://dx.doi.org/10.1523/JNEUROSCI.3498-17.2019

264. Götzl JK, Colombo AV, Fellerer K, Reifschneider A, Werner G, Tahirovic S, et al. Early lysosomal maturation deficits in microglia triggers enhanced lysosomal activity in other brain cells of progranulin knockout mice. Mol Neurodegener [Internet]. 2018 Sep 4;13(1). Available from: https://www.ncbi.nlm.nih.gov/pmc/articles/PMC6123925/

265. van Dierendonck XAMH, Vrieling F, Smeehuijzen L, Deng L, Boogaard JP, Croes C-A, et al. Triglyceride breakdown from lipid droplets regulates the inflammatory response in macrophages. Proc Natl Acad Sci U S A [Internet]. 2022 Mar 22;119(12):e2114739119. Available from: http://dx.doi.org/10.1073/pnas.2114739119

266. den Brok MH, Raaijmakers TK, Collado-Camps E, Adema GJ. Lipid Droplets as Immune Modulators in Myeloid Cells. Trends Immunol [Internet]. 2018 May;39(5):380–92. Available from: http://dx.doi.org/10.1016/j.it.2018.01.012

267. Jarc E, Petan T. A twist of FATe: Lipid droplets and inflammatory lipid mediators. Biochimie [Internet]. 2020 Feb;169:69–87. Available from: http://dx.doi.org/10.1016/j.biochi.2019.11.016

268. Raas Q, Tawbeh A, Tahri-Joutey M, Gondcaille C, Keime C, Kaiser R, et al. Peroxisomal defects in microglial cells induce a disease-associated microglial signature. Front Mol Neurosci [Internet]. 2023 Apr 17;16:1170313. Available from: http://dx.doi.org/10.3389/fnmol.2023.1170313

269. Poulos A, Beckman K, Johnson DW, Paton BC, Robinson BS, Sharp P, et al. Very Long-Chain Fatty Acids in Peroxisomal Disease. In: Bazan NG, Murphy MG, Toffano G, editors. Neurobiology of Essential Fatty Acids [Internet]. Boston, MA: Springer US; 1992. p. 331–40. Available from: https://doi.org/10.1007/978-1-4615-3426-6_30

270. Ruiz-Sala P, Peña-Quintana L. Biochemical Markers for the Diagnosis of Mitochondrial Fatty Acid Oxidation Diseases. J Clin Med Res [Internet]. 2021 Oct 22;10(21). Available from: http://dx.doi.org/10.3390/jcm10214855

271. Uzor N-E, McCullough LD, Tsvetkov AS. Peroxisomal Dysfunction in Neurological Diseases and Brain Aging. Front Cell Neurosci [Internet]. 2020 Mar 10;14:44. Available from: http://dx.doi.org/10.3389/fncel.2020.00044

272. Ertunc ME, Hotamisligil GS. Lipid signaling and lipotoxicity in metaflammation: indications for metabolic disease pathogenesis and treatment. J Lipid Res [Internet]. 2016 Dec;57(12):2099–114. Available from: http://dx.doi.org/10.1194/jlr.R066514

273. Martínez-Reyes I, Chandel NS. Mitochondrial TCA cycle metabolites control physiology and disease. Nat Commun [Internet]. 2020 Jan 3;11(1):102. Available from: http://dx.doi.org/10.1038/s41467-019-13668-3